

TRITIUM SUPPRESSION FACTOR OF THE KATRIN TRANSPORT SECTION

Zur Erlangung des akademischen Grades eines

DOKTORS DER NATURWISSENSCHAFTEN

von der KIT-Fakultät für Physik des
Karlsruher Instituts für Technologie
genehmigte

DISSERTATION

von

M. Sc. Carsten Röttele

aus Ehrenkirchen

Referent: Prof. Dr. Guido Drexlin
Institut für Experimentelle Teilchenphysik (ETP)
Korreferent: Prof. Dr. Ulrich Husemann
Institut für Experimentelle Teilchenphysik (ETP)

Tag der mündlichen Prüfung: 07. Juni 2019

Declaration of authorship Herewith I affirm that I wrote the current thesis on my own and without the usage of any other sources or tools than the cited ones and that this thesis has not been handed neither in this nor in equal form at any other official commission.

Erklärung der Selbstständigkeit Hiermit versichere ich, die vorliegende Arbeit selbstständig angefertigt zu haben und keine Hilfsmittel jenseits der kenntlich gemachten verwendet zu haben. Weiterhin habe ich weder diese noch eine äquivalente Version dieser Arbeit bei einer anderen Prüfungskommission vorgelegt.

Karlsruhe, 21.05.2019

.....
(Carsten Röttele)

Introduction

With the postulation of a neutral particle [PKW64], which is produced in addition to the electron during a β -decay, the neutrino was "born" in 1930. Despite that neutrinos are the most abundant particle in the Universe, it took more than 20 years to detect this particle directly in an experiment [RC53]. As neutrinos only interact weakly and because of this, their cross section is small, the detection of them is very challenging. With the detection of the muon neutrino in 1962 [DGG⁺62] and the tau neutrino in 2000 [KUA⁺01], there are nowadays three known neutrino flavors in the standard model of elementary particles.

As of today, neutrino physics is one of the most exciting and challenging fields of physics with many things left to explain. One important parameter is the neutrino mass, which has not yet been measured. In the standard model, neutrinos are massless. However, the detection of neutrino oscillations can only be explained when neutrinos have a non-vanishing mass. Since the 1940s, there were many experiments that have tried to determine their mass. However, only upper limits have been found so far. With a model independent measurement, the limit for an effective electron antineutrino mass is given by $m_{\nu_e} < 2.0 \text{ eV}$ (95% C.L.) [KBB⁺05, ABB⁺11]. With the knowledge of the previous experiments, the KATRIN experiment has been set up in Karlsruhe to follow further this way.

The Karlsruhe tritium neutrino experiment (KATRIN) aims to measure the effective electron anti-neutrino mass with an unprecedented sensitivity of 0.2 eV (90% C.L.) [KAT05]. In KATRIN, the kinematics of electrons from the tritium β -decay are used to analyze the neutrino mass squared model-independently as a parameter in fit to β -electron spectrum. The β -electrons are produced in the windowless gaseous tritium source (WGTS), and afterwards adiabatically guided through the transport and pumping section into the spectrometer section. In the spectrometer section, the magnetic adiabatic collimation combined with an electrostatic filter (MAC-E filter) method is applied to measure the β -electrons' energy with a high energy resolution. Finally, the β -electron rate is counted on a detector.

In order to keep the background level of tritium decaying in the spectrometers in the mHz level, the tritium flow from the source to the spectrometer has to be reduced by at least 14 orders of magnitude. Therefore, the pumping section combines

a differential pumping section (DPS) and a cryogenic pumping section (CPS) as a cold trap with a tritium reduction of 10^7 each. In the DPS, turbomolecular pumps (TMPs) are installed to fulfill this task, while in the CPS a frozen argon layer kept at 3 K is prepared. As an essential part to demonstrate the integrity of the experiment, the pumping system has to prove its functionality before tritium is injected for the first time. Otherwise, tritium could get implanted into the spectrometers, which would lead to a non reversible contamination. In this case, the background rate would be too high so that no competitive neutrino mass analysis is possible. Therefore, commissioning measurements have to be performed with non radioactive gases in order to prove the required retention. These measurement results have to be confirmed with simulation results so that the first tritium can be entered into the KATRIN source.

In this thesis, the focus is set on the KATRIN pumping sections dedicated to the tritium reduction. The commissioning of those systems builds an important milestone for the KATRIN experiment. The successful execution of several reduction measurements as presented in this work allowed the begin of first KATRIN tritium operation. The thesis is structured as it follows:

In the first chapter 1, an introduction of the neutrino physic is given. Therefore, the discovery of the different neutrino flavors are placed in historic context before their role in the standard model is discussed. The principle of neutrino oscillation, which proved that neutrinos have to be massive, are explained as well as a possible neutrino mass mechanism. Additionally, several neutrino mass experiments are presented.

In the next chapter 2, the setup of the KATRIN experiment is introduced. The (several) specific components are described together with the processes which induce background events in the spectrometers.

Chapter 3 discusses the pumping principles of the DPS and CPS. An introduction for argon frost pumps is given, with a focus set on hydrogen as an adsorbent. Furthermore, the technical process for argon frost preparation and regeneration are explained.

In chapter 4, simulations are performed for the investigation of the DPS and CPS reduction factors. These simulations have to meet several challenges.

Chapter 5 presents the commissioning measurements with the DPS and CPS. For both components, measurements with deuterium are outlined as well as the analysis of the reduction factor. Additionally, investigations on the background rate are made for the first KATRIN tritium campaign. With a complementary approach, the combined reduction factor of the WGTS and DPS is analyzed.

Finally, a conclusion and an outlook are given in chapter 6.

Contents

Introduction	v
1. Neutrino physics	1
1.1. First discovery	1
1.2. Neutrinos in the standard model	3
1.3. Neutrino oscillation	4
1.3.1. Theory	4
1.3.2. Experiments	7
1.4. Neutrino mass	9
1.4.1. Neutrino mass generation	9
1.4.2. Neutrino mass experiments	11
1.4.2.1. Model dependent measurement	11
1.4.2.1.1. Cosmology	11
1.4.2.1.2. Supernova neutrinos	12
1.4.2.1.3. Neutrinoless double beta decay	13
1.4.3. Model independent measurements	14
1.4.3.1. Rhenium and holmium as β -emitters	16
1.4.3.2. Tritium as a β -emitter	16
2. The Karlsruhe Tritium Neutrino Experiment	19
2.1. KATRIN measurement principle	19
2.2. Major components of the KATRIN experiment	20
2.2.1. Windowless gaseous tritium source	21
2.2.2. Monitoring devices	23
2.2.2.1. Rear section	23
2.2.2.2. Laser Raman system	24
2.2.2.3. Forward beam monitor	24
2.2.3. Differential pumping section	24
2.2.4. Cryogenic pumping section	26
2.2.5. Spectrometer section	27
2.2.5.1. Pre-spectrometer	30
2.2.5.2. Main spectrometer	30
2.2.6. Detector	31
2.2.7. Monitor spectrometer	32
2.3. Background processes	32
2.3.1. Magnetically stored particles in the spectrometer	33
2.3.2. Penning traps	34
2.3.3. Muon-induced background	34
2.3.4. Natural radioactivity	35

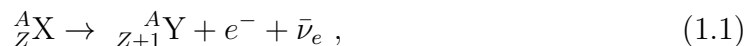
2.3.5.	Radon induced background	36
2.3.6.	Rydberg hypothesis	37
2.3.7.	Tritium induced background	38
3.	Pumping Sections	39
3.1.	Differential Pumping Section	39
3.2.	Cryogenic Pumping Section	39
3.2.1.	Adsorption on cold surfaces	40
3.2.1.1.	Argon properties as a cryo-stat	41
3.2.2.	Hydrogen on frozen argon layer	42
3.2.3.	Kinematics for adsorption and desorption processes	42
3.2.4.	Setup of the cryogenic pumping section	43
3.2.5.	Argon frost preparation	45
3.2.5.1.	Argon inlet system	45
3.2.5.2.	Buffer vessel volume	46
3.2.5.3.	Conductances of argon capillaries	47
3.2.5.4.	Amount of argon needed for argon frost preparation	48
3.2.5.5.	Preparation procedure	48
3.2.5.6.	Helium purging	50
4.	Simulations of reduction factors	51
4.1.	Simulation programs	51
4.1.1.	MolFlow+	51
4.1.2.	COMSOL Multiphysics	52
4.2.	DPS reduction factor simulation	52
4.3.	CPS reduction factor simulations	55
4.3.1.	Cold trap temperature simulation	55
4.3.2.	MolFlow+ simulation	59
4.3.3.	Semi-analytical tracking model	66
4.4.	Summary	70
5.	Measurements of the gas flow reduction factor	73
5.1.	Measurements with deuterium	73
5.1.1.	Reduction factor of the differential pumping section	74
5.1.2.	Reduction factor of the cryogenic pumping section	77
5.1.2.1.	Deuterium inlet system	78
5.1.2.1.1.	Determination of buffer vessel volume	78
5.1.2.2.	Test measurement with helium	78
5.1.2.3.	Calibration of the residual gas analyzer	81
5.1.2.4.	Reduction measurements without argon frost layer	83
5.1.2.4.1.	First deuterium reduction factor measurement	84
5.1.2.4.2.	Reduction factor measurement with a residual gas analyzer	85
5.1.2.5.	Reduction factor measurements with an argon frost layer	86
5.1.2.5.1.	First reduction factor measurement with argon frost layer	86

5.1.2.5.2.	Second reduction factor measurement with an argon frost layer	88
5.1.2.5.3.	Temperature dependence measurement of the CPS reduction factor	89
5.2.	Measurements with tritium	94
5.2.1.	Goals of the First Tritium campaign	94
5.2.2.	Accumulated activity in the cryogenic pumping section	95
5.2.3.	Stability of the background rate	96
5.3.	Summary	102
6.	Summary and outlook	105
Appendix		109
A.	Measurement buffer vessel volume of argon inlet system	110
B.	Measurement buffer vessel volume of deuterium inlet system	110
C.	CPS loops piping and instrumentation diagram	111
D.	MAG W 2800 pumping speed	112
E.	Position of CPS beam tube sensors	113
F.	Simulation of a hardware failure	114
G.	Run list first tritium background rate analysis	115
List of Acronyms		117
List of Figures		119
List of Tables		121
Bibliography		123
Danksagung		139

1. Neutrino physics

1.1. First discovery

In the year 1930, Wolfgang Pauli postulated a neutral particle¹, which has a half-integer spin to account for the measured energy spectrum of the β -decay. At that time, the β -electron was expected to be mono-energetic similar to the α and γ -decay. If the electron is the only particle which results from the β -decay besides the daughter nuclei, it has to be mono-energetic. In 1934, Enrico Fermi published the name neutrino for the first time describing the β -decay as



with the mother nuclei ${}^A_Z\text{X}$, and the daughter nuclei ${}^A_{Z+1}\text{Y}$. Today this decay is known as a weak interaction, which has a cross section on the order of $\sigma < 10^{-44} \text{ cm}^2$.

More than 20 years later, Cowan and Reines started an experiment using a 200 ℓ water tank enriched with a cadmium chloride solution to directly detect a neutrino for the first time [RC53]. They considered the inverse β -decay



for an electron antineutrino reacting with a proton in the water. For the neutrino source, they located their tank close to a nuclear reactor. The neutron, which arises from the decay, is captured by a cadmium nucleus. When returning into the cadmium ground state, photons are emitted in the energy range of 3 MeV to 11 MeV. The positron of equation (1.2) quickly annihilates producing two γ 's with an energy of 511 keV each. For the detection of the γ 's, three liquid-scintillator chambers equipped with 110 photomultipliers surround the tank. In order to discriminate the signal of an inverse β -decay from other background signals, the 17 μs delay of the γ induced by the neutron (compared to the positron annihilation) is used. The measurement principle is summarized in figure 1.1. They achieved an event rate of about 3 events per hour and Reines was awarded a Nobel prize in 1995².

¹He called it "neutron" as the particle today known under this name was not yet detected.

²https://www.nobelprize.org/nobel_prizes/physics/laureates/1995/ (accessed on 21st April, 2019).

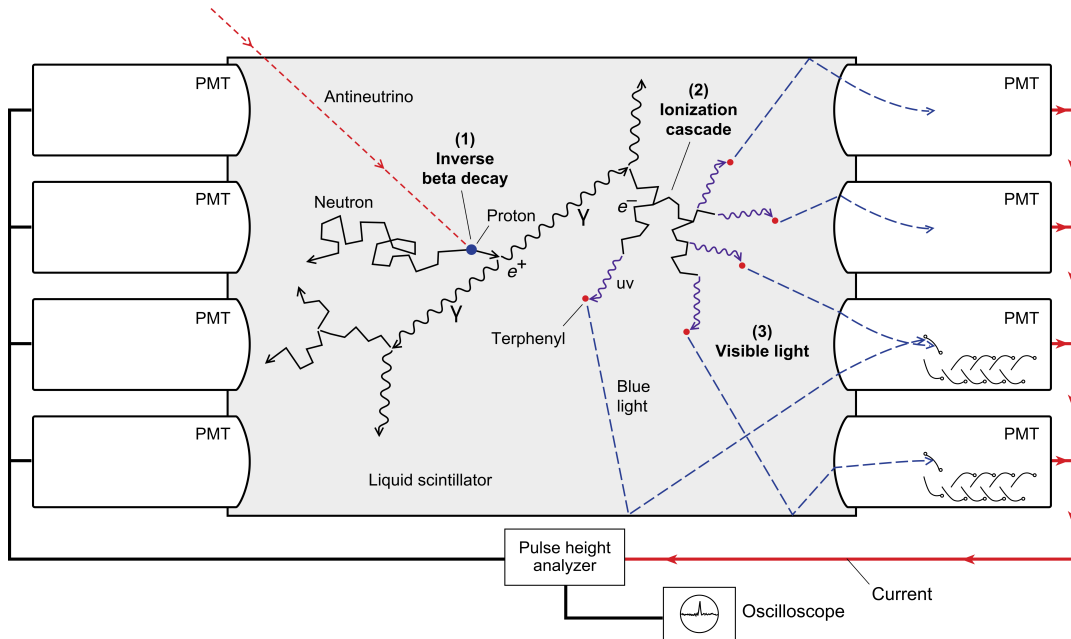


Figure 1.1.: Inverse beta-decay detection. The anti-electron neutrino reacts with a proton and decays into a neutron and a positron (1). The positron annihilates together with an electron and produces two γ 's. These γ 's produce secondary electrons via Compton scattering resulting in an ionization cascade (2). By the interaction with the scintillator the photons of the cascade produce light (3), which can be detected by PMTs. This figure is taken from [Coo].

The second neutrino flavor was discovered in the Brookhaven National Laboratory in 1962 by Lederman, Schwartz, and Steinberger. They investigated the pion decay

$$\pi^+ \rightarrow \mu^+ + \nu_\mu \quad \text{and} \quad \pi^- \rightarrow \mu^- + \bar{\nu}_\mu, \quad (1.3)$$

by shooting highly energetic protons onto a beryllium target. Behind the target, a 13.5 m long thick iron shield wall [DGG⁺62] was installed shielding all particles arising from the collisions except for neutrinos. In the detector behind the wall only muons were measured, therefore another neutrino generation has to exist in addition to electron neutrinos.

The final (as known today) neutrino flavor was detected in 2000. The measurement method was similar to the discovery of ν_μ ; a proton beam was shot at a tungsten target producing D_S mesons. The charged charmed mesons decay via

$$D_S^+ \rightarrow \tau^+ \nu_\tau \quad \text{and} \quad D_S^- \rightarrow \tau^- \bar{\nu}_\tau. \quad (1.4)$$

The τ were detected by identifying their typical kink in their trajectory in the detection plates (alternating nuclear emulsion and steel). A total of 4 τ events were found as published in reference [KUA⁺01].

To obtain the total number of neutrino generations, another measurement method can be used. With the collision of electrons and positrons at a center-of-mass energy of 91.2 GeV, Z^0 boson can be produced. The Z^0 can decay only in either a lepton anti-lepton pair, or a quark anti-quark pair in order to preserve all conservation

2.2 MeV u Up quark 2/3	1.3 GeV c Charm quark 2/3	173.0 GeV t Top quark 2/3	0 g Gluon 0	← Mass ← Symbol ← Name ← Electric charge
4.7 MeV d Down quark -1/3	95 MeV s Strange quark -1/3	4.2 GeV b Bottom quark -1/3	0 γ Photon 0	
511 keV e Electron -1	105.7 MeV μ Muon -1	1.8 GeV τ Tauon -1	91.2 GeV Z Z boson 0	
0 ν_e Electron neutrino 0	0 ν_μ Muon neutrino 0	0 ν_τ Tauon neutrino 0	80.4 GeV W W boson ±1	125.2 GeV H Higgs boson 0

Figure 1.2.: Particles in the standard model. The particles of the standard model are summarized with their corresponding mass and electric charge. The six quarks are surrounded with a blue box and the six leptons with a green one. These are all fermions with a spin of $1/2$. The intermediate vector bosons are displayed in gray and have a spin of 1. The Higgs boson is a spin 0 particle (in black). Note that neutrinos are massless in the standard model [THH⁺18].

numbers for weak interactions. By analyzing the decay products, all pairs can be detected except for the neutrinos. From the first comparison of the decay width measured at the LEP collider at CERN with the theoretical one, the number of neutrino flavors is found to be [D⁺89]

$$N_\nu = 3.27 \pm 0.30 . \quad (1.5)$$

This and other LEP results were combined with a new measurement performed at the Stanford Linear Collider leading to [EG06]

$$N_\nu = 2.9840 \pm 0.0082 . \quad (1.6)$$

Therefore, all results favor three neutrino generations which participate in the weak interaction.

1.2. Neutrinos in the standard model

In the standard model, the three neutrinos flavors are part of the six leptons. Each neutrino has a corresponding partner (e , μ , and τ) with which they build a generation. However, the neutrinos only interact weakly while their partner particles take part in weak and electromagnetic interactions. The six quarks are the only particles

which can interact via all the three forces. These twelve particles are fermions with a spin of $1/2$. The intermediate vector bosons of the strong and electromagnetic force are both massless. Due to the SU(3)-symmetry of the strong force, there are eight different gluons, which differ in the color they mediate. The electromagnetic force is described by a U(1) symmetry, which only has one vector boson namely the photon. In contrast to the other forces, the intermediate vector bosons of the weak interaction have a mass. Their mass originates from the spontaneous symmetry breaking in the Higgs mechanism [EB64, Hig64]. In 2012, this theory was confirmed by the discovery of the Higgs boson with a mass of 125.2 GeV [AAA⁺12, CKSea12].

The standard model neutrinos are massless (see figure 1.2), which arises from the measurement of parity violation in β -decays. Wu was the first person to investigate the parity in the weak interaction sector in 1957. She used a magnetized ^{60}Co β -source and measured that emission of the electrons anti-parallel to their nuclear spin is favored [WAH⁺57]. The maximum parity violation of the β -electrons was confirmed by other experiments within the following year [GLW57]. One year later, Goldhaber measured the helicity h of the neutrino, defined by

$$h = \frac{\vec{p} \cdot \vec{s}}{|\vec{p}| \cdot |\vec{s}|} , \quad (1.7)$$

with its momentum \vec{p} and its spin \vec{s} [GG58]. The measurement result revealed a helicity of $h_\nu = -1.0 \pm 0.3$ implying there are only left-handed neutrinos and right-handed anti-neutrinos. As the helicity is not Lorentz invariant, there is always a reference system in which the momentum is flipped, if the particle is massive. So with the result of $h_\nu = -1.0$, there is no evidence that neutrinos have a mass. Therefore, the neutrino mass is set to zero in the standard model.

However, a few years later experimental results hinted that neutrinos oscillate, which is a contradiction to the massless particle theory. These results are presented in section 1.3 and confirm that there has to be physics beyond the standard model in the neutrino sector.

1.3. Neutrino oscillation

The Nobel prize was awarded to McDonald and Kajita on behalf of the SNO and SuperKamiokande experiments in 2015. Not only this achievement demonstrates the importance of neutrino oscillations. Neutrino oscillations are only possible if neutrinos have a mass. In this section the theory of neutrino oscillation is described before the results of several experiments are given.

1.3.1. Theory

B. Pontecorvo was the first person who introduced the theoretical concept of neutrino oscillations in 1957 [Pon58, Pon57]. However, he described neutrinos oscillating into anti-neutrinos, a process which has not yet been detected. A few years later, the change from flavor states $|\nu_\alpha\rangle$ ($\alpha = e, \mu, \tau$) into mass states $|\nu_i\rangle$ ($i = 1, 2, 3$) has been included [MNS62, Pon68]. The flavor states can be described similarly to the Cabibbo-Kobayashi-Maskawa matrix [KM73]

$$|\nu_\alpha\rangle = \sum_i U_{\alpha i} |\nu_i\rangle \quad \text{and} \quad |\nu_i\rangle = \sum_\alpha U_{i\alpha}^* |\nu_\alpha\rangle , \quad (1.8)$$

with the unitary 3×3 matrix $U_{\alpha i}$, which is known as Pontecorvo-Maki-Nakagawa-Sakata matrix (PMNS matrix). The PMNS matrix elements are given by

$$U = \begin{pmatrix} U_{e1} & U_{e2} & U_{e3} \\ U_{\mu 1} & U_{\mu 2} & U_{\mu 3} \\ U_{\tau 1} & U_{\tau 2} & U_{\tau 3} \end{pmatrix} = \begin{pmatrix} c_{12}c_{13} & s_{12}c_{13} & s_{13}e^{-i\delta} \\ -s_{12}c_{23} - c_{12}s_{23}s_{13}e^{i\delta} & c_{12}c_{23} - s_{12}s_{23}s_{13}e^{i\delta} & s_{23}c_{13} \\ s_{12}s_{23} - c_{12}c_{23}s_{13}e^{i\delta} & -c_{12}s_{23} - s_{12}c_{23}s_{13}e^{i\delta} & c_{23}c_{13} \end{pmatrix} \cdot \begin{pmatrix} e^{i\alpha_1/2} & 0 & 0 \\ 0 & e^{i\alpha_2/2} & 0 \\ 0 & 0 & 1 \end{pmatrix}, \quad (1.9)$$

with $s_{jk} = \sin(\theta_{jk})$ and $c_{jk} = \cos(\theta_{jk})$ ($\theta_{j,k} = [0, \frac{\pi}{2}]$). The matrix has six free parameters, the Euler angles of the mass eigenstates $\theta_{j,k}$ and the phases δ , α_1 , α_2 . If neutrinos are not Majorana particles (particle and anti-particle are identical, see section 1.4.2.1.3), α_1 and α_2 can be set to zero. Including the three neutrino masses m_i , this leaves seven free parameters, which have to be measured.

In general the unitary matrix does not have to be three dimensional; additional neutrinos (e.g. a sterile neutrino, which does not interact weakly) can be included by another dimension. Consequently, the number of mixing angles and phases will increase.

As neutrinos will be detected during measurements after they have traveled for a certain time since their creation, the time evolution of $|\nu_\alpha\rangle$ has to be investigated. In the following, the calculations are described for only one direction x for simplicity.

For the time evolution, the Schrödinger equation has to be considered

$$\mathcal{H} |\nu_i(x,t)\rangle = i\hbar \cdot \frac{\partial}{\partial t} |\nu_i(x,t)\rangle. \quad (1.10)$$

Here \mathcal{H} is the free, time-independent Hamiltonian with its energy eigenvalues E_j . In this case the solution for $|\nu_\alpha\rangle$ is given by

$$|\nu_i(x,t)\rangle = e^{-\frac{i}{\hbar} \cdot (E_i t - p_i x)} |\nu_i\rangle. \quad (1.11)$$

In the next step, the time evolution of $|\nu_\beta(x,t)\rangle$ is expressed by the initial condition $|\nu_\alpha\rangle$ for $t = x = 0$

$$|\nu_\beta(x,t)\rangle \stackrel{(1.8)}{=} \sum_i U_{\alpha i} |\nu_i(x,t)\rangle \quad (1.12)$$

$$\stackrel{(1.11)}{=} \sum_i U_{\alpha i} e^{-\frac{i}{\hbar} \cdot (E_i t - p_i x)} |\nu_i\rangle \quad (1.13)$$

$$\stackrel{(1.8)}{=} \sum_{i,\beta} U_{\alpha i} e^{-\frac{i}{\hbar} \cdot (E_i t - p_i x)} U_{i\beta}^* |\nu_\alpha\rangle. \quad (1.14)$$

For the experiments, it is important to know the probability for the initial eigenstate to be oscillated into $|\nu_\beta(x,t)\rangle$ at the position x and the time t

$$\mathcal{P}(\nu_\alpha \rightarrow \nu_\beta)(x,t) = |\langle \nu_\alpha | \nu_\beta(x,t) \rangle|^2 = \sum_{i,j} U_{\alpha i} U_{j\alpha}^* U_{i\beta}^* U_{\beta j} e^{-\frac{i}{\hbar} \cdot (E_i t - p_i x)} e^{-\frac{i}{\hbar} \cdot (E_j t - p_j x)}. \quad (1.15)$$

In the following, the probability is transformed in order to leave it independent of the distance between the neutrino origin and detection L , the neutrino mass squared difference $\Delta m_{ij}^2 = m_i^2 - m_j^2$, and the energy E . First E_i has to be considered using the fact that neutrinos can be described in first approximation as relativistic particles traveling close to the speed of light

$$E_i = \sqrt{m_i^2 c^4 + p_i^2 c^2} = p_i c \cdot \sqrt{1 + \frac{m_i^2 c^2}{p_i^2}} \stackrel{(p_i \gg m_i)}{\simeq} p_i c \cdot \left(1 + \frac{m_i^2 c^2}{2p_i^2}\right) \stackrel{(p_i c \simeq E)}{\simeq} E + \frac{m_i^2 c^4}{2E}. \quad (1.16)$$

For the third transformation, Taylor's theorem is used. Under the same assumptions x can be expressed by

$$x = L = v \cdot t \simeq c \cdot t. \quad (1.17)$$

Using equations (1.16) and (1.17) for the exponent in equation (1.15) can be written as

$$E_i t - p_i x \stackrel{(1.16),(1.17)}{=} \left(E + \frac{m_i^2 c^4}{2E}\right) \cdot t - p_i \cdot L \stackrel{(1.17)}{=} \left(E + \frac{m_i^2 c^4}{2E}\right) \cdot \frac{L}{c} - \frac{E}{c} \cdot L = \frac{m_i^2 c^3 L}{2E}. \quad (1.18)$$

Applying equation (1.18) for the probability results in

$$\begin{aligned} \mathcal{P}(\nu_\alpha \rightarrow \nu_\beta)(x, t) &= \mathcal{P}(\nu_\alpha \rightarrow \nu_\beta)(L, E) = \sum_{i, j} U_{\alpha i} U_{j\alpha}^* U_{i\beta}^* U_{\beta j} e^{-\frac{i}{\hbar} \cdot \frac{\Delta m_{ij}^2 c^3}{2} \cdot \frac{L}{E}} \\ &= \sum_i \left| U_{\alpha i} U_{i\beta}^* \right|^2 + 2 \operatorname{Re} \sum_{j>i} U_{\alpha i} U_{j\alpha}^* U_{i\beta}^* U_{\beta j} e^{-\frac{i}{\hbar} \cdot \frac{\Delta m_{ij}^2 c^3}{2} \cdot \frac{L}{E}}. \end{aligned} \quad (1.19)$$

The probability consists of two terms, the first one represents the average transition probability, which is constant. The second one contains the oscillation part and is dependent on E , L , and Δm_{ij}^2 . Following equation (1.19), there is no possibility to gain information on the absolute neutrino mass from oscillations. At the same time, the mass difference of the mass eigenstates has to be non-zero in order to perform an oscillation.

There are two possibilities for an experiment to measure neutrino oscillations; the appearance and the disappearance channel. Equation (1.19) gives the probability for the appearance channel. For the second channel holds

$$P(\nu_\alpha \rightarrow \nu_\alpha) = 1 - \sum_\beta P(\nu_\alpha \rightarrow \nu_\beta). \quad (1.20)$$

If only two neutrino flavors are considered, equation (1.19) can be simplified to

$$\mathcal{P}(\nu_\alpha \rightarrow \nu_\beta)(L, E) = \sin^2(2\theta) \sin^2 \left(\frac{\Delta m^2 c^3 L}{4\hbar E} \right), \quad (1.21)$$

now with a 2×2 mixing matrix

$$U = \begin{pmatrix} \cos \theta & \sin \theta \\ -\sin \theta & \cos \theta \end{pmatrix}. \quad (1.22)$$

Equation (1.21) shows the importance of the length-energy ratio. These two parameters have to be considered in the planning of an oscillation experiment. Therefore the characteristic oscillation length can be introduced

$$L_{\text{osz}} = \frac{4\pi \hbar E}{\Delta m^2 c^3}. \quad (1.23)$$

Three cases have to be distinguished

- $L \ll L_{osz}$: No oscillation signal is measured since the distance from source to detector is too small for an oscillation.
- $L \approx L_{osz}$: This is the optimal distance for a detector to be most sensitive.
- $L \gg L_{osz}$: Only the average transition probability can be measured as there are too many oscillations.

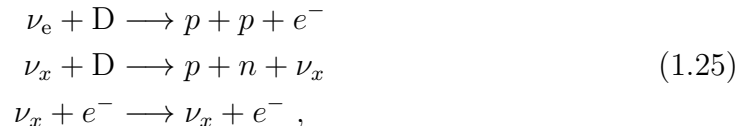
1.3.2. Experiments

The first experiment which detected neutrino oscillations was the Homestake experiment in 1970. With the aim to prove the calculated solar neutrino flux by Bahcall [Bah64], the experiment started in 1964. A tank with a volume of 615 t was filled with C_2Cl_4 to investigate the inverse β -decay of chlorine [Dav94]



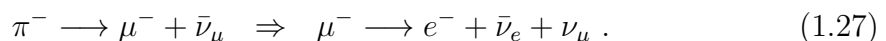
In this radiochemical experiment, neutrinos can be detected via purging the tank with helium and analyzing the number of argon atoms by extraction. Therefore, the reverse reaction of equation (1.24) was used [Dav94]. With this measurement method, there is no continuous measurement possible as it has to be interrupted for this analysis. The results showed that only a third of the expected neutrino rate was detected [Dav94].

In 2001, a different approach enabled detection of the missing electron neutrino rate. The Sudbury Neutrino Observatory (SNO) experiment used a 1000 t volume of heavy water (D_2O). In contrast to chlorine, not only the charged current reaction can be detected, but also the neutral current one. Additionally the scattering of neutrinos with electrons was used [A⁺13]



with ν_x including the three neutrino flavors. The three reactions were measured in different campaigns because the experiment setup had to be slightly changed. The result of the first reaction confirmed the Homestake experiment observations by measuring a large electron neutrino deficit compared to the expected solar neutrino flux. However including the detection of the neutral current reactions, the number of events is close to the expected neutrino flux [A⁺13]. Therefore, the neutrino flavors have to change on the way from the sun to the detector.

At the same time, the Super-Kamiokande experiment tried to detect the neutrino flux arising from the pion-decay of radiation showers. These pions will decay into muon and electron neutrinos by [Zub12]



Therefore a ratio of 2 muon neutrinos to 1 electron neutrino was expected. For the detection, a 50 000 t water tank is used [FHI⁺98]. An incoming electron or muon neutrino can react via the charged current with the water and will produce Cherenkov

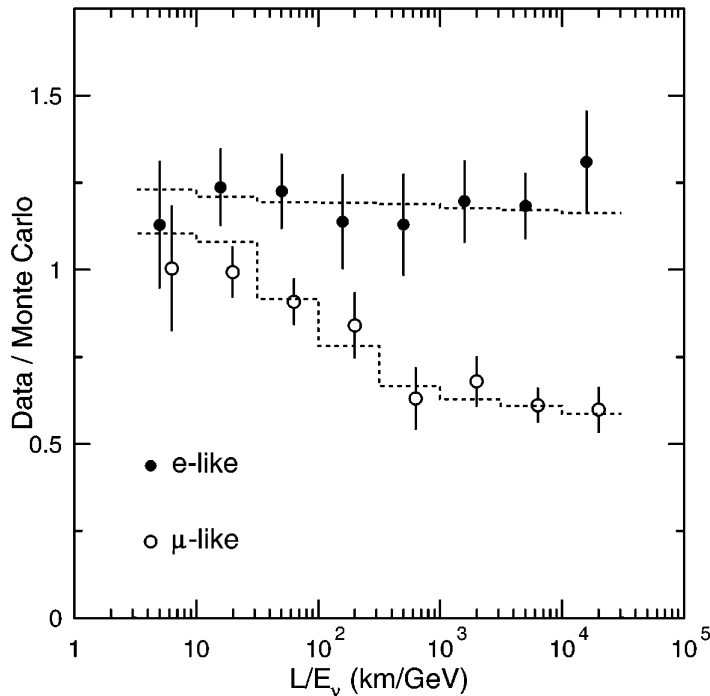


Figure 1.3.: SuperKamiokande result. The ratio of measured events to Monte Carlo data is plotted over the length-energy ratio. For the Monte Carlo data no oscillations were assumed. While the measured electron rate is rather constant (excluding detector effects [FHI⁺98]), the muon rate shows a deficit for larger L/E_ν . This can be explained by the oscillation into tau neutrinos [FHI⁺98].

rings. These rings were detected via photomultipliers; the muons produce a sharper ring compared to the electrons and they can therefore be distinguished [HKK⁺88]. The direction of the incoming neutrino can be detected via the signal of the charged particle in the tank.

The result can be seen in figure 1.3. A muon deficit is measured in dependence of the zenith angle [FHI⁺98]. For neutrinos traveling through the earth, the number of muon neutrinos is too small. If only the measured neutrinos with short travel distances are used, the expected ratio of 2:1 (muon to electron) is measured. This can be explained by the oscillation from muon to tau neutrinos [FHI⁺98].

Another test for neutrino oscillations can be made with reactor neutrinos with energies up to 8 MeV. With at least one detector close to the reactor and one of a distance of about 1 km to 2 km, an experiment is sensitive for $\sin \theta_{13}$ [Zub12]. Three experiments have been built to perform such a measurement: the Double Chooz Experiment [TAA⁺16], the Daya Bay Experiment [ABB⁺17], and the Reactor Experiment for Neutrino Oscillation (RENO) [CCC⁺16]. The measurement method is similar to the experiment of Cowan and Reines using the inverse β -decay (see equation (1.2)). The most recent measured values are summarized in table 1.1. Solar neutrinos in the MeV-energy range were the first source to provide the values of $\sin^2(\theta_{12})$ and Δm_{12}^2 . Δm_{12}^2 is in $10^{-5} \text{ eV}^2/c^4$ range and therefore the mass difference of m_1 and m_2 has to be small with $m_1 < m_2$, which is determined from the Mikheyev-Smirnov-Wolfenstein (MSW) effect with the large mixing angle (LMA)

Table 1.1.: Measured values for the neutrino oscillation parameters. The values are obtained by various experiments [THH⁺18]. The normal and inverted mass hierarchy are used to determine $\sin^2(\theta_{23})$ and $|\Delta m_{32}^2|$. The results for the phase angle δ are not listed since it has not been determined.

Parameter	Value	Neutrino source
$\sin^2(\theta_{12})$	$0.307^{+0.013}_{-0.012}$	sun, reactor, accelerator
Δm_{12}^2	$(7.53 \pm 0.18) \cdot 10^{-5} \text{ eV}^2/c^4$	sun, reactor, accelerator
$\sin^2(\theta_{23})$ ($\Delta m_{32}^2 > 0$)	$0.417^{+0.025}_{-0.028}$	atmospheric, accelerator
$\sin^2(\theta_{23})$ ($\Delta m_{32}^2 < 0$)	$0.597^{+0.024}_{-0.030}$	atmospheric, accelerator
$ \Delta m_{32}^2 $	$(2.51 \pm 0.05) \cdot 10^{-3} \text{ eV}^2/c^4$	atmospheric, accelerator
$\sin^2(\theta_{13})$	0.0212 ± 0.0008	reactor

solution [Wol78, MS86]. The mixing angle of $\theta_{12} \approx 33^\circ$ is relatively large.

With the measurement of atmospheric neutrinos, it is not possible to distinguish if m_2 or m_3 is larger. This is the reason why the results for $\theta_{23} \approx 44^\circ$ list two possibilities. θ_{23} is the largest mixing angle, while $\theta_{13} \approx 10^\circ$ is the smallest one.

With the oscillation measurement results, there are three possibilities for the neutrino masses:

- **Normal hierarchy:** $m_1 < m_2 \ll m_3$
- **Inverted hierarchy:** $m_3 \ll m_1 < m_2$
- **Quasi degenerate:** $m_1 \approx m_2 \approx m_3 \approx m_0$

The normal and inverted hierarchies are shown in figure 1.4. The determination of the correct hierarchy is the goal of various neutrino mass experiments in the 2020s. The planned experiments and their measurement principle can be found in [QV15]. One example is the Jiangmen Underground Neutrino Observatory (JUNO), which aims to use reactor neutrinos to measure the electron anti-neutrino channel with a high precision. Data taking should start in 2020 and is planned to run for six years leading to a sensitivity of 3σ to 4σ [AAA⁺16].

1.4. Neutrino mass

In this section, a neutrino mass mechanism is introduced which could explain the small neutrino masses. Furthermore, several experiments are described, which aim to measure the neutrino mass.

1.4.1. Neutrino mass generation

All massive particles of the standard model obtain their mass via coupling with the Higgs field ϕ . The SU(2) gauge transformations result in several ground states for the Higgs field. A common way is to choose the ground state to be

$$\langle \phi \rangle = \frac{1}{\sqrt{2}} \begin{pmatrix} 0 \\ v \end{pmatrix}, \quad (1.28)$$

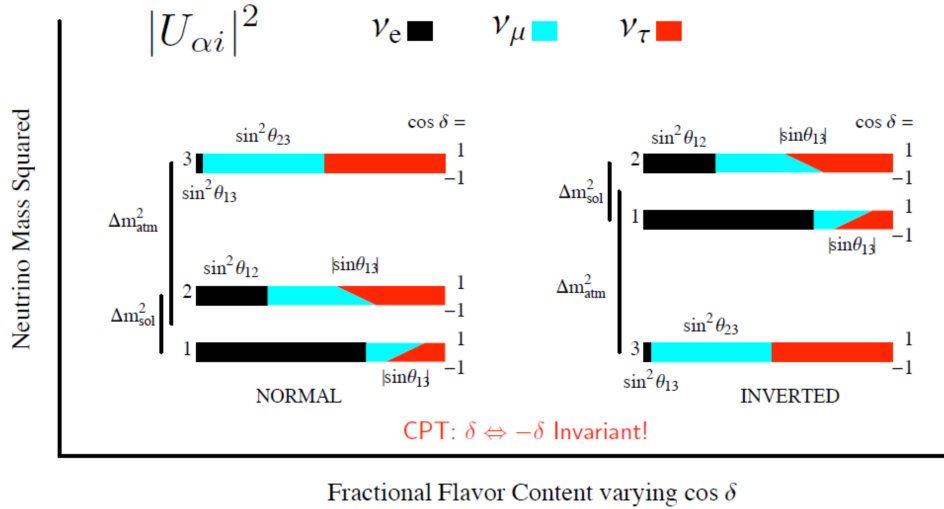


Figure 1.4.: Neutrino mass hierarchy. The normal (left) and inverted hierarchy (right) for the neutrino mass states are shown. The different colors indicate the neutrino flavors. The influence of the phase angle can be seen in mass eigenstates 1 and 2. The mixing angles, which have been used for the ratio are illustrated. The plot is taken from [Par06].

with its vacuum expectation value v [PS95]. v is the only free parameter and is determined by the Higgs boson mass. For the Lagrangian \mathcal{L}_f the Yukawa type coupling of the fermions to the Higgs field has to be introduced [PS95]

$$\mathcal{L}_f(\phi, A, \psi) = \bar{\psi} \gamma^\mu D_\mu \psi + G_\psi \bar{\psi} \phi \psi . \quad (1.29)$$

D_μ is the gauge covariant derivative. Since the fermion particles of the standard model have a spin of $1/2$, the Dirac equation has to be used to describe particle's wave function

$$(i\not{\partial} - m)\psi = 0 , \quad (1.30)$$

with the particle mass m . By introducing right- and left-handed currents in equation (1.29) the fermion field can be described as

$$\psi = \psi_L + \psi_R . \quad (1.31)$$

Using equation (1.31) and the Euler-Lagrange mechanism on equation (1.29), the equation of motions for the Higgs field are found to be [PS95]

$$i\not{\partial}\psi_L - G_\psi \frac{1}{\sqrt{2}} \begin{pmatrix} 0 \\ v \end{pmatrix} \psi_R = 0 . \quad (1.32)$$

By comparing equations (1.30) with (1.32), the mass can be obtained. Additionally, equation (1.32) shows that there has to be right-handed fermions in order to have a mass, which contradicts the helicity measurements (see section 1.2). However, neutrino oscillation is only possible if they are massive. With the introduction of a right-handed neutrino field ν_R , which does not interact weakly, both problems could be solved. In this case, an additional Yukawa coupling would have to be added to

account for the very small neutrino masses (several orders of magnitude lower than the other SM particles).

As an alternative to the Dirac coupling, another mass generation mechanism can be introduced. A combination of the see-saw mechanism with Majorana neutrinos is a good candidate to solve the problem of the tiny masses [GMRS79, Yan80, MSac80, SV80]. Therefore two additional mass terms m_L and m_R have to be added to the Dirac Lagrangian mass term. If only one neutrino flavor is considered, the Lagrangian is given by

$$\begin{aligned} \mathcal{L} &= \frac{1}{2}m_D(\bar{\psi}_L\psi_R + \bar{\psi}_L^C\psi_R^C) + \frac{1}{2}m_L\bar{\psi}_L\psi_R^C + \frac{1}{2}m_R\bar{\psi}_L^C\psi_R + \text{h.c.} \\ &= \begin{pmatrix} \bar{\psi}_L & \bar{\psi}_L^C \end{pmatrix} \begin{pmatrix} m_L & m_D \\ m_D & m_R \end{pmatrix} \begin{pmatrix} \psi_R^C \\ \psi_R \end{pmatrix} + \text{h.c.} . \end{aligned} \quad (1.33)$$

In the see-saw mechanism, the two assumptions $m_L \approx 0$ and $m_R \gg m_D$ are made [GMRS79, Yan80, MSac80, SV80]. Calculating the eigenvalues of the matrix results in the measurement mass observables

$$m_1 = \frac{m_D^2}{m_R} \quad \text{and} \quad m_2 \approx m_R \quad (1.34)$$

This would leave m_1 in the (sub-)eV range, while m_2 could possibly be the mass of a sterile neutrino. Additionally to the mass terms, a small mixing angle between the left- and right-handed neutrinos is introduced by this method [GMRS79, Yan80, MSac80, SV80], which can be calculated to

$$\tan 2\theta = 2 \cdot \frac{m_D}{m_R} . \quad (1.35)$$

This mechanism can explain the active neutrino flavor (interacting weakly) ν_L to consist mainly of ν_1 and the (sterile) neutrino ν_R to consist mainly of ν_2 . There are several experiments, which hint to the existence of sterile neutrinos (e.g. see [DHCK⁺17]) but do not yet have sufficient sensitivity. Still the see-saw mechanism stays as one of most promising candidates for the neutrino mass generation.

1.4.2. Neutrino mass experiments

The neutrino oscillation experiments described in section 1.3 are only sensitive to the difference of the mass squared. Therefore, other measurement methods are needed to gain information about the absolute neutrino mass. In this section first model dependent methods are described, then model independent methods are explained.

1.4.2.1. Model dependent measurement

There are three different possibilities to measure the neutrino mass in a model-dependent way. These are described in the following.

1.4.2.1.1. Cosmology

The strongest model dependent limit on the neutrino mass is obtained by cosmological measurements. A cosmological model has to be chosen, which describes the early

universe. The most favored one is the Λ CDM model, which was used for the analysis of the Cosmic Microwave Background (CMB). Similar to the microwave background by photons, there is one for neutrinos [Sch06]. Approximately 0.1 s after the Big Bang, neutrinos decoupled from the plasma, marking the time when the interaction rate of the weak force is smaller than the Hubble expansion rate.

Using the Λ CDM model, the most relevant measurement observables are the temperature anisotropies of the CMB radiation spectrum (most recent from the Planck satellite [A⁺18a]), the mass power spectrum (most recent from the Sloan Digital Sky Survey data), and a probe of the large scale structure of the universe [LP12]. Due to the strong influence on the model, only a range of upper limits can be given [YPDBdMdB17]

$$\sum_i m_i \lesssim 0.1 \text{ eV to } 0.8 \text{ eV} \quad (1.36)$$

For the sensitivity of 100 meV, several independent data samples are additionally used for example Lyman alpha forest measurements [YPDBdMdB17]. However, more than 10 free parameters have to be fit to obtain the result, which underlines the importance of a model independent measurement. Furthermore, cosmology measurements are only sensitive to the total sum of the neutrino masses and therefore require additional measurements for the individual masses.

1.4.2.1.2. Supernova neutrinos

If a supernova happens, a large number of neutrinos are emitted isotropically in the MeV-range. Within the first 10 s, the neutrinos carry away over 99% of the energy available from the supernova [Per08]. There are two production mechanisms, which have to be considered in the analysis

$$p + e^- \rightarrow n + \nu_e, \quad (1.37)$$

$$e^+ + e^- \rightarrow \nu_\alpha + \bar{\nu}_\alpha. \quad (1.38)$$

The sensitivity on the neutrino mass is given by the time difference Δt , in which the neutrinos are detected. The time difference of the emitted neutrinos can be calculated to [Per08]

$$\Delta t = t_1 - t_2 = \Delta t_0 + \frac{Lc^3 m^2}{2} \left(\frac{1}{E_2^2} - \frac{1}{E_1^2} \right). \quad (1.39)$$

From measurements of Δt , E_1 , and E_2 (energy of the neutrinos) by a detector and the determination of the distance from the supernova to the earth L by another astroparticle physics method (for example gamma-rays), the neutrino mass can be analyzed. The model dependent part is Δt_0 , which is described by the supernova process [Per08]. The large uncertainty mainly arises from the model used to determine Δt_0 .

SN1987A was the first supernova that occurred when experiments were running on the earth which could detect neutrinos. Both the IMB detector (8 neutrinos within 6 s and an energy between 20 MeV to 40 MeV) [BBB⁺87] and the Kamiokande-II detector (12 neutrinos within 13 s and an energy between 5 MeV to 35 MeV) [HKK⁺88] have been used to analyze the neutrino mass. In 2002, they published a result with a mass limit of [LL02]

$$m_\nu \leq 5.7 \text{ eV (95\% C.L.)}. \quad (1.40)$$

1.4.2.1.3. Neutrinoless double beta decay

In 1935, double beta decay was predicted by Goeppert-Mayer [GM35]. In case that single β -decay is forbidden, a double β -decay can happen if it is energetically favorable. The possible decays can be calculated by using the Bethe-Weizsäcker mass formula [Wei35]. In general a decay only happens, when the binding energy of the daughter nuclei is larger than that of the mother nuclei. By fixing the mass number A , the binding energy plot describes a parabola, with a minimum for the stable nuclei (the highest binding energy). If A is even, there are two parabolas, one for an even neutron number N and proton number Z , the second one for the odd case.

Double beta decay is a second order process of the weak interaction resulting in a long lifetime (more than 10^{20} y) of the nuclei [Zub12]. In the standard model, the rare process is described by

$${}^A_Z N \rightarrow {}^A_{Z+2} N' + 2e^- + 2\bar{\nu}_e \quad \text{or} \quad {}^A_Z N \rightarrow {}^A_{Z-2} N' + 2e^+ + 2\nu_e . \quad (1.41)$$

The first events from the decay of ${}^{82}\text{Se}$ into ${}^{82}\text{Kr}$ were detected in 1969 [KM69]. If lepton number is violated, there is a second possibility for the decay, which was introduced by Furry [Fur39]. In this case, no neutrinos are emitted leading to

$${}^A_Z N \rightarrow {}^A_{Z+2} N' + 2e^- \quad \text{or} \quad {}^A_Z N \rightarrow {}^A_{Z-2} N' + 2e^+ . \quad (1.42)$$

This is only possible if neutrinos are Majorana particles i.e. the anti-particle and particle are the same. As this decay violates lepton number, it would be physics beyond the standard model. Additionally, the Majorana neutrinos have to be massive since they would have to be right-handed and left-handed in order to account for the helicity [Zub12].

Both cases can be distinguished by their β -electron spectrum shape (see figure 1.5). A nominal $2\nu\beta\beta$ -decay spectrum is continuous missing the energy of the neutrinos. For the $0\nu\beta\beta$ -decay, the measured spectrum would be mono-energetic at the Q value. The sensitivity of the experiment is strongly dependent on the unknown half-life time $t_{1/2}^{0\nu}$. Together with the phase space factor $G^{0\nu\beta\beta}$ and the nuclear matrix element $M^{0\nu\beta\beta}$, the Majorana neutrino mass is derived by

$$\langle m_{\beta\beta} \rangle^2 = \left| \sum_{i=1}^3 U_{ei}^2 m_i \right|^2 = \frac{m_e^2}{G^{0\nu\beta\beta} \cdot |M^{0\nu\beta\beta}|^2 \cdot t_{1/2}^{0\nu}} . \quad (1.43)$$

Since the $\langle m_{\beta\beta} \rangle^2$ is derived by the coherent sum of the neutrino mixing matrix elements U_{ei} multiplied by the neutrino masses m_i , the Majorana phases α_1 and α_2 (see section 1.3) may play a major role for the total value of $m_{\beta\beta}$. As the uncertainty on $M^{0\nu\beta\beta}$ is large for nuclei decaying via double beta decay, the published results have a large error band. The most recent results are given by KamLAND-Zen [GGH⁺16], Majorana [AAA⁺18a], GERDA [ABB⁺18], EXO-200 [A⁺14], and CUORE [AAA⁺18b] and lead to an upper limit of

$$m_{\beta\beta} \lesssim 0.06 \text{ eV to } 0.52 \text{ eV} . \quad (1.44)$$

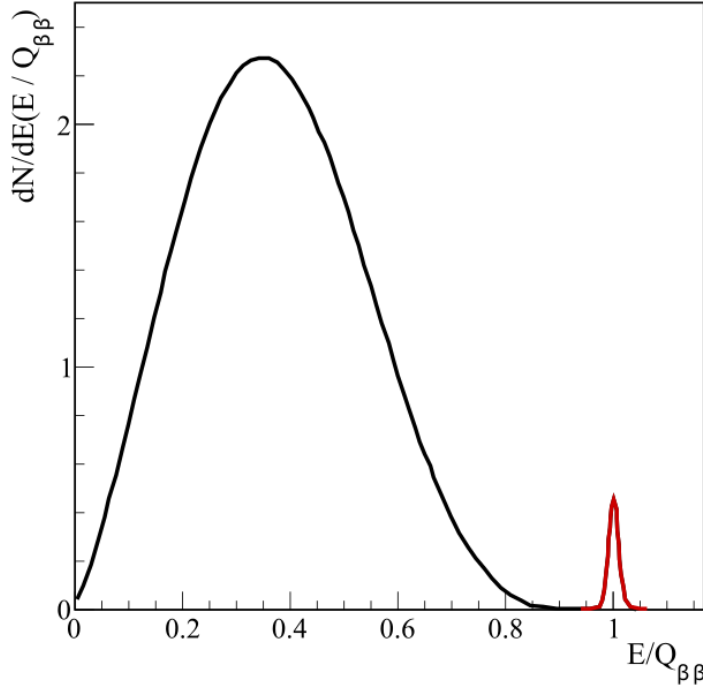


Figure 1.5.: Neutrinoless double beta-decay spectrum. In black the spectrum of the $2\nu\beta\beta$ -decay is plotted, in red the one of the $0\nu\beta\beta$ -decay. The plot is based on [WS12].

1.4.3. Model independent measurements

For a model independent measurement, only kinematics of a decay are used in which an electron, a muon, or a tau with its corresponding partner neutrino is produced. By measuring the energy of the charged lepton, energy conservation is used to obtain information about the neutrino mass. The simplest possibility would be the neutron decay

$$n \rightarrow p + e^- + \bar{\nu}_e . \quad (1.45)$$

In order to be sensitive enough, the energy of the electron has to be measured precisely, for example, with a spectroscopy method.

In figure 1.6, the influence of neutrino mass on the β spectrum can be seen on the right side. At the endpoint the event rate is proportional to E_0^{-3} , which is the reason why the endpoint energy of the β -emitter has to be small. Additionally, the energy resolution of the measurement setup has to be in the sub-eV range to be sensitive to the small neutrino mass. By using Fermi's Golden Rule [Fer34, KBD⁺18], the differential β -spectrum can be derived

$$\frac{d^2 N}{dt dE} = \frac{G_F^2 \cdot \cos^2 \theta_C \cdot |M|^2}{2\pi^3} \cdot F(Z+1, E) \cdot p \cdot (E + m_e) \cdot (E_0 - E) \cdot \sqrt{(E_0 - E)^2 - m_{\bar{\nu}_e}^2} \cdot \Theta(E_0 - E - m_{\bar{\nu}_e}) , \quad (1.46)$$

with

- G_F : Fermi constant
- θ_C : Cabibbo angle

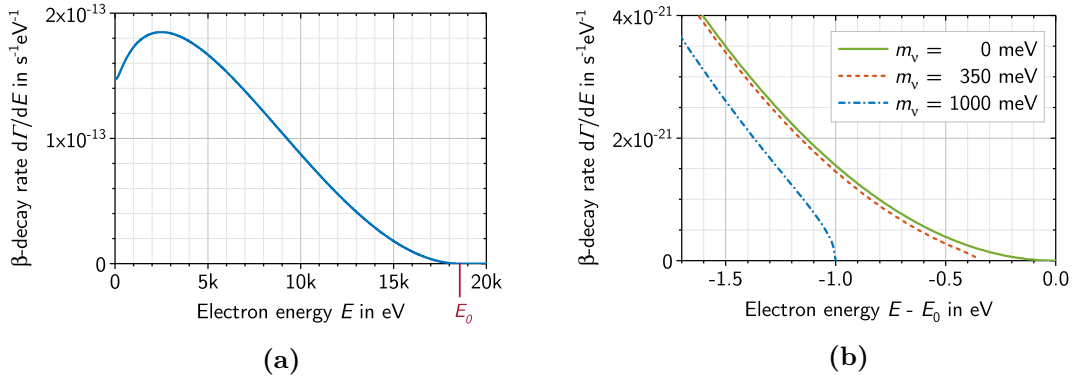


Figure 1.6.: Tritium β -spectrum. (a) The complete β -spectrum. The corresponding endpoint energy is marked in red. (b) Zoom into the region below the endpoint. The deviations in the spectrum for two different neutrino masses are plotted compared to a massless neutrino. The figures are adapted from [KBD⁺18].

- M : transition matrix element
- $F(Z+1, E)$: Fermi function, which considers the Coulomb interaction between daughter nuclei and electron
- E : kinetic energy of the electron
- p : momentum of the electron
- E_0 : endpoint of the β -spectrum, which is the maximal energy for an β -electron. If the nuclear recoil is neglected, E_0 is equal to the total decay energy Q .

The Heaviside step function Θ ensures that a neutrino can only be emitted if enough energy is left for its mass.

The square root in equation (1.46) shows that the fit measurement observable is the electron anti-neutrino mass squared, which is defined by

$$m_{\bar{\nu}_e}^2 = \sum_i |U_{ei}|^2 m_i^2 . \quad (1.47)$$

It has to be noted that due to $|U_{ei}|^2$ the Majorana phases have not to be considered (compared to the neutrinoless double β -decay), meaning the measurement is model independent.

By using the pion decay

$$\pi \rightarrow \mu + \nu_\mu , \quad (1.48)$$

the effective muon neutrino mass can be analyzed. Similar to the β -decay, the energy of the muon has to be measured in order to get information of m_{ν_μ} . The current limit is given by [ABD⁺96]

$$m_{\nu_\mu} \leq 0.17 \text{ MeV (90\% C.L.)} . \quad (1.49)$$

For the analysis of the tau neutrino mass, there are two decay channels of the tau to be considered

$$\tau^- \rightarrow 2\pi^- + \pi^+ + \nu_\tau \quad \text{and} \quad \tau^- \rightarrow 3\pi^- + 2\pi^+ (+\pi^0) + \nu_\tau . \quad (1.50)$$

In the decay products, pions are generated, which decay again. As the pion energy is important for the mass analysis, the sensitivity is worse. In 1998 a result was published with a limit of [BBD⁺98]

$$m_{\nu_\tau} \leq 18.2 \text{ MeV (95\% C.L.)} . \quad (1.51)$$

In the following, the focus is on the β -decay experiments leading to a sensitivity improvement by several orders of magnitude compared to the tau neutrino mass measurement since the cosmology results suggest that neutrino mass is in the meV-range.

1.4.3.1. Rhenium and holmium as β -emitters

The β -emitter ^{187}Re has the lowest endpoint energy with $Q = 2.47 \text{ keV}$ [SAB⁺04] and would be a good candidate for a neutrino mass measurement. However, the half-life time of $4.32 \times 10^{10} \text{ y}$ is relatively large due to the fact that the decay is not super allowed. Therefore, a huge amount of ^{187}Re would be required since the activity is relatively small. The measurement set-up typically consists of a cryogenic bolometer. When a decay occurs, the released energy leads to a temperature increase in the bolometer. The temperature difference can be used to determine the β -electron energy [Nuc12]. The results provide a neutrino mass limit of [Nuc12]

$$m_{\bar{\nu}_e} < 15 \text{ eV (90\% C.L.)} . \quad (1.52)$$

If the challenges with solid state effects can be solved, the MARE experiment plans to achieve a sensitivity in the eV-range [Nuc12].

In another approach, the electron capture of ^{163}Ho is used, which has a Q-value of 2.83 keV [EBB⁺15]. Similar to the β -decay, the experiments have to be sensitive close to the endpoint to determine the neutrino mass [LV11]. The ECHo [GBC⁺17] and HOLMES experiments [NAB⁺18] both use cryogenic micro-calorimeters with a detector readout by microwave SQUID multiplexing. ECHo aims to reach sub-eV sensitivity by using 10^5 detectors [DHMW13]. For a sensitivity below 2 eV , 1024 detector pixels are necessary for the HOLMES experiment [NAB⁺18].

1.4.3.2. Tritium as a β -emitter

The best limit on the effective neutrino mass with a model independent measurement was analyzed with a tritium source. Tritium is an isotope of hydrogen with two additional neutrons which decays into helium



Compared to other isotopes using tritium for neutrino mass analysis has several advantages:

- **Short half-life:** The half-life of tritium is 12.3 y [JBD67], which leads to a higher activity in contrast to rhenium and holmium.
- **Low endpoint energy:** 18.6 keV is the second lowest endpoint energy for a β -emitter. Together with the short half-life, a rate of approximately $2 \times 10^{-13} \text{ s}$ is reached close to the endpoint.

- **Simple atomic structure:** As tritium nuclei only consists of one proton and two neutrons, the probability for inelastic scattering is low. Additionally, the calculation of the correction terms (for example, the interaction between β -electrons and emitter) is relatively easy.
- **Super-allowed transition:** The nuclear matrix element is energy independent. Therefore, the β -spectrum is completely defined by the free phase space. Furthermore, the matrix element $|M|^2 = 5.55$ [RK88] is relatively large.
- **Gaseous phase:** The influence of solid state effects can be neglected if gaseous tritium is used at a temperature of 30 K (see section 2.2.1).

However in the gaseous phase, tritium is a molecule. Therefore, different excitations and final states before and after the decay have to be considered [KAT05]. Using the molecular form, the reaction equation has to be modified



Previous experiments in Mainz [Ott94] and Troitsk [LS85b] have used tritium to obtain a limit on the effective neutrino mass. The combined result leads to the current mass limit of [THH⁺18]

$$m_{\bar{\nu}_e} < 2.0 \text{ eV (95\% C.L.)} . \quad (1.55)$$

2. The Karlsruhe TRItium Neutrino Experiment

The KATRIN experiment is designed to measure the effective neutrino mass model independently with a sensitivity of 0.2 eV (90% C.L.). In the following, the measurement principle and the experimental setup are described.

2.1. KATRIN measurement principle

In KATRIN, the tritium induced β -decay

$$\text{T}_2 \longrightarrow \left({}^3\text{HeT}\right)^+ + e^- + \bar{\nu}_e \quad (2.1)$$

is used in order to measure the absolute scale of the effective neutrino mass $m_{\bar{\nu}_e}$. According to Fermi's Golden Rule the decay rate is given by [KBD⁺18]

$$\begin{aligned} \frac{d\Gamma}{dE} = & \frac{G_F^2 \cdot |V_{ud}|^2 \cdot |M_{\text{nuc}}|^2}{2\pi^3} \cdot F(Z, E) \cdot p \cdot (E + m_e) \\ & \cdot \sum_f P_f \cdot (E_0 - V_f - E) \cdot \sqrt{(E_0 - V_f - E)^2 - m_{\bar{\nu}_e}^2} \cdot \Theta(E_0 - V_f - E - m_{\bar{\nu}_e}) , \end{aligned} \quad (2.2)$$

with the Fermi coupling constant G_F , the CKM matrix element V_{ud} , the nuclear transition matrix element M_{nuc} , the Fermi function $F(Z, E)$, the electron's momentum p , its kinetic energy E , its mass m_e , the tritium endpoint energy $E_0 = (18\,574.00 \pm 0.07)$ eV [OW08, MWKW15], the additional energy V_f of the final states f , and the transition probability P_f to a state f in the daughter molecule.

As previous neutrino mass experiments in Mainz and Troitsk [KBB⁺05, ABB⁺11] gave results for an upper limit of 2 eV, the KATRIN experiment was designed to increase the sensitivity by one order of magnitude. Considering equation (2.2) the observable is the neutrino mass squared, which means the actual sensitivity has to be improved by a factor of 100. Therefore, a stable β -source with a high activity circulating 40 g of tritium per day, as well as a high resolution spectrometer was

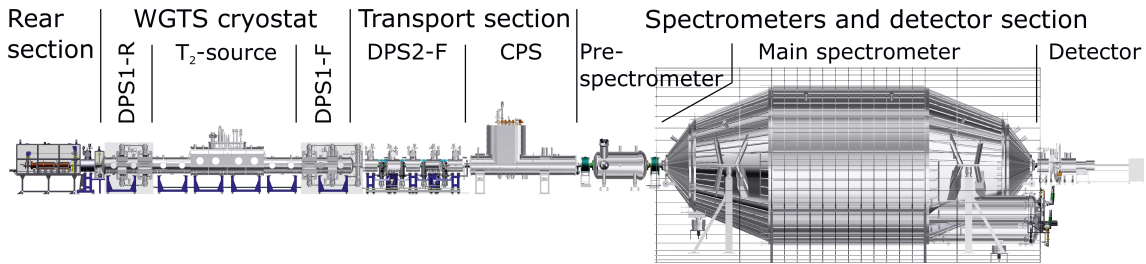


Figure 2.1.: KATRIN beamline. Overview of the 70 m long KATRIN experiment. The components are described in the text. Figure is taken from [A⁺18c].

designed to reach this ambitious goal. In KATRIN the integrated β -spectrum is measured. Consequently, the observable is the measured rate [KBD⁺18]

$$\dot{N}(t) = \frac{1}{2} \cdot N_T \int_{qU}^{E_0} \frac{d\Gamma}{dE} \cdot R(E,U) dE , \quad (2.3)$$

which is dependent on the number of tritium nuclei in the source N_T , and the response function $R(E,U)$ for a specific electrostatic potential U set at the main spectrometer. Hence, any instability in N_T or U directly translates into a systematic uncertainty on the measured rate and ultimately on the measured neutrino mass. The following section 2.2 describes the major KATRIN components, which have been installed for providing sufficiently stable experimental conditions.

2.2. Major components of the KATRIN experiment

The KATRIN beamline is 70 m long and can be subdivided into several components, which can be seen in figure 2.1. These components were combined to a complete beamline for the first time in 2016 and afterwards inaugurated with the First Light campaign. Within this campaign the alignment as well as ion characterization measurements were performed [A⁺18c]. The next milestone was the injection of krypton-83m into the KATRIN source at a temperature of 100 K. Measuring the discrete line spectrum of this krypton isotope provided a nuclear standard for important calibration purposes and investigating the stability of the source and high voltage parameters [A⁺18b]. Finally, the first tritium gas has been introduced into the system in May 2018.

In general, tritium is injected into the windowless gaseous tritium source (WGTS) via the loop system, and continuously pumped out at both ends of WGTS and in the transport section, consisting of the differential pumping section (DPS) and the cryogenic pumping section (CPS). On the rear side of the experiment, there are calibration (electron gun) and monitoring (rear wall and beta induced X-ray spectrometry (BIXS) detectors) devices. The electrons originating from β -decay are magnetically guided towards the spectrometer section by a series of superconducting magnets [A⁺18d]. Here, they are energetically filtered by the magnetic adiabatic collimation combined with an electrostatic filter (MAC-E filter) method. Finally, the electrons overcoming this electrostatic barrier are counted on the detector.

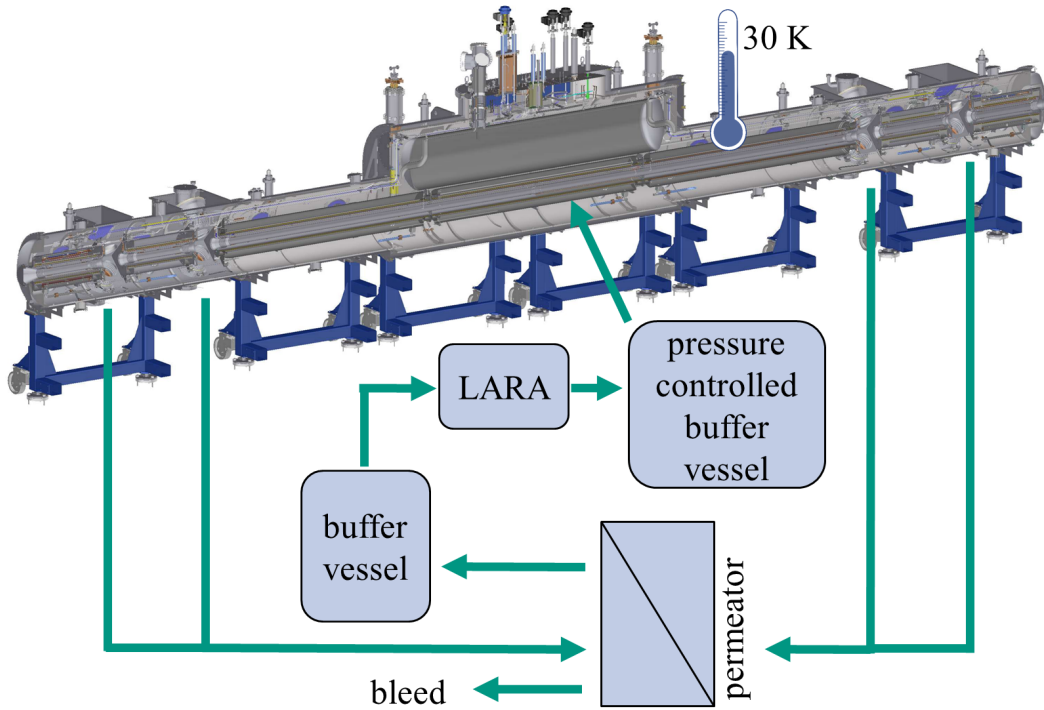


Figure 2.2.: WGTS cryostat with inner loop system. The WGTS cryostat is shown together with a simplified inner loop system. The arrows illustrate the direction of the tritium flow, beginning from the pressure controlled buffer vessel to the injection in the center of the WGTS. In the four pump ports, the tritium is pumped out and cleaned in the permeator (the non-tritium gases are bled). The extracted tritium is given back into a buffer vessel. The gas composition is monitored with the LARA system before it is injected into the source.

2.2.1. Windowless gaseous tritium source

The 26 t WGTS cryostat is 16 m long, 1.5 m wide, and up to 4 m high; a CAD drawing can be seen in figure 2.2. In the middle of the WGTS tritium gas is inserted via an injection chamber with 415 orifices [Hei19]. This allows a three dimensional injection of tritium into the 10 m long beam tube, which has a diameter of 90 mm. Together with the magnetic field of up to 3.6 T [A⁺18d] provided by three superconducting coils, this central beam tube defines the magnetic flux of

$$\Phi = 191 \text{ T cm}^2, \quad (2.4)$$

which is mapped onto the KATRIN detector. At both ends of this central beam tube, there are pump ports attached, each equipped with 4 turbo molecular pumps (TMPs). These pumps mainly define the column density distribution along the 10 m. In nominal operation a total column density of 5×10^{21} molecules m^{-2} is reached, representing a trade-off between maximizing the count rate on the one hand, and minimizing the scattering probability for the β -electrons on the other hand [KAT05]. The column density \mathcal{N} is defined as the integral of the molecular density along the

beam axis resulting in [Hei19]

$$\mathcal{N} = \int_{-5\text{m}}^{5\text{m}} n(\vec{r}, p_{\text{in}}, p_{\text{out}}, T(\vec{r})) dz, \quad (2.5)$$

with the number density n , the injection pressure p_{in} , the outlet pressure p_{out} , and the temperature $T(\vec{r})$ at spatial coordinate \vec{r} .

Subsequent to each of the two pump ports another 1 m long beam tube element is mounted. Following this one, there is another pump port equipped with 2 TMPs and again it follows a 1 m beam tube element (see figure 2.2). On the upstream side the so-called pump port 0 (PP0) with 2 additional TMPs connects the front part of WGTS and the DPS (see section 2.2.3). In total a tritium flow reduction of more than two orders of magnitude is reached according to simulations [KHD⁺18]. Additionally four superconducting coils producing a maximum magnetic field of up to 5.6 T are installed, which surround the four 1 m long beam tube elements.

There are two operation modes, the nominal tritium operation with the inner beam tube at a temperature of 30 K and the ^{83m}Kr operation mode with a temperature at 100 K avoiding freezing of krypton on the beam tube surface. The temperature of 30 K reduces the influence of the Doppler effect on the one hand, while on the other hand it avoids clustering of tritium molecules at lower temperatures [KAT05]. An inner radiation shield cooled down with 27 K helium shields the beam tube from the 4.5 K cold magnet coils. As the column density should be stable in order to achieve a stable count rate, the temperature has to be monitored precisely. For the nominal operation, neon is used for the two-phase tube connected to the outer wall of the central 10 m long beam tube. The two-phase tube is half way filled with liquid and gaseous neon, respectively. A small pressure increase of the nominal 2 bar can be directly translated into a corresponding temperature increase [Mar17]. In order to control the evaporation of neon, four 2 W heaters are installed on each cooling pipe. At one end, the two-phase tube is connected with the 27 K helium cooling which results in the condensing of neon on this side and flowing back into the phase tube [GJBG⁺08, Gro09, GBSS11, GBH⁺13]. Furthermore, 24 temperature sensors are installed at the central beam tube which are calibrated regularly before a measurement campaign starts.

The tritium injection is controlled via the inner loop system. In order to achieve a stable injection on the 0.1% level, the tritium is stored in a pressure controlled buffer vessel before it is inserted into the WGTS [KBK⁺08, Stu10, PSB15]. On the way to the WGTS, the injection capillary is thermally coupled to the two-phase cooling tube ensuring a stable inlet flow. The tritium pumped out in the WGTS pump ports is recycled by a permeator, which separates other gases. Thereby, a tritium purity of $\epsilon_{\text{T}} > 95\%$ has to be ensured with a stability of 0.1% [KAT05]. The purity is continuously monitored with the laser Raman system (LARA, see section 2.2.2.2) [SSR⁺13, SJF⁺13, SRS⁺13, Fis14]. The LARA cell is located between the two buffer vessels (see figure 2.2).

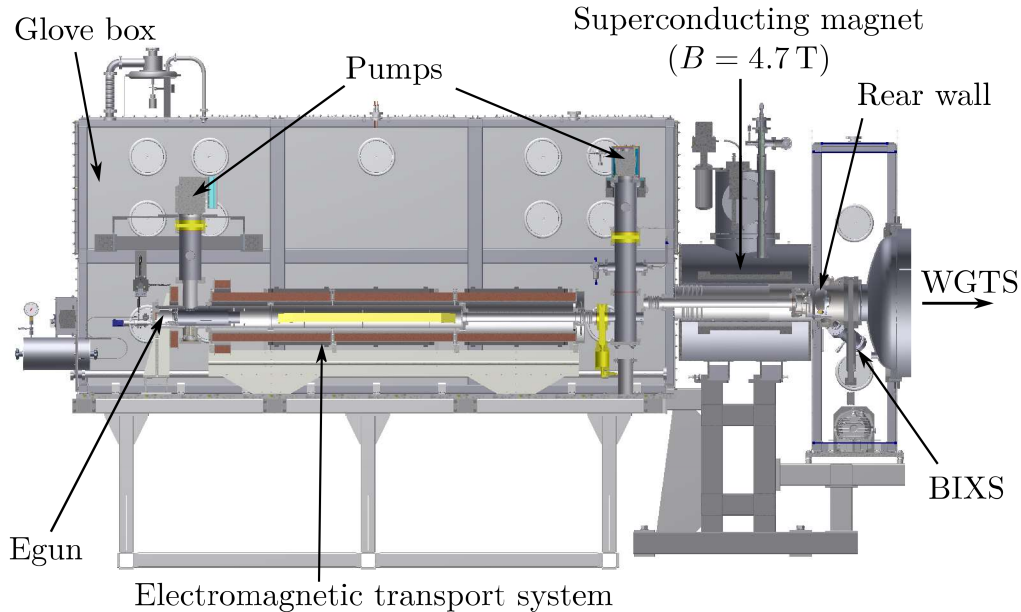


Figure 2.3.: Rear section. The different parts of the rear section are shown in the CAD drawing. From the left, the egun is contained inside a glove box, which serves as a second containment for the tritium inside. The egun electrons are guided by the electromagnetic transport system into the WGTS. The superconducting magnet is located between the glove box and the rear wall chamber containing the rear wall and the BIXS system. The drawing is taken from [SM19].

2.2.2. Monitoring devices

2.2.2.1. Rear section

Located at the upstream end of the KATRIN beam line, the rear section (see figure 2.3) provides several monitor and calibration tools. The beam line is terminated with the rear wall, which is a gold plated stainless steel disc with a diameter of 145 mm. It can be set to voltages up to 500 V. Dedicated plasma simulations indicated that the WGTS plasma potential can be controlled by the rear wall potential [KAT05, Röl15, Kuc16]. As the β -electrons decay isotropically, approximately half of them will be guided to the rear wall, where they produce X-rays via interaction with the gold surface. The intensity of these X-rays is measured with BIXS detectors enabling to monitor the source activity on the per-mill level [Röl15]. In order to focus the beam towards the rear wall, a superconducting magnet (maximal magnetic field 4.7 T) is located between the electron gun setup and the rear wall chamber.

For measurements of the column density and the energy loss function, a dedicated electron gun (egun) is installed on the rear end of the rear section [HHW⁺17]. The egun provides a narrow beam of photoelectrons with energies of up to 30 keV at count rates of more than 10^4 . The electron beam is transmitted into the rear section through a 5 mm hole in the center of the rear wall and can be shot through the complete KATRIN beamline. It has a small angular distribution with pitch angles less than 4° and a low energy spread of 0.2 eV [Bab14, Hei15]. The first commissioning

of the egun has been performed in September 2018.

2.2.2.2. Laser Raman system

Since tritium is decaying, the gas composition inside the loop system changes over time. As different tritium isotopologues in the same amount of gas lead to a different source activity (e.g. two tritium atoms in T_2 , one in DT), the abundance has to be monitored. Furthermore, different mother molecules have distinct probabilities for decaying into the different possible daughter molecule ions (${}^3\text{HeT}^+$, ${}^3\text{HeD}^+$, and ${}^3\text{HeH}^+$). Therefore, monitoring of the gas composition on the level of 10^{-3} is important for ensuring stable measurement conditions in the WGTS [BBB⁺12]. In order to fulfill these requirements, the LARA system has been designed, installed and successfully commissioned [FSS⁺11, SSR⁺13, Fis14].

In an optical cell, a gas probe is analyzed by a laser with a wavelength of 532 nm. The photons will scatter off the gas molecules and the resulting spectroscopy spectrum is recorded. After a calibration [SSR⁺13, Zel17], the Raman spectrum can be analyzed by using the different rotational and vibrational excitations of the corresponding hydrogen molecules.

2.2.2.3. Forward beam monitor

The forward beam monitor (FBM) measures the source activity with two Si-PIN diodes in the cryogenic pumping section. As it is located in front of the spectrometer section, the FBM is exposed to the complete β -spectrum. Via two stepper motors the FBM can be moved in horizontal and vertical direction. Its nominal monitoring position is at the outer edge of the magnetic flux tube but it can also be moved out of the flux tube completely. On the detector board a Pt1000 temperature sensor and a Hall sensor are mounted. Results of previous KATRIN measurement campaigns can be found in [A⁺18c].

2.2.3. Differential pumping section

The differential pumping section (DPS) is the first part of the KATRIN transport sections. Its setup is shown in figure 2.4. The total length of the beam tube is 6.5 m consisting of five individual beam tube elements where each is tilted by 20° compared to its neighboring elements. These five elements are enclosed by the so-called pump port 0 (PP0) on the upstream and the pump port 5 (PP5) on the downstream end [Jan15, Hac17]. There are five superconducting magnets, which can provide a magnetic field up to 5.6 T and guide the β -electrons through the beamline [A⁺18d] adiabatically.

The DPS has three main purposes. The first one is to guide the β -electrons by the magnetic field lines adiabatically through the beamline. Secondly, the neutral tritium flux has to be reduced by at least five orders of magnitude in downstream direction in order to prevent β -induced events in the main spectrometer (see section 2.3.7). Thirdly, the tritium ions created in WGTS shall not pass towards the spectrometer section and therefore have to be blocked and removed. In order to fulfill the first task, there are five superconducting magnets in place, which can provide a magnetic field of up to 5.5 T [A⁺18d]. For reducing the neutral tritium

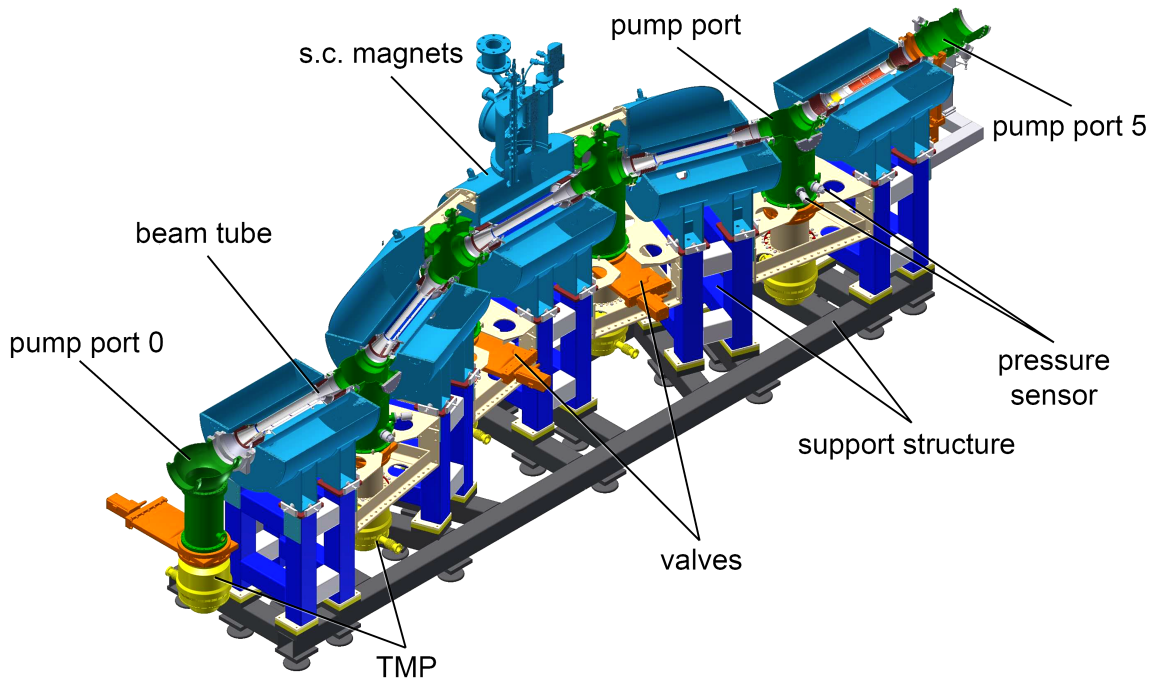


Figure 2.4.: DPS CAD drawing. The DPS CAD drawing is shown with a 3/4 cut along the horizontal plane. The TMPs (yellow) are attached to the pump ports (green), which are connected to the beam tube (silver). Five superconducting solenoids (blue) surround the beam tube. The figure is adapted from [FRS⁺19].

flow six TMPs are installed, each providing a pumping speed of $2400 \ell s^{-1}$ for tritium [Mal07]. The TMPs are connected to the loop system circulating the tritium back into the buffer vessel after the tritium isotopologues have been filtered out in the permeator (see figure 2.2). A more detail description of the vacuum system is discussed in section 3.1. For the ion blocking and removing two different systems are installed inside of the DPS beam tube elements:

- Four dipole electrodes use the $\vec{E} \times \vec{B}$ drift to deflect the incoming ions towards a series of lobes attached to one of the dipole's half shells and thereby remove them out of the system.
- Two ring electrodes in the fifth beam tube element and in the adjacent PP5 are set on a positive blocking potential.
- In the last beam tube element, a Fourier transform ion cyclotron resonance (FT-ICR) device is installed [UDRL⁺09]. In principle, it could be used for measuring the frequency spectrum of the different ion species originating from the WGTS. However, due to technical issues it can and will not be operated for performing meaningful measurements.

During the First Light as well as the First Tritium campaign, the ion blocking devices have been tested successfully [Hac17, A⁺18c, Kle19].

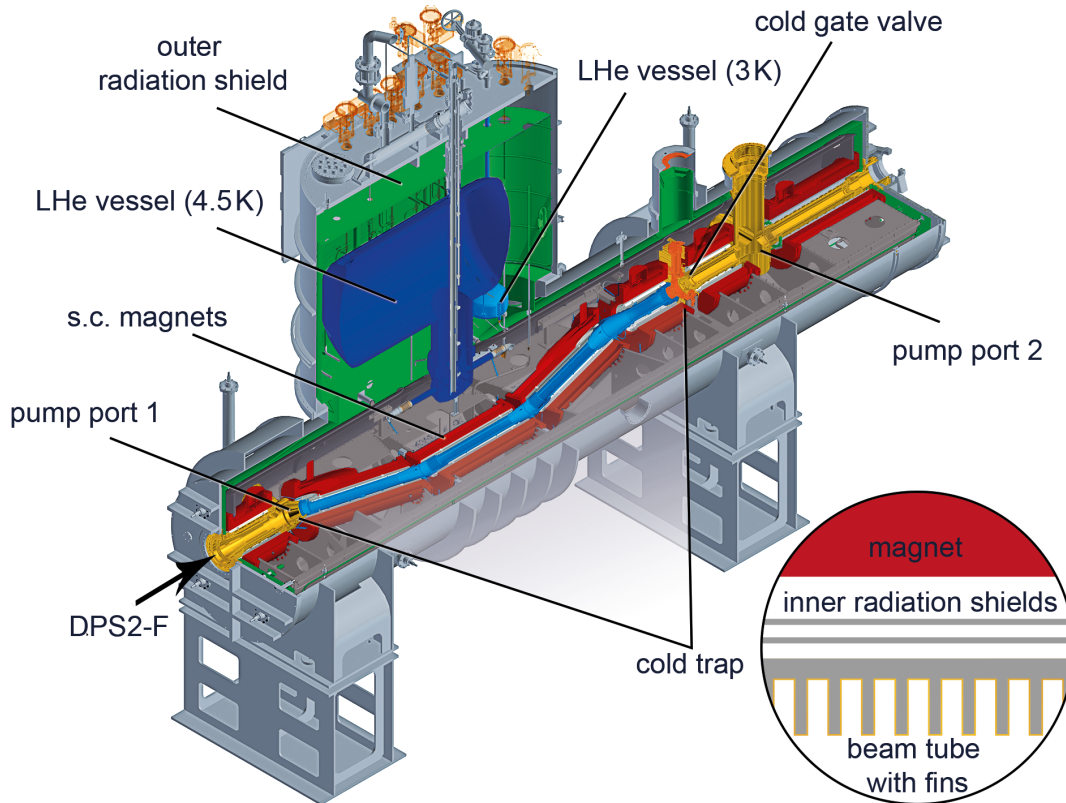


Figure 2.5.: CPS cryostat. The CPS cryostat is shown in a CAD drawing (3/4 cut). Seven superconducting solenoids (red) are installed around the gold-plated beam tube. For cooling the magnets and the cold trap (blue), a LHe vessel (4.5 K) provides a reservoir of 4.5 K cold helium. The cold trap is further cooled down to 3 K, while the rest of the beam tube is at 77 K using the nitrogen cooling. The cold gate valve (operated at 4.5 K) separates the end of the cold trap from PP2 and acts as a safety valve [FRS⁺19].

2.2.4. Cryogenic pumping section

The second part of the transport section is the cryogenic pumping section (CPS, see figure 2.3). It consists of a 6.5 m long and 4 m high cryostat in which the beam tube is embedded [Jan15, FRS⁺19]. Besides guiding the β -electrons magnetically towards the spectrometers, the CPS is designed for reducing the incoming tritium flow by at least another seven orders of magnitude. The key components of the CPS are seven beam tube elements, two pump ports (PP1 and PP2), three cooling vessels, and seven superconducting magnets (see figure 2.5). Three of the beam tube elements (1,6, and 7) are aligned in a straight way and are cooled to liquid nitrogen temperature. The beam tube elements 2 to 5 are tilted by 15° compared to their direct neighbors and are cooled down to liquid helium temperature of 3 K. The tilting is implemented in order to increase the probability of particles hitting the inner beam tube wall. After hitting the wall, the molecules eventually stick to the surface because of cryosorption. This is why this central part of the CPS beam tube is referred to as the cold trap. The sticking surface is provided by an argon frost layer prepared on top of the gold-plated inner beam tube wall. For increasing the effective pumping surface there are fins on the inside of beam tube elements 2 to 5 (for more details see section 3.2). After 60 days of standard KATRIN operation

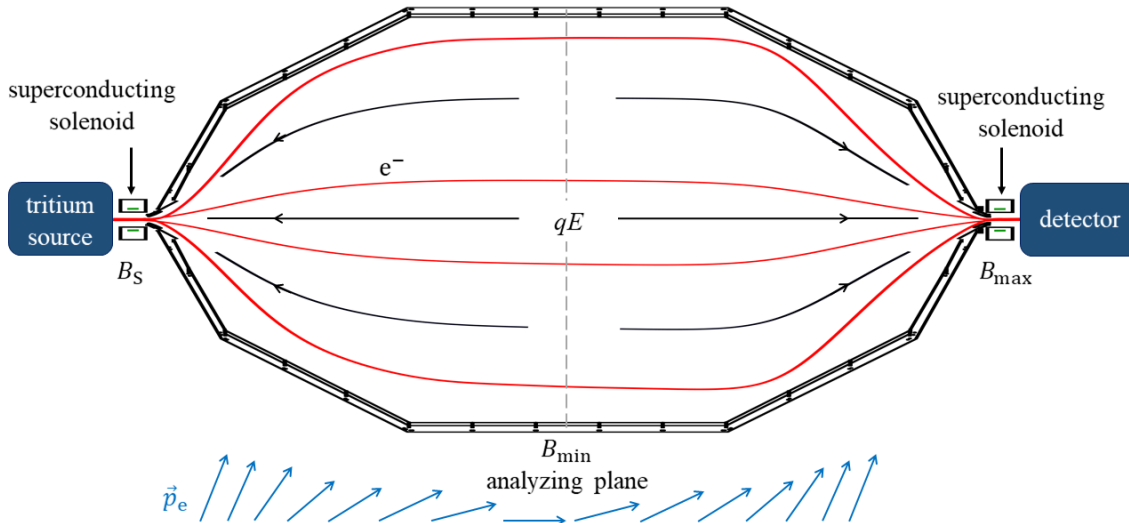


Figure 2.6.: MAC-E filter method. The β -electrons produced in the tritium source enter the spectrometer. If the electron’s energy is larger than qE defined by the set potential, they will reach the detector. In front of and behind the spectrometer there are superconducting magnets. Towards the center of the MAC-E filter the magnetic field strength continuously decreases while the electrons’ momenta are collimated. Below the MAC-E filter the corresponding electron momenta are shown. At the analyzing plane the momentum vector has only a component parallel to the electric field lines. The drawing is based on [Hac17].

equivalent to an accumulated activity of 1 Ci, the argon frost layer is regenerated by purging with helium. During this process the cold gate valve is closed. A more detailed description of these processes is given in section 3.2.5.

For the adiabatic β -electron transport, seven superconducting solenoids each provide a magnetic field of up to 5.6 T.

At PP2, the forward beam monitor (FBM) can be inserted horizontally (see section 2.2.2.3). On the FBM board, there are two PIN diodes mounted for monitoring the β -activity at the outer edge of the sensitive magnetic flux tube. Furthermore, at PP2 a quench condensed krypton source can be moved inside of the beam tube for calibration purposes [A⁺18b].

2.2.5. Spectrometer section

KATRIN uses the magnetic adiabatic collimation MAC-E filter principle to measure the β -electrons with a high sensitivity and therefore determine the effective neutrino mass. The method is based on previous neutrino experiments in Mainz and Troitsk [BPT80, LS85a, KBB⁺05, ABB⁺11]. Figure 2.6 shows the MAC-E filter principle. In the following the most important MAC-E filter characteristics are described.

- **Adiabatic guiding of the electrons:** The two superconducting magnets define the trajectories, on which the electrons travel through the spectrometer.

Due to the isotropic source, the β -particles do not only carry a momentum component parallel to the magnetic field direction $p_{\parallel} = |\vec{p}| \cdot \cos\theta$ but also a perpendicular one $p_{\perp} = |\vec{p}| \cdot \sin\theta$. The polar angle θ is defined as the angle between the magnetic field line and the decay direction. While the perpendicular component results in a cyclotron motion, the parallel one is responsible for the guidance along the magnetic field lines. The total kinetic energy is given by

$$E_{\text{kin}} = \frac{|\vec{p}|^2}{2m} = E_{\parallel} + E_{\perp}. \quad (2.6)$$

The adiabatic transport condition is true if the product of the magnetic moment μ and the Lorentz-factor γ is constant [Jac99]. Due to the β -electron's maximum energy of 18.6 keV, it is $\gamma_{\text{max}} = 1.04$. The deviation from 1 can be neglected. The magnetic moment is defined by

$$\mu = \frac{E_{\perp}}{B} = \text{const.} \quad (2.7)$$

In order to minimize E_{\perp} , the magnetic field has to be minimal, too. This is the reason for designing the spectrometer in a way that the minimum magnetic field strength is reached at the analyzing plane (see figure 2.6) where the electrostatic potential reaches a maximum. At the same time the perpendicular energy is transformed into the parallel energy component due to energy conservation. However, the magnetic field gradient has to be small enough to allow the adiabatic conservation. In reality any MAC-E filter has a finite energy resolution meaning that the minimum magnetic field is not equal to zero. Consequently, there is a remaining perpendicular energy component, which has to be accounted for in the measured electron rate of the detector.

- **Electrostatic filter:** By applying a negative high potential to the spectrometer, it acts as a high-pass filter allowing only electrons with a longitudinal energy $E_{\parallel} > |qU_0|$ to pass the potential barrier. The electric field lines are parallel to the magnetic ones in the analyzing plane. As previously mentioned, the perpendicular energy component should be close to zero in order to achieve the highest possible energy resolution. This method only allows to measure an integral spectrum, therefore the spectrometer high voltage has to be changed to be able to scan the β -spectrum endpoint.
- **Conservation of the magnetic flux:** The KATRIN magnetic flux is defined at the WGTS by the source magnetic field and the beam tube diameter (see section 2.2.1). It is given by

$$\Phi = \int_A \vec{B} \cdot d\vec{A} = \text{const.} \quad (2.8)$$

As the magnetic field is varying along the KATRIN beam line, the flux tube diameter changes respectively. With the minimum magnetic field set in the analyzing plane, the required maximum diameter can be determined as

$$d_{\text{max}} = d_{\text{source}} \cdot \sqrt{\frac{B_{\text{source}}}{B_{\text{min}}}}. \quad (2.9)$$

In KATRIN the minimum magnetic field is 0.3 mT, which defines the maximum diameter to be $d_{\text{max}} = 10$ m.

- **Energy resolution:** For the energy resolution ΔE , the minimum magnetic field B_{\min} in the analyzing plane, and the maximum magnetic field B_{\max} behind the main spectrometer have to be considered. By calculating the ratio, the resolution for a specific energy E is given by

$$\Delta E = \frac{B_{\min}}{B_{\max}} \cdot E . \quad (2.10)$$

By neglecting the relativistic effects, the KATRIN energy resolution can be determined for β -electrons close to the tritium endpoint of 18.6 keV

$$\Delta E = \frac{0.3 \text{ mT}}{6 \text{ T}} \cdot 18.6 \text{ keV} = 0.93 \text{ eV} . \quad (2.11)$$

- **Magnetic mirror effect:** For adiabatic motion the relation between the magnetic field B and the electron's pitch angle θ relative to the beam axis is given by

$$\frac{B_1}{B_2} = \frac{\sin^2 \theta_1}{\sin^2 \theta_2} , \quad (2.12)$$

for arbitrary points 1 and 2. Therefore only β -electrons, which started with a small enough angle will reach the detector, the others will be reflected. With the values for the source magnetic field ($B_{\text{source}} = 3.6 \text{ T}$) and the maximum magnetic field ($B_{\max} = 6 \text{ T}$), the maximal acceptance angle θ_{\max} can be derived by setting $\theta_2 = 90^\circ$:

$$\theta_{\max} = \arcsin \left(\sqrt{\frac{B_{\text{source}}}{B_{\max}}} \right) = 51.7^\circ . \quad (2.13)$$

The maximum value should not be larger than this particular value because otherwise the scattering probability increases as well as the synchrotron radiation.

- **Transmission function:** To be able to calculate the expected count rate at the detector, the transmission function $T(E, qU_0)$ for an incoming electron has to be included for a given potential qU_0

$$\frac{dN(qU_0)}{dt} \propto \int_{qU_0}^{E_0} \frac{d^2 N}{dt dE} (E_0, m_{\nu_e}^2) \cdot T(E, qU_0) \cdot dE , \quad (2.14)$$

with $\frac{d^2 N}{dt dE} (E_0, m_{\nu_e}^2)$, and the parameters defined in equation (1.46). For the transmission probability $T(E, qU_0)$ three different cases have to be distinguished [KAT05, KBD⁺18]:

$$T(E, qU_0) = \begin{cases} 0 & \text{if } E < |qU_0| \\ \frac{1 - \sqrt{1 - \frac{E - qU_0}{E} \cdot \frac{B_S}{B_{\min}}}}{1 - \sqrt{1 - \frac{B_S}{B_{\min}}}} & \text{if } |qU_0| \leq E \leq |qU_0| + \Delta E \\ 1 & \text{if } E > |qU_0| + \Delta E . \end{cases} \quad (2.15)$$

These equations are valid for an isotropic source.

- **Response function:** On their way from the decay in the source, several effects have to be included, which can cause energy loss of the β -electrons. These effects are summarized in the KATRIN response function $R(E, qU_0)$, which is measured with the rear section electron gun. Additionally to the transmission function $T(E, qU_0)$ (see equation (2.15)), the energy loss function $f(\epsilon)$ is considered in $R(E, qU_0)$ [KBD⁺18]

$$R(E, qU_0) = \int_{\epsilon}^{qU_0} \int_{\theta=0}^{\theta_{\max}} T(E - \epsilon, \theta, qU_0) \sin \theta \sum_s P_s(\theta) f_s(\epsilon) d\theta d\epsilon. \quad (2.16)$$

$P_s(\theta)$ is the probability for s scattering processes with the angle θ .

2.2.5.1. Pre-spectrometer

The pre-spectrometer is surrounded by two superconducting magnetic solenoids, which can be operated at a magnetic field up to 4.5 T. Its main purpose is to reduce the incoming β -electron flux by seven orders of magnitude by applying a negative potential of 18.3 kV. An energy resolution of $\Delta E = 70$ eV is reached at an energy of 18.6 keV. Additionally, a picoammeter connected to an inner electrode of the pre-spectrometer allows an in-situ measurement of a residual ion flux into the spectrometer section [Kle19]. For ensuring ultra high vacuum conditions, TMPs and Non Evaporable Getter (NEG) pumps are used in the 3.4 m long vessel.

In order to reduce the background caused by a Penning trap, Penning wipers are installed in between both spectrometers, which were successfully tested [Pra11, PRG⁺12]. The results of further commissioning measurements can be found in [Frä10, FBD⁺11, MBB⁺12, WDF⁺13, FGV⁺14].

2.2.5.2. Main spectrometer

The main spectrometer has a diameter of 10 m and a length of 23 m resulting in a total volume of 1240 m³. Inside the vessel a pressure in the order of 10⁻¹¹ mbar is reached using TMPs and NEG pumps [ABB⁺16]. In order to reduce the outgassing rate from the inner surface, the main spectrometer was heated up to 200 °C before the tritium measurement campaign started. As previously derived, the achieved energy resolution is 0.93 eV for the tritium endpoint energy.

Inside the spectrometer, a double layer of electrodes are installed, which allow to set the desired electric potential. Additionally they actively suppress the background rate (more details in section 2.3). 15 air coils installed along the spectrometer main axis allow to adjust the magnetic field gradient. With this set-up a minimal magnetic field of 0.3 mT can be reached. For the compensation of the earth magnetic field, there are 26 current loops, which are installed vertically and horizontally. Two mobile units are used to monitor the magnetic field in the analyzing plane by moving around the inner side of two air coils. Furthermore, 36 stationary Hall sensors are installed along the main spectrometer vessel [OSL⁺12, Rei13, Erh16].

The results of main spectrometer characterization can be found in [Gör14, Lei14, Sch14, Gro15, Har15, Kra16, Erh16, Beh16, Hil16, BRB⁺17, Fra17, Tro19].

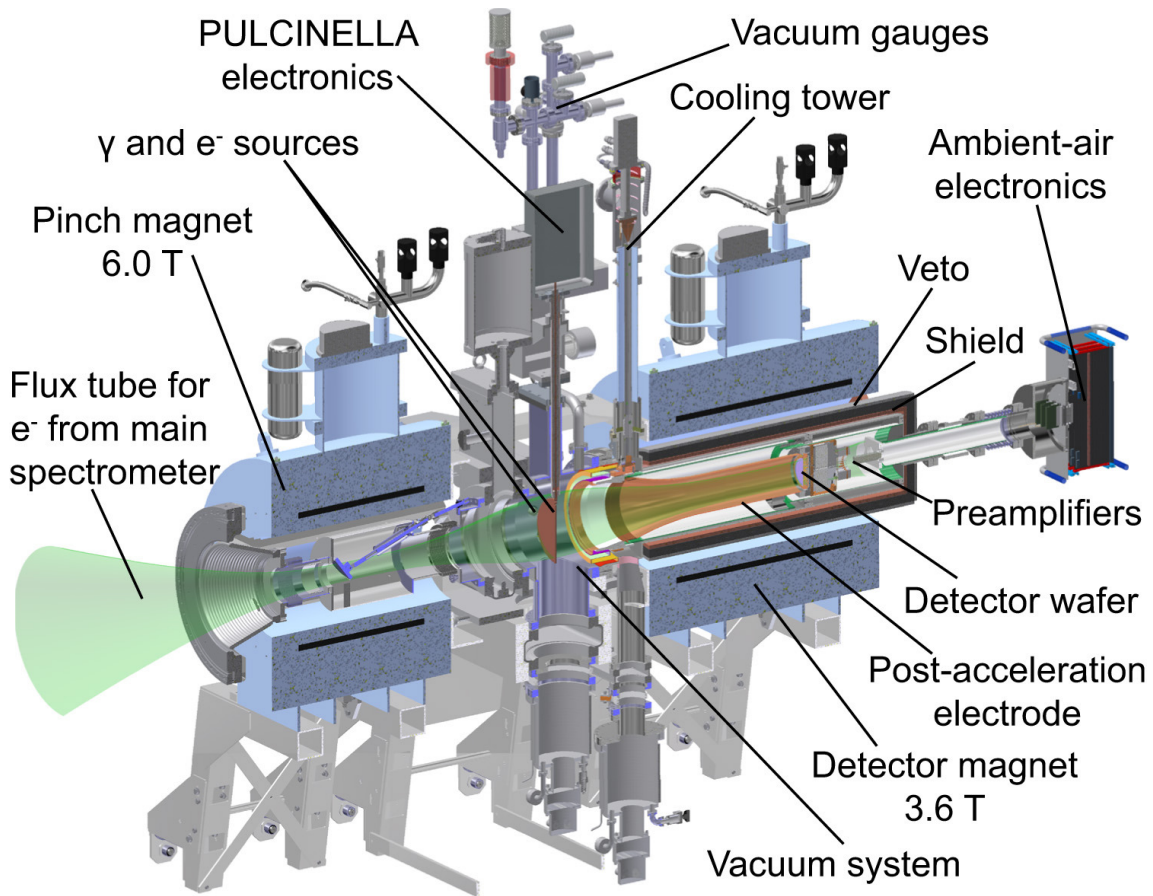


Figure 2.7.: KATRIN detector system set-up. The different components of the detector system are labeled in the CAD drawing in a $1/2$ cut. The main parts are described in the text, a more detailed description can be found in reference [ABB⁺15].

2.2.6. Detector

At the end of the KATRIN beam line, the detector system is installed. The electrons transmitted through the main spectrometer are counted by silicon PIN diodes. The detector wafer has a diameter of 90 mm and is subdivided into 148 pixels of equal area. A CAD drawing of the detector system is shown in figure 2.7; it contains two superconducting magnets, the pinch magnet with the largest magnetic field of the KATRIN beam line, and the detector magnet, which surrounds the detector wafer. In order to reduce the background rate, a post-acceleration electrode is installed and is operated at 10 kV. This results in an additional acceleration of the β -electrons to an energy region with a smaller intrinsic noise. As the KATRIN energy resolution is defined by equation (2.11), therefore a detector energy resolution of approximately 2 keV per pixel is sufficient. For the calibration of the individual pixels a γ or an e^- source can be inserted between both magnets.

In a separate mode, the Precision Ultra-Low Current Integrating Normalization Electrometer for Low-Level Analysis (PULCINELLA), which consists of a Faraday cup is measuring the electron flux current [ABB⁺15].

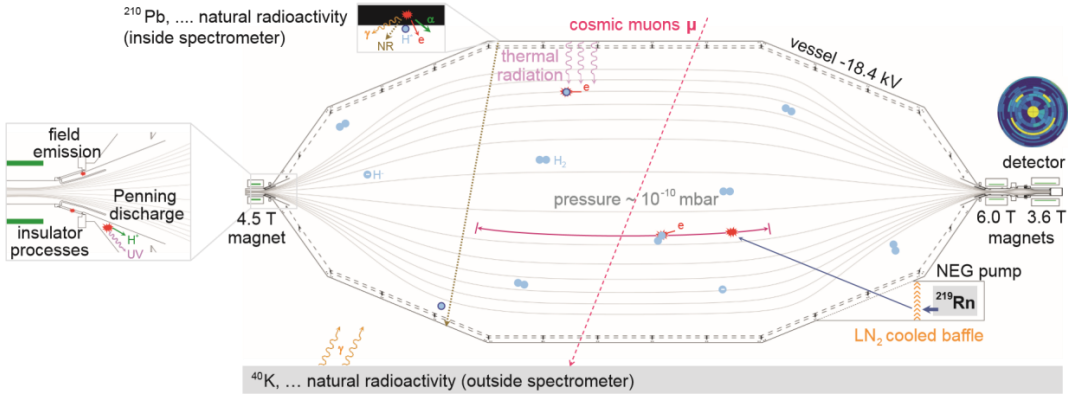


Figure 2.8.: Background processes of the spectrometer and detector section.

There are several processes which could induce a background rate at the detector. The origin of these processes are discussed in the text. The figure is taken from [Fra17].

2.2.7. Monitor spectrometer

The task of the monitor spectrometer is to monitor the high voltage fluctuations of the main spectrometer on the ppm level. It mainly consists of components of the spectrometer used in the Mainz neutrino mass experiment, and has a length of 4 m and a diameter of 1 m. The two superconducting solenoids can reach a magnetic field of up to 6 T [EBB⁺14]. The electrodes in the monitor spectrometer are coupled galvanically with the high voltage set on the main spectrometer while the outer wall is grounded. With the K32 conversion electrons from a ^{83m}Kr source, a stable energy of 17.83 keV can be observed [Zbo11]. In order to compensate the energy difference to the tritium endpoint energy, the krypton source is set on a potential at the beginning of the spectrometer. At the other end, a silicon PIN diode serves as a detector for measuring the conversion electron rate. The results of several commissioning measurements can be found in [Zbo11, SBD⁺13, ZBB⁺13, EBB⁺14, Sle15].

2.3. Background processes

As the KATRIN background rate is a key parameter for the sensitivity, the rate has to be as low as possible. Measurements [Har15, Tro19] have shown that a background rate of 10 mcps targeted in the KATRIN design report [KAT05] is exceeded by a factor of approximately 40. This leads to a slightly worse sensitivity of the neutrino mass compared to the designed 200 meV. In order to achieve the designed sensitivity and therefore reducing the background rate, the existing background processes have to be fully understood to apply possible countermeasures. Since the previous measurements were analyzed without tritium in the KATRIN beamline, the background rate could change for nominal tritium operation.

In the following, the background processes (see figure 2.8), which have to be taken into account for the background rate, are described.

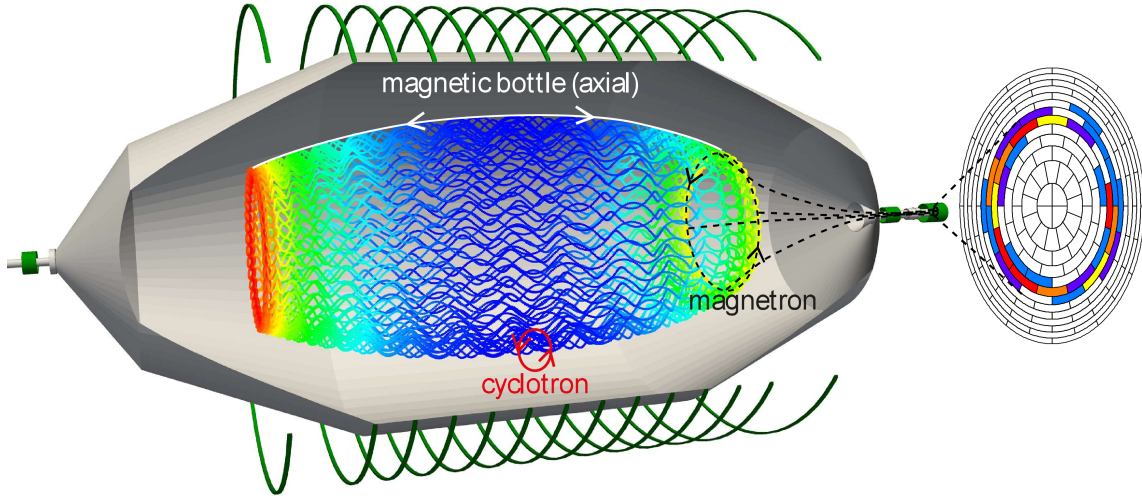


Figure 2.9.: Magnetically stored particle inside main spectrometer. A charged particle inside the main spectrometer is trapped between the two high magnetic fields at both ends of the spectrometer. This magnetic bottle defines the area where a particle can be trapped. During the storage, the particle can move along different axes illustrated by the arrows and create secondary electrons via scattering with residual gas. The ring-like event rate seen by the detector is typical for stored particles that break the storage condition of equation (2.17). This figure is extracted from [Har15].

2.3.1. Magnetically stored particles in the spectrometer

An electron is trapped, if its starting polar angle θ is larger than [Gro15]

$$\theta > \theta_{\max} = \arcsin \left(\sqrt{\frac{qU(\vec{x}_s)}{E_{\text{kin}}(\vec{x}_s)} \cdot \frac{B(\vec{x}_s)}{B_{\max}}} \right). \quad (2.17)$$

Here, $U(\vec{x}_s)$ corresponds to the electric potential at a given starting point \vec{x}_s of the electron, $E_{\text{kin}}(\vec{x}_s)$ is the electron's kinetic energy, $B(\vec{x}_s)$ the magnetic field at \vec{x}_s , and B_{\max} the maximum magnetic field defined by the Pinch magnet. Therefore a higher magnetic field B_{\max} and initial energy E_{kin} of the stored particle decrease θ_{\max} and increase the probability for electrons to be stored.

For the particle motion inside the magnetic bottle, three components have to be considered, which are also illustrated in figure 2.9:

- The particle travels along the magnetic field line and therefore performs a longitudinal motion. This axial motion can be executed in both directions.
- The cyclotron force causes a fast gyration around its center motion.
- The magnetron drift leading the stored particle to oscillate around the beam-line axis.

Primary particles, which are trapped inside the magnetic bottle can stay there for hours [Har15]. Eventually, the primary particles scatter with residual gas and cool down and finally leave the magnetic bottle if the condition in equation (2.17) is not fulfilled anymore. During these scattering processes, secondary electrons are

produced alongside the axis of motion. These secondary electrons can be guided to the detector wafer due to their lower energy (compare equation (2.17)) and produce ring-wise patterns as they share the magnetron radius of the primary particle [Sch14, Har15]. Depending on the illuminated rings, the motion of the primary particle can be determined. The number of secondary electrons can be used for the analysis of the initial energy of the primary particle identifying the background source. However, the possible energy loss of secondary particles (determined by dedicated simulations) has to be included for example due to synchrotron radiation, or a loss of secondary electrons, which leave the magnetic bottle and hit the spectrometer surface [Gro15, Har15].

2.3.2. Penning traps

Between the spectrometers Penning traps can be induced by the strong magnetic and electric fields. If they are not prevented, they produce a background rate larger than 1 kcps [Frä10].

In order to produce a Penning trap, a charged particle has to be trapped in between two electric potentials for example between two cathodes. Therefore, a low energetic electron has to be emitted off a cathode's surface. By following the magnetic field lines, it is accelerated by the potential of the other cathode. During the traveling time, the electron loses energy either by scattering or cyclotron radiation so that they are not able to reach the other cathode. This process leads to an oscillation between both cathodes. After a certain time (depending on the pressure), the electron scatters with residual gas molecules and therefore produces secondary electrons and ions. The maximal number of secondary electrons, which can be produced within a Penning trap is given by [Frä10]

$$N_{\max} = 2^{eU_{\text{trap}}/E_{\text{ion}}} - 1, \quad (2.18)$$

with the electric potential difference inside the Penning trap U_{trap} , and the ionization energy of the residual gas molecules E_{ion} . The ion can create further secondary electrons by hitting the cathode which are trapped with the probability p . If for the product of the ions N_{ion} produced by primary electrons and p applies

$$N_{\text{ion}} \cdot p \geq 1 \quad (2.19)$$

a self-sustained Penning discharge starts [Frä10]. This effect leads to a negative space charge as the ions are not trapped, decreasing the initial U_{trap} [Kna62]. Ultimately an equilibrium state is reached, which produces a stable Penning discharge.

In order to prevent such Penning discharges, dedicated Penning wipers are installed, which decrease the Penning trap induced background rate by several orders of magnitude. More information can be found in [Frä10, FGV⁺14].

2.3.3. Muon-induced background

In contrast to other low background experiments searching for dark matter particles or $0\nu\beta\beta$ -decays, the KATRIN experiment is not located underground. Therefore, muons with GeV energies [THH⁺18] arising from cosmic showers have to be taken into account as they can produce electrons via ionization. Approximately every

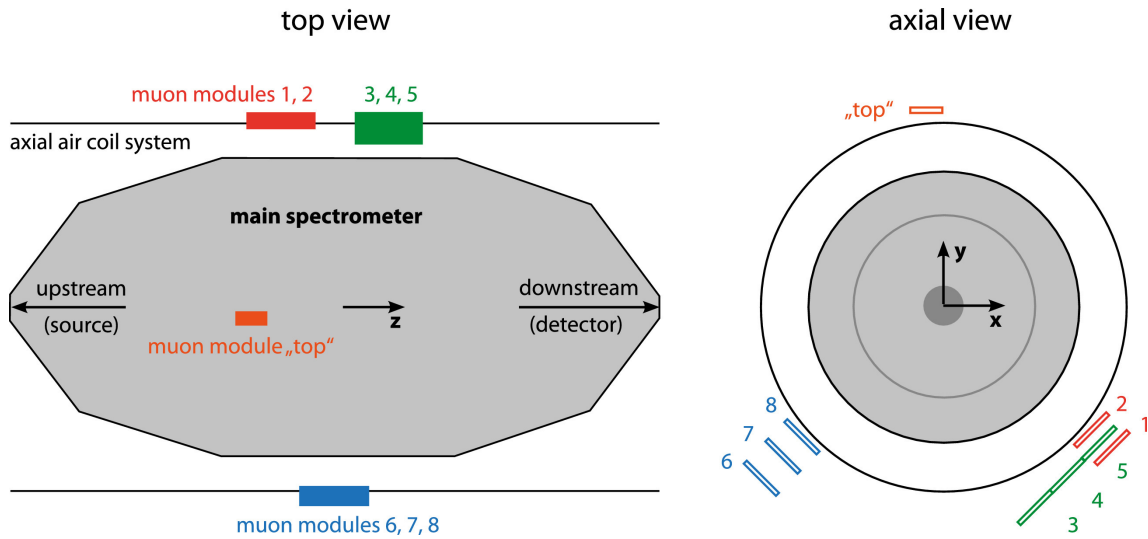


Figure 2.10.: Muon-veto system: The location of the installed muon-veto system is shown. On the left side the main spectrometer is drawn from the top, on the right side an axial view is given. The figure is taken from [AAB⁺19].

17th muon which passes through the main spectrometer creates such secondary electrons [AAB⁺19]. These electrons can produce further secondary electrons via scattering and cascade processes, which can have energies below 30 eV and therefore can be accelerated by the electromagnetic field inside the spectrometer to the detector [AAB⁺19]. In such a case, the muon-induced events cannot be distinguished from a β -decay signal electron. In order to prevent such events, there are counteractions. The vessel and inner wire electrodes are on a different potential (200 V difference) so that electrons arising from the walls are reflected and cannot enter the spectrometer volume. Furthermore, the setting of the magnetic field inside the main spectrometer only allows electrons with a small polar angle (see equation (2.17)) to enter the inner volume. Otherwise, the electrons are also rejected. In addition, a muon veto system is installed (see figure 2.10), with which it is possible to find coincident events from the veto system and the detector.

Since the background rate evolving from the muon induced events contributes to less than 16.6% (90% C.L.) to the overall measured background rate, the muon veto system is not used for the neutrino mass measurements due to the large amount of data, which has to be stored when it is active [AAB⁺19]. If there will be a significant improvement in the background rate with a new reduction system, the muon system can be activated at any time.

2.3.4. Natural radioactivity

As the KATRIN beamline is not located underground, there are several possibilities for external radiation, for example ^{40}K in the spectrometer building. The γ -flux for $E_\gamma > 100\text{ keV}$ was measured to be $1\text{ cm}^{-2}\text{ s}^{-1}$ inside the building [Fra17]. With a 53 MBq ^{60}Co gamma source, which was placed 1 m away from the main spectrometer, the influence on the background rate was investigated. The results showed that a maximum of

$$\Gamma_\gamma < 5.6\text{ mcps (90\%C.L.)} \quad (2.20)$$

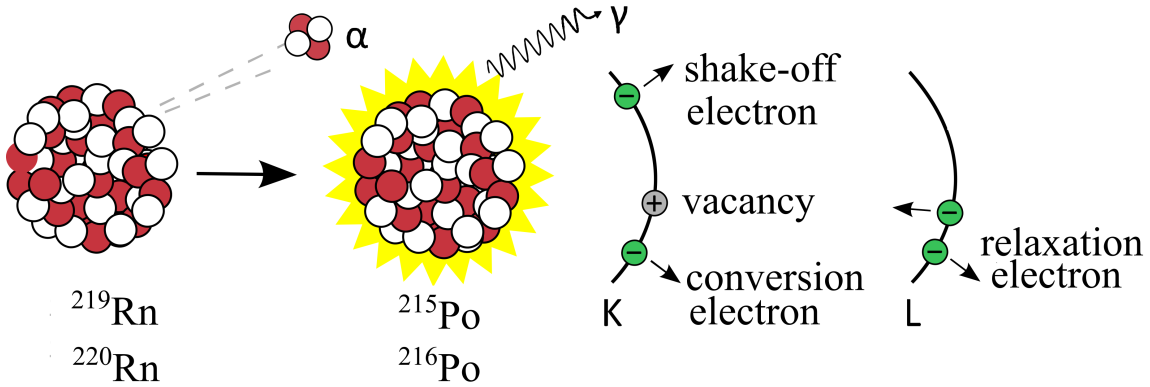


Figure 2.11.: Electron emission from radon decay. The radon atom decays via an α -decay into an excited polonium state. Afterwards, electrons can be released by different methods. The individual processes are described in the text. This figure is adapted from [Har15].

is induced by external gamma radiation [A⁺19]. In comparison with the current background rate of 400 mcps, this component can be neglected.

2.3.5. Radon induced background

One of the major contributors to the KATRIN background are radon decays, which mainly originate from the NEG pumps and the stainless steel surface [FBD⁺11, WDF⁺13, Har15]. In particular the isotopes ^{219}Ra and ^{220}Ra are relevant since they have a short half-life of 3.96 s and 55.6 s [ABBW03]. Compared to the average pumping time of the main spectrometer for radon of approximately 300 s [WDF⁺13], the radon can decay in the main spectrometer volume before it is pumped out. The radon decays via an α -decay to polonium, which is in an excited state. In the next step, the polonium can produce electrons via several effects with different electron energies.

The largest energy in the order of 100 keV comes from conversion electrons of $^{215}\text{Po}^*$, which cool down the excited state back to its ground state. Energies of up to 10 keV are achieved by either shake-off processes or atomic relaxation. For the shake-off process, the emitted α -particle interacts with an electron of the polonium atom. The electron either gets emitted or is lifted in a higher shell depending on the transferred energy by the interaction. The atomic relaxation describes the occupation by electrons from higher shells due to a vacancy caused by the emission of another electron. The released energy (inner electrons have a larger binding energy) can cause another electron to be emitted by the Auger effect. As the number of vacancies increases during this process, a cascade of emitted electrons is produced. Alternatively radiation can be emitted, which transfers the vacancies into a higher shell [Har15].

The trapped electrons can have energies up to 100 keV in the magnetic flux tube [Fra17]. Via ionization with the residual gas, a stored electron can produce hundreds of secondary electrons depending on the pressure inside the spectrometer and the initial energy. Afterwards, those secondary electrons leave the spectrometer to the detector, where they produce a background signal.

The described dependence on the pressure is used to analyze the radon background rate. By manually increasing the main spectrometer pressure, the possibility for an ionization process becomes higher. Therefore, the energy loss of the stored electrons happens faster and with the information on time difference between two ionization processes, the analysis can search for cluster events (many events in a small time interval) [Har15].

As a countermeasure, the baffle surfaces are cooled with liquid nitrogen. With this method, the radon which originates from the NEG pumps is adsorbed on the cold surface before it decays. The efficiency of the cold baffles has been measured in [Har15]. The result showed that the background rate is decreased by approximately 0.5 cps with an efficiency of 97%, when the baffles are cooled down [Fra17].

2.3.6. Rydberg hypothesis

After the suppression of the previously described background processes, there is still a rate in the order of 400 mcps left [Har15, Tro19]. Several measurements were performed, which investigated the dependencies of this background component and revealed the following properties [Har15, Tro19]:

- The rate is uniformly distributed in the spectrometer's volume.
- The inner electrode potential influences the rate. For higher potentials, the rate gets smaller.
- The pressure only slightly influences the remaining background rate.

At the moment, the most plausible hypothesis is that this major background component is induced by Rydberg atoms, which are highly excited atoms with a high principal quantum number n (typical in the range of 100) [Tro19, Hin18]. In a classical picture, the highly excited electron's radii r_n are obtained by the Bohr model and Newton's second law,

$$r_n \propto \frac{n^2}{Z}, \quad (2.21)$$

together with a binding energy of

$$E_n = -\frac{13.6 \text{ eV} \cdot Z^2}{n^2}, \quad (2.22)$$

with the nucleus charge number Z . In case of a hydrogen atom ($Z = 1$), the corresponding Rydberg atom has therefore a larger radius and a larger binding energy compared to the ground state. The lifetime is proportional to

$$\tau \propto n^{4.5} \quad (2.23)$$

and is therefore very high (in the order of ms) for large n [BS57].

The most probable explanation for the formation of Rydberg atoms inside the spectrometer is the alpha-decay of ^{210}Po (implanted on the spectrometer surface via the ^{222}Ra channel), which produces a ^{206}Pb ion. By sputtering atoms from the inner spectrometer surface, those atoms can travel through the spectrometer volume, and finally hitting the opposite wall. As Rydberg atoms are not charged they are not

trapped inside the magnetic bottle and are not influenced by the electric potential [FMO82, Kel82, WBOF94].

With the measured background rate in the order of 400 mcps, there have to be constant ionization processes ongoing. This is a contradiction to the pressure independent background rate for this component (see above). Another problem with this hypothesis is that the electric field between vessel and inner electrodes does not lead to an instant ionization of the Rydberg atoms [Hin18, Tro19]. Therefore the Rydberg atoms must not be highly excited. Further analyses of this spectrometer background component are ongoing.

2.3.7. Tritium induced background

There are two different ways how tritium can enter the spectrometer: neutral tritium and tritium ions. Even with the retention system in the KATRIN transport and pumping section, a small amount of tritium can enter the spectrometers. In this case, tritium ions are accelerated due to the retarding potential. Afterwards, they hit the downstream side of the pre-spectrometer or the full-metal electrodes. As the ions will be implemented and neutralized, this effect does not lead to a background signal because a β -electron would have to pass the main spectrometer potential. Also, tritium which is implanted on the main spectrometer surface does not produce a background signal since it is electromagnetically shielded.

A possible measurement method, which is sensitive to tritium implanted inside the pre-spectrometer is discussed in [Hei18]. However, the KATRIN setup cannot be operated in standard mode for such a measurement.

The only threat is tritium which enters the main spectrometer and decays inside its volume. There it can produce secondary electrons via ionization similar to the keV electrons discussed in the radon section 2.3.5.

A constant tritium flow of 10^{-14} mbar ℓs^{-1} into the spectrometer leads to an increase in the background rate of 1 mcps [MDF⁺13]. Therefore, the tritium retention in the transport and pumping section plays a crucial role for this background component and has to be analyzed in detail. Measurements which examine this reduction are presented in chapter 5 and allowed to start the first injection of tritium in the KATRIN beamline. In order to be sensitive on the tritium-induced signal, the measured background before tritium operation has to be compared with the one during operation. The background rate analysis for the first KATRIN tritium measurements is described in section 5.2.

3. Pumping Sections

The general setup of the KATRIN pumping sections are described in chapter 2. In the following, the focus is set on the pumping principles of the two systems, which are connected to the tritium loop system (see figure 3.1).

3.1. Differential Pumping Section

The first part of the KATRIN transport section is designed to reduce the tritium flow from the WGTS by five orders of magnitude. With a total length of 6.5 m, the DPS consists of five approximately 1 m long beam tube elements. Six pump ports (PP0-PP5) connect the single beam tube elements and can be approximated by cylinders with a diameter of 322 mm and a height of 715 mm. The DPS beamline builds a chicane with each beam tube element tilted by 20° against each other [Jan15, Hac17].

While two Leybold MAG-W 2800 turbomolecular pumps (TMPs) are installed on PP0, the pump ports 1-4 have only one. With these TMPs a pressure of 10^{-10} mbar can be reached [Vaca], while the pumping speed for tritium can be estimated to $2400 \ell s^{-1}$ [Mal07]. Furthermore, forepumps are installed behind the TMPs for evacuating the beam tube in case of pressures larger than 1 mbar. The pumped out tritium is transferred to the tritium recovery and will be cleaned by an isotope separation. Afterwards it is filled back in the inner loop buffer vessel (see figure 3.1 and section 2.2.1).

As the DPS magnets produce a magnetic field up to 5.5 T, the TMPs have to be surrounded by a magnetic shield. Otherwise, the magnetic field can overheat the TMP by induced eddy currents [Jan15].

The simulation of the tritium retention factor is described in section 4.2 and the results of first commissioning measurements are discussed in section 5.1.1.

3.2. Cryogenic Pumping Section

The second part of the KATRIN transport section is the cryogenic pumping section (CPS). The CPS has to reduce the tritium flow from the DPS by additional seven

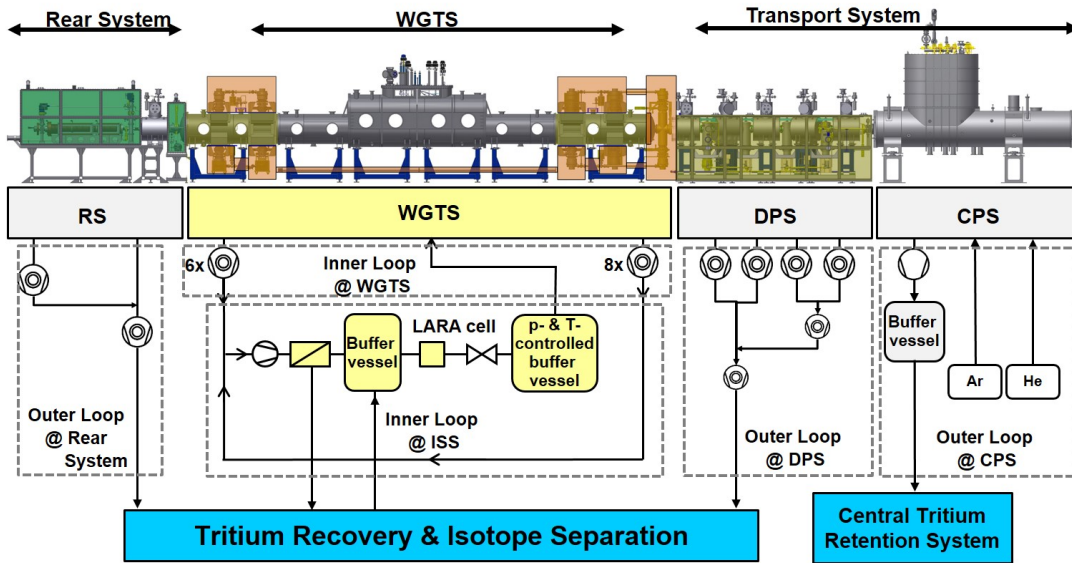


Figure 3.1.: Setup of the KATRIN loop system. The tritium, which is pumped out in the several components except the CPS by TMPs is transferred back into the buffer vessel. During this process, the tritium fraction in the pumped out gas has to be separated from other hydrogen isotopologues and gases. The injection process into the WGTS is described in section 2.2.1. For the CPS, in which the adsorbed tritium is purged out with helium after a regeneration of the argon frost layer, the tritium is taken to the central tritium retention system.

orders of magnitude. In order to fulfill this task, an argon frost layer is prepared in the beam tube sections 2-5 (see figure 2.5) and kept at a temperature of 3 K. Therefore, incoming tritium is adsorbed on the frost layer by cryosorption. After 60 days corresponding to an accumulated activity of 1 Ci, the argon frost layer is regenerated and a new one is prepared. In the following, an introduction in the principle of cryosorption is given with the focus set on argon as an adsorbent. Afterwards, the setup of the CPS is described before the necessary processes of the argon frost preparation are explained.

3.2.1. Adsorption on cold surfaces

The CPS uses the principle of cryosorption, which refers to a gas particle, which is bound to a highly porous adsorbent at a low temperature by van der Waals forces. By this definition a coverage [Hae81]

$$a = \frac{N_{\text{adsorbate}}}{N_{\text{adsorbent}}}, \quad (3.1)$$

with the number of particles in adsorbate $N_{\text{adsorbate}}$, and in adsorbent $N_{\text{adsorbent}}$ respectively.

Gaseous adsorbents can have higher characteristic temperatures (e.g. melting point, vapor pressure curve) than the gases, which should be pumped due to the high

intermediate forces between each other [Hae81]. In such a case, they are called as a cryo-deposit. This enables the pumping of hydrogen isotopologues for example with an argon cryo-deposit. In the CPS, argon is used because it has several advantages:

- It is a noble gas and does therefore not react with tritium or any other adsorbate.
- The heat transfer between the adsorbent and the surface is good.
- Very clean argon can be used for the preparation process.
- The gas can be removed after a certain time and a new layer can be prepared.

In the following, the properties for an argon adsorbent are described.

3.2.1.1. Argon properties as a cryo-stat

Solid argon crystallizes in a face-centred cubic (fcc) lattice [DJ57]. By assuming spherical atoms, the binding forces are defined by the Lennard-Jones potential [DJ57]

$$\Phi(r) = \frac{A}{r^{12}} + \frac{B}{r^6}, \quad (3.2)$$

with the characteristic constants A and B . Octahedral (111) and cubic (100) growth faces can occur when the interaction between the first next neighbors in the crystal is dominant [KS52, Hae81].

Measurements by Abe and Schulze studied the dependence of the capacity on the preparation temperature for hydrogen on noble gas frost layers [AS79]. For argon, a maximum monolayer adsorption capacity of $60 \text{ mmol}_{\text{H}_2}/\text{mol}_{\text{Ar}}$ has been found at a preparation temperature of 5.5 K. For higher temperatures, the capacity decreases for example, at 15 K it is only one third of the maximum value. Furthermore, the layer density was investigated, which starts to decrease at 20 K (approximately 25% of the argon triple point of 83.8058 K [KKL⁺17]). The density increases linearly in the range from 5 K to 10 K, resulting in an increase of the adsorbing area and higher porosity for lower temperatures [AS79].

Nepjika, Rabin, and Schulze performed atomic force microscopy measurements in order to investigate the layer thickness of argon for different low temperatures [NRS05]. The results showed that the morphology is nearly constant for layer thicknesses larger than 150 nm, if the preparation temperature is fixed (for example at 5 K). Furthermore, they observed a significant number of pores on the argon surface, with an increasing size for lower temperatures. At a temperature of 5 K, the maximum size of 65 nm is reached [NRS05]. This effect has a positive impact on the pumping efficiency as the effective surface A_0 increases by formation of pores [AS79].

The effective surface is defined by

$$A_0 = a_0 \cdot F \cdot \frac{N_{\text{ads}}}{M_{\text{ads}}}, \quad (3.3)$$

with the required space for one particle $F = 1.225 \times 10^{21} \text{ m}^2$ (for hydrogen [Hae81]), the monolayer capacity a_0 , the number of adsorbed particles N_{ads} , and the molar mass M_{ads} . Using the specific numbers for argon, A_0 can be determined for a temperature of 6 K (in this case $a_0 = 58 \text{ mmol}_{\text{H}_2}/\text{mol}_{\text{Ar}}$ [Hae81]):

$$A_0 = 1.38 \times 10^5 \text{ m}^2 \text{ kg}^{-1}. \quad (3.4)$$

The effective surface is correlated with the mean crystal size δ by [Hae81]

$$\delta = \frac{6}{A_0 \rho} . \quad (3.5)$$

This equation is valid if the condensate is assumed to be cubic with an edge length δ . ρ is the temperature dependent density of the cryodeposit, which is correlated with the porosity Φ by

$$\Phi = 1 - \frac{\rho}{\rho_0} , \quad (3.6)$$

with the particle density ρ_0 .

With this information, the capacity of an argon frost layer can be calculated for a hydrogen adsorbate. Using the argon density at 6 K of $\rho_0 = 1.77 \text{ g cm}^{-3}$, the molar mass of argon $M_{\text{Ar}} = 39.948 \text{ g mol}^{-1}$, and a porosity of 15%, the desired layer thickness δ in dependence of the number of adsorbed particles N_{ads} can be determined. For $\delta = 1 \text{ }\mu\text{m}$, the total number of adsorbed hydrogen molecules can be $5.61 \cdot 10^{20}$ corresponding to an inventory of 60 Ci tritium. However, the last calculation is only valid if tritium acts similar to hydrogen.

3.2.2. Hydrogen on frozen argon layer

Hydrogen molecules have a diameter of 0.293 nm [JOHW55], which is smaller than the distance between next neighbors on an argon crystal (0.37 nm [Zem65]). Therefore, the adsorbed hydrogen will presumably take the place at a free lattice spot. If it is a (100) face, the hydrogen will have either 5 or 8 next neighbors, if it is a (111) face, there are 5 or 9 next neighbors possible. Consequently, the binding energy ϕ for hydrogen varies depending on the neighbor numbers. For the calculation of the binding energy of each pair, the sublimation enthalpy ΔH for the adsorbate and adsorbent have to be known [KS52]

$$\phi \cdot N_A = \frac{1}{6} (\Delta H_{\text{adsorbate}} \cdot \Delta H_{\text{adsorbent}})^{\frac{1}{2}} . \quad (3.7)$$

Using the Avogadro constant N_A , the binding energy for one hydrogen molecule and one argon atom is given by 440 J mol^{-1} [BLS⁺72]. This value has to be multiplied with the number of neighbors depending on the face.

This leads to large uncertainties, which lead to large uncertainties in the argon frost pump performance. Therefore, the binding energies calculated with equation (3.7) have to be treated carefully. The TRAP experiment was performed to test the KATRIN CPS setup [EBB⁺08, Eic09]. The results revealed a binding energy of approximately 1400 J mol^{-1} for deuterium on an argon frost layer [Eic09].

3.2.3. Kinematics for adsorption and desorption processes

For cryo pumps, the rates of adsorption and desorption play a crucial role to specify their performance. Both are strongly dependent on the temperature. For a non-radioactive adsorbent, the rate of adsorption j_{ads} can be described by [Kos12]

$$j_{\text{ads}} = \frac{1}{\sqrt{2\pi k_B}} \cdot \frac{\alpha \cdot p}{\sqrt{T_{\text{gas}} \cdot M}} , \quad (3.8)$$

with the partial pressure p , the Boltzmann constant k_B , the temperature and coverage dependent sticking coefficient α , the gas temperature T_{gas} , and the molecular mass M of the gas. For hydrogen adsorbing on an argon frost layer, the sticking coefficient was found to be 0.7 at a temperature of 4.2 K [Hae81].

The desorption rate is given by [Eic09, Kos12]

$$\frac{dN_{\text{des}}}{dt} = \frac{N_{\text{ads}}}{A} \cdot \nu \cdot \exp\left(-\frac{E_{\text{des}}}{RT}\right), \quad (3.9)$$

with the number of adsorbed particles N_{ads} , the cryo-surface A at temperature T , the desorption energy E_{des} , and the universal gas constant R . $\nu \approx 10^{13}$ Hz corresponds to the solid state vibration frequencies with which the adsorbed particles vibrate. From equation (3.9), the mean sojourn time τ_{des} can be defined [Jou08]

$$\tau_{\text{des}} = \frac{1}{\nu} \cdot \exp\left(\frac{E_{\text{des}}}{RT}\right) = \tau_0 \cdot \exp\left(\frac{E_{\text{des}}}{RT}\right). \quad (3.10)$$

In order to attain a sufficient tritium retention in the CPS, τ_{des} has to be significantly larger than 5×10^6 s (corresponding to a nominal 60 d operation of the argon frost layer).

For radioactive adsorbates, the influence of radioactive decays inside of the adsorbents have to be taken into account. Additionally, the decay can cause other atoms in its vicinity to desorb. In the following, tritium is used as a radioactive adsorbate. Depending on the surface coverage s , the amount of desorbed tritium $\eta(s)$ from a single β -decay inside the argon frost layer can be described by [Mal08]:

$$\eta(s) = \eta_{\text{max}} \cdot \frac{s}{s + s_m}. \quad (3.11)$$

η_{max} is the upper limit for the desorption yield and s_m is the kink between the linear rise and the plateau where $\eta(s)$ reaches saturation [Mal08]. From reference [Mal08], the values for $\eta_{\text{max}} = 10^3$ T₂/decay and for $s_m \approx 4 \times 10^{14}$ T₂ cm⁻² can be estimated. Considering this effect, the differential equation (3.9) is now described by

$$\frac{dN}{dt} = -N \cdot \left(\frac{1}{\tau_{\text{des}}} + \sigma \cdot \eta(s) \cdot \lambda_T \right), \quad (3.12)$$

with the decay constant λ_T . The variable σ describes the number of tritium atoms in the adsorbate (for H₂: $\sigma = 0$, HT: $\sigma = 1$, T₂: $\sigma = 2$, ...). Similar to equation (3.10), a new effective time constant τ_{eff} can be defined

$$\tau_{\text{eff}} = \left(\frac{1}{\tau_{\text{des}}} + \sigma \cdot \eta(s) \cdot \lambda_T \right)^{-1}. \quad (3.13)$$

Therefore, the desorption time cannot be arbitrarily increased by reducing the temperature since τ_{eff} will converge to a limit defined by the second term.

3.2.4. Setup of the cryogenic pumping section

The cryogenic pumping section has to reduce the neutral tritium flow by at least seven orders of magnitude. In order to fulfill this task, an efficient preparation of the

argon frost layer is important. Additionally the CPS cryostat has to fulfill several tasks, which are described in the following.

In beam tube elements 2-5, a total number of 307 fins are installed increasing the inner surface to 2.536 m². Therefore, the average number of adsorptions for a particle migrating through the cold trap is increased. Simultaneously, the surface coverage and the influence on the sticking coefficient are decreased. For the frost layer preparation, the beam tube elements 2-4 are equipped with three 85 cm long capillaries with 23 orifices (see section 3.2.5). After 60 d of tritium operation, the argon frost layer is regenerated corresponding to an accumulated activity of up to 1 Ci with a surface coverage smaller than 1% (see section 3.2.5.6) [Jan15].

The cold trap is cooled down to 3 K to increase the mean sojourn time (compare equation (3.10)). In order to achieve 3 K, the CPS consists of a dedicated, multi-stage cooling system (compare to figure 2.5):

- **Liquid nitrogen cooling:** The cold nitrogen circuit cools down the outer radiation shield to a temperature of 77 K. The outer radiation shield reduces the heat load on the magnet coils operated at 4.5 K and the cold trap. Furthermore, beam tube sections 1, 6, and 7 are cooled by the liquid nitrogen. The flow through each section and the radiation shield is regulated separately by a regulation valve. Depending on the temperature of the segments, the valve position is adjusted automatically. At the end of the circuit, the nitrogen flows into an 11 ℓ vessel, operated at a filling level of 40%. In total, a capacity of 25 ℓ of nitrogen is inside the cooling circuit, provided by a transfer line¹.
- **4.5 K Helium cooling:** The 4.5 K circuit provides cooling power for a helium shield, the cold gate valve, the magnet coils, and the 3 K cooling (see next item). The flow through the different parts can be controlled via regulation valves. Due to the large volume which has to be cooled, a 1300 ℓ vessel is installed storing the liquid helium at a nominal level of 60%. Similar to the nitrogen cooling, the helium is constantly supplied by the transfer line with a mass flow of 4 g s⁻¹ (at 4.5 bar).
- **3 K Helium cooling:** For the 3 K cooling of the cold trap, a second vessel is installed, in which the pressure is pumped down. A Leybold DRYVAC DV 650 S pump with a maximum pumping speed of 650 m³ h⁻¹ holds a pressure of 0.24 bar inside the 15 ℓ vessel. With this setup a mass flow of 0.5 g s⁻¹ (at 2.5 bar) is achieved running through the cooling loop of the CPS cold trap. This is necessary because the nominal boiling temperature of helium is 4.22 K [MS59]. Due to the pumping, some helium atoms will boil leading to a first order phase transition. This process can be described by the Clausius–Clapeyron relation

$$\frac{dp}{dT} = \frac{L}{\Delta V \cdot T}, \quad (3.14)$$

with the pressure p , the temperature T , the specific latent heat L , and the specific volume change ΔV . In order to prevent a too high loss of helium due to vaporisation, only the small volume of the second vessel is pumped down. Additionally, a heat exchanger is installed cooling the 4.5 K circuit down to 3 K.

¹The transfer line provides the WGTS and CPS with helium and nitrogen.

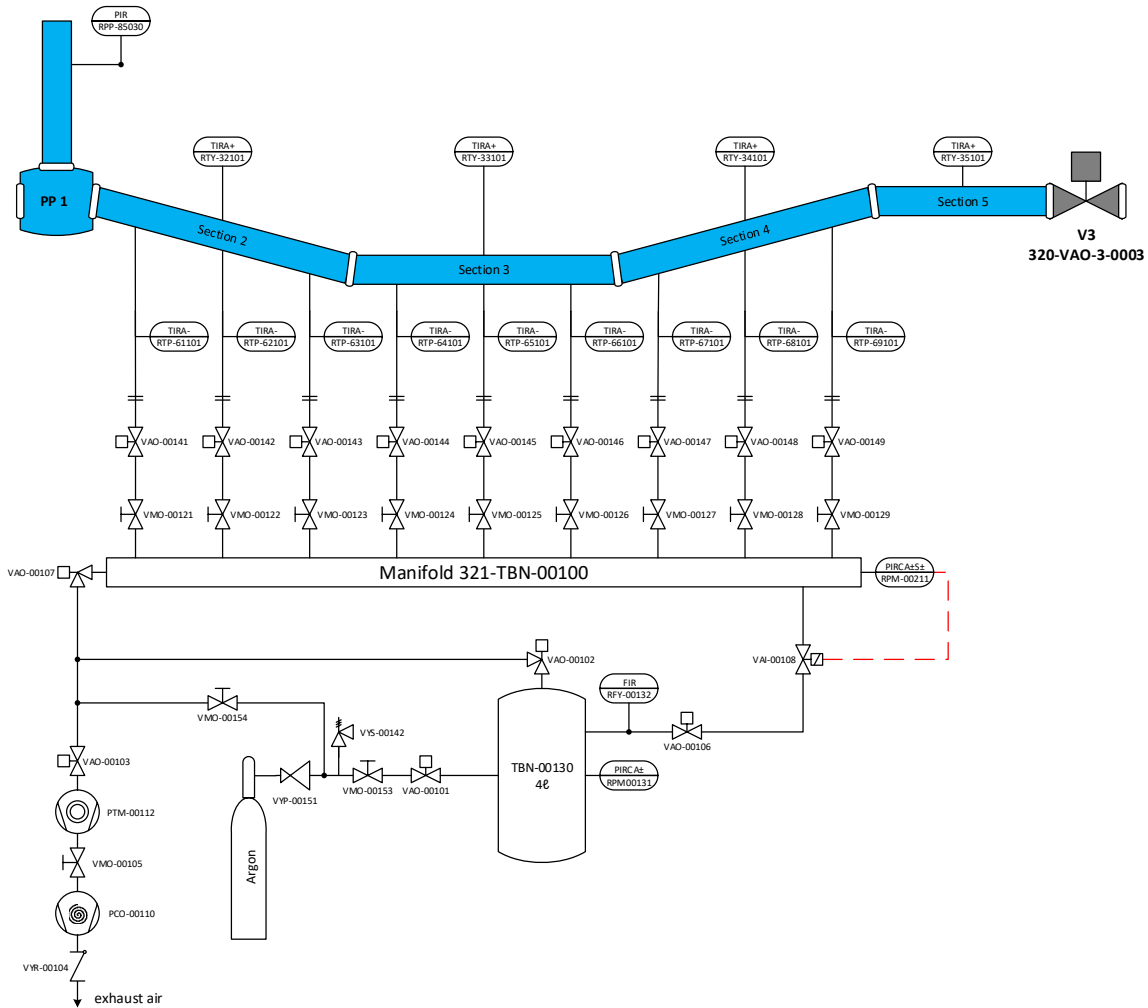


Figure 3.2.: Piping and instrumentation (P&I) diagram of argon inlet system. Shown is the process flow diagram with its different components. The main parts are described in the text.

The temperature is the important parameter of the pumping efficiency. Therefore, 24 temperature sensors monitor the temperature in the different beam tube sections. In the cold trap and around the cold gate valve, 14 rhodium iron sensors (RFY in figure E.3) are installed, which are sensitive for temperatures between 1 and 500 K. The other sensors are made of platinum (PT100) specified for temperatures above 30 K. The exact position of the sensors can be seen in figure E.3.

3.2.5. Argon frost preparation

3.2.5.1. Argon inlet system

The argon inlet system needs to fulfill the requirements for the preparation process of the cold layer. In figure 3.2 the setup is shown in a process flow diagram. The main parts are the 4 ℓ buffer vessel and a manifold, which is pressure stabilized and distributes argon into the nine capillaries. The pressure stabilization is realized by a control valve *VAI-00108*, which is regulated by the pressure in the manifold. Combining the read-out of the buffer vessel pressure together with its volume reveals the inserted argon amount into the cold trap. The pressure has to be between 100 mbar

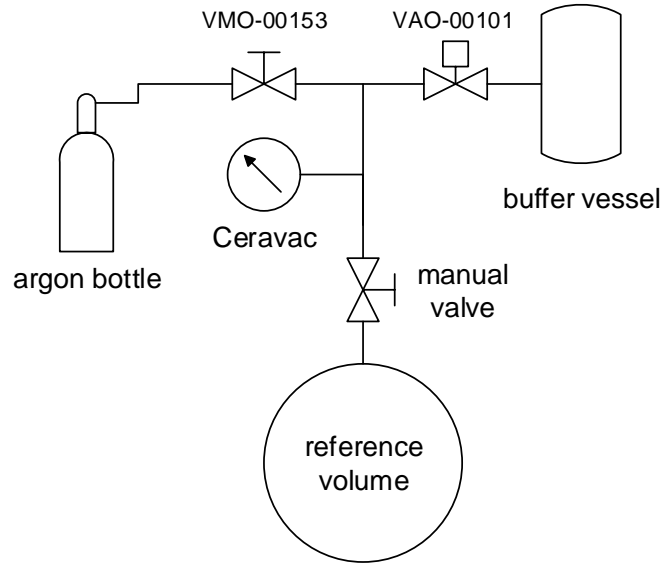


Figure 3.3.: Experimental set-up for buffer vessel volume measurement. The calibrated volume, a manual valve, and a *Ceravac CTR 100 N* pressure sensor are connected between the valves *VMO-00153* and *VAO-00101*. Within this setup the effective volume of the buffer vessel is measured.

and 950 mbar preventing both a too low and high flow rate into the cold trap. In order to avoid freezing of argon, the argon capillaries are heated up to 75 K. If the temperature drops below 70 K the preparation process is stopped automatically. Another interlock is triggered by the temperature of the cold trap, which has to be colder than 10 K. The buffer vessel can be evacuated via a turbo molecular pump, which is used before and after the preparation.

3.2.5.2. Buffer vessel volume

Since the volume of the buffer vessel V_{buf} plays a crucial role for the insertion of the right argon pV amount into the cold trap, a dedicated measurement was performed. The defined volume does not only include the buffer vessel itself but also the piping to the closed valves during the begin of preparation. Therefore, a reference volume $V_{\text{ref}} = (6332.501 \pm 22.164) \text{ ml}$ and a pressure gauge (*Ceravac CTR 100 N*) were connected between the argon bottle and the valve *VAO-00101* to the buffer vessel. This reference volume was filled with argon to a pressure of $p_0 = 300 \text{ mbar}$ while the rest of the setup was evacuated. By opening the manual valve to the volume between reference volume and buffer vessel (see figure 3.3), the pressure dropped to p_1 enabling the determination of the intermediate volume V_{int} . Afterwards the valve *VAO-00101* to the buffer vessel was opened, which again led to a pressure drop to p_2 . This procedure was repeated two times.

The buffer vessel volume can be calculated by the ideal gas law assuming a constant temperature during the measurement time of 2 min

$$p_0 \cdot V_{\text{ref}} = p_1 \cdot (V_{\text{ref}} + V_{\text{int}}) = p_2 \cdot (V_{\text{ref}} + V_{\text{int}} + V_{\text{buf}}) , \quad (3.15)$$

with the pressure p_1 (p_2) after opening the manual valve (*VAO-00101*). Solving the first equation for V_{int} and apply it for the second one leads to

$$V_{\text{buf}} = p_0 \cdot \left(\frac{1}{p_2} - \frac{1}{p_1} \right) \cdot V_{\text{ref}} \quad (3.16)$$

With the measured values (see appendix A) together with an uncertainty of 0.2% of the pressure reading given by the manufacturer [Ley18] the buffer vessel volume can be calculated

$$V_{\text{buf}} = (4254.7 \pm 17.5) \text{ m}\ell . \quad (3.17)$$

3.2.5.3. Conductances of argon capillaries

In order to compose a preparation procedure, the differing conductances of the nine argon capillaries have to be measured at nominal conditions. A measurement with the CPS at room temperature has been done in [Röt16], but due to the strong correlation between conductance and temperature a repetition is necessary.

Therefore the following settings were used:

- cold trap temperature at 6 K,
- the heaters installed at the argon capillary to a target temperature between 75 K and 77 K,
- pressure in the manifold to 2 mbar.

At the beginning of each individual measurement, the buffer vessel was filled to a pressure of 895.1 mbar while the other parts of the argon inlet system were evacuated. Afterwards valve *VAO-00106* was opened so that the manifold was filled to a pressure of $p_{\text{in}} = 2$ mbar. One valve of an argon capillary was opened until the pressure in the buffer vessel dropped by $\Delta p = 5$ mbar measuring the required time. This procedure was repeated three times for each capillary. With the averaged measured time \bar{t}_i the conductance can be calculated by

$$C_i = \frac{q_{pV,i}}{p} = \frac{\Delta p \cdot V}{\bar{t}_i} \cdot \frac{1}{p_{\text{in}}} . \quad (3.18)$$

For the determination of the uncertainties the Gaussian error propagation is used applying

- 0.12% for $\sigma(\Delta p)$, [MI18]
- 30.24 mℓ for σV ,
- the standard deviation of the three measured times for $\sigma(\bar{t}_i)$,
- 1% for $\sigma(p_{\text{in}})$ [MIb].

The results are listed in Tab. 3.1. The conductances deviate from their mean value by a maximum of 12%, which has to be considered at the preparation process.

Table 3.1.: Conductances of argon capillaries. Measured conductances of the nine argon capillaries with their appendant uncertainties.

Capillary	Conductance in ml s^{-1}	Conductance uncertainty in ml s^{-1}
1	55.0	1.7
2	57.2	2.9
3	60.7	3.0
4	61.6	0.8
5	55.7	2.7
6	67.5	1.7
7	60.4	1.5
8	58.0	2.7
9	66.8	1.0

3.2.5.4. Amount of argon needed for argon frost preparation

The required amount of argon needed for the preparation can be calculated by using the precondition of a layer thickness of $\delta = 3 \mu\text{m}$ [Jan15]. For the calculation the following values are used

- inner beam tube surface of elements 2-4: $A = 2.197 \text{ m}^2$
- molar mass of argon: $M_{\text{Ar}} = 39.948 \text{ g mol}^{-1}$
- density of argon at 6 K: $\rho_0 \approx 1.77 \text{ g cm}^{-3}$ [Hae81]
- porosity: $\Phi = 0.15$

With equation (3.6), the required argon mass can be determined as

$$m = (1 - \Phi) \cdot \rho_0 \cdot \delta \cdot A = 9.92 \text{ g} \quad (3.19)$$

Using the ideal gas law, the mass can be converted into a pV amount (the buffer vessel is at room temperature $T = 293 \text{ K}$)

$$pV = \frac{m \cdot N_A \cdot k_B \cdot T}{M_{\text{Ar}}} = 6042 \text{ mbar } \ell . \quad (3.20)$$

With a maximum buffer vessel pressure of 950 mbar, the necessary pV amount can not be stored. Therefore, the buffer vessel has to be refilled one time during the preparation process.

3.2.5.5. Preparation procedure

For the argon frost preparation, the buffer vessel is filled to a pressure of 925 mbar and the beam tube temperature of sections 2-5 is warmed up to 6 K. When these starting conditions are fulfilled, the valves to the nine capillaries are opened simultaneously. The valves close automatically after reaching a specific pressure so that the same amount of argon is injected through each capillary. The buffer vessel volume (see section 3.2.5.2) and the conductance measurement of section 3.2.5.3 were used for the calculation. The pressures to the corresponding capillaries are listed in table 3.2 (compare figure 3.2). When all valves are closed, the procedure is repeated for one time. Finally, the cold trap temperature is cooled down to 3 K.

Table 3.2.: Argon preparation pressures. The pressure values at which the valve to the corresponding capillary is closed are listed.

capillary	pressure in mbar
1	220
2	232
3	258
4	236
5	214
6	281
7	222
8	215
9	262

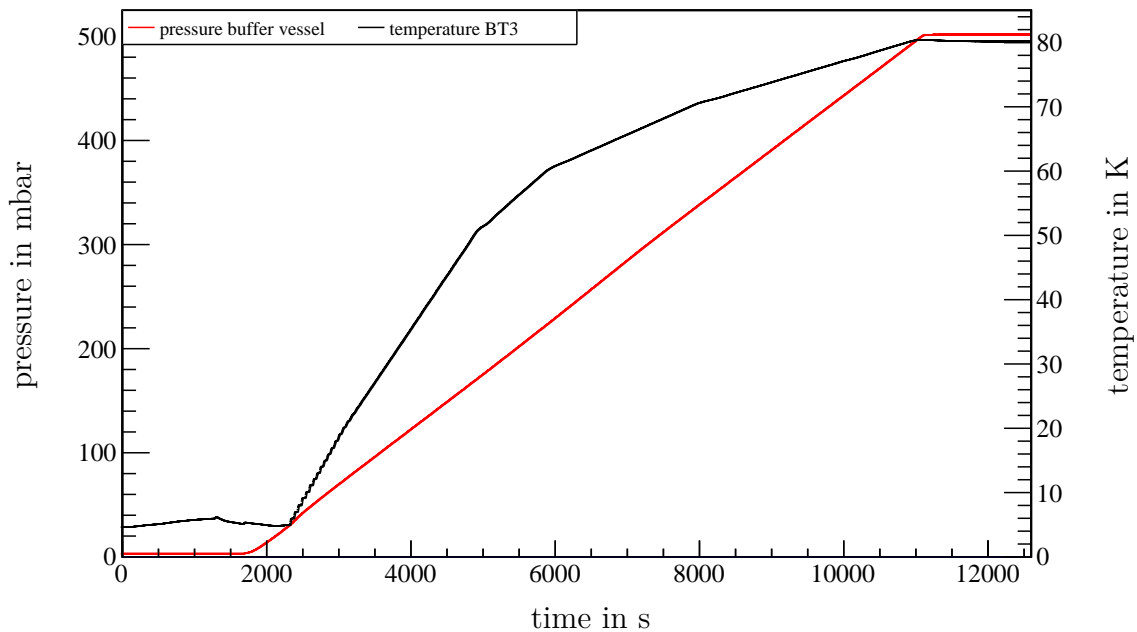


Figure 3.4.: Helium purging. The pressure in the 506 ℓ buffer vessel and the temperature in beam tube 3 is plotted over time during helium purging.

3.2.5.6. Helium purging

After 60 d of operation, an accumulated activity of 1 Curie is stored on the cold trap. In order to prevent tritium from further migrating and eventually reaching the spectrometer section, the argon frost layer is regenerated. Therefore, a helium purging and pumping system is connected to the CPS. During purging the valve between DPS and CPS, and the cold gate valve are closed. While helium is injected via a stable flow of 1000 sccm into beam tube section 5, the gas is pumped into a 506 ℓ buffer vessel at DPS-PP5 and CPS-PP1. Simultaneously, the cold trap temperature is warmed up to 80 K using heaters installed at each beam tube section and closing the valve from the 4.5 K vessel to the beam tube cooling pipe. When the buffer vessel pressure reaches 500 mbar, the valve *VAO-85170* to beam tube 5 is closed automatically. As a result the heating has to be controlled so that during the end of the process the beam tube temperature is at 80 K. This is realized by four different slopes in certain temperature regimes, which can be seen in figure 3.4. The slopes originate from the power of the beam tube heater; for a temperature lower than 40 K a short-time switch-on leads to a high rise of the beam tube temperature. For higher temperatures, it is important to have a smaller gradient because in this case the temperature discrepancies inside the cold trap become larger. With smaller gradients these temporary colder beam tube areas have more time to warm up.

At the end of the helium injection the turbo molecular pump connected to CPS-PP1 (see appendix C.1) is turned on. When a pressure inside the beam tube below 10^{-6} mbar is reached, the beam tube will be cooled down to 3 K again.

4. Simulations of reduction factors

Simulations play an important role for comparing measurement results with predictions. In case of the KATRIN source and transport section (STS), the gas flow changes from laminar flow of the tritium injection into the WGTS to molecular flow at the end of the WGTS. In order to investigate the performance of the DPS and CPS, especially the retention of neutral tritium, molecular flow simulations are performed. Since the pressure gauges cannot be installed close to the beam line, the measured pressure does not directly convert into a reduction factor. Dedicated simulations are needed to derive the reduction factor from the measured pressure ratio.

In section 4.1 the simulation programs are described, which are used to simulate the reduction by the differential pumping section (section 4.2) and by the cryogenic pumping section (section 4.3).

4.1. Simulation programs

Two simulation programs, MolFlow+ and COMSOL Multiphysics[®], are used when simulating the reduction factor of the DPS and CPS. In the following both programs are shortly described.

4.1.1. MolFlow+

MolFlow+ is a test particle Monte Carlo tracking software developed for the molecular flow regime at CERN [KA14]. The geometry of a model is composed of so-called facets, which are flat polygons combined to a mesh that represents the 3-d surface of the vacuum chamber. To each facet physical parameters can be assigned, such as the sticking probability, for impinging gas molecules, the temperature of the surface, its opacity, and the type of reflection (diffuse or specular). Furthermore, a facet defined as a desorbing surface, represents the starting point of simulated particle trajectories. Each facet has three counters, which are incremented each time a particle desorbs (N_{des}), hits the facet (N_{hit}), or is adsorbed (N_{ads}). If a particle is absorbed, the simulation of the particles trajectory stops. In order to include a

pump, the corresponding sticking coefficient has to be chosen. For the simulations performed within this chapter, Knudsen’s cosine law is used describing diffuse reflections. The velocity after scattering of a particle at a wall is calculated assuming a total thermalization using Maxwell’s velocity distribution.

In summary, MolFlow+ is an efficient tool to determine effective pumping speeds, conductances, and pressure distributions in the molecular flow regime.

4.1.2. COMSOL Multiphysics

COMSOL Multiphysics[®] is a commercial simulation software package, which uses the finite element method in order to solve physical problems. There are several modules available, each implies the physical environment for a particular physical field. The decision which one to use (one or more), has to be made first; within this work the heat transfer module is applied to investigate the CPS’s cold trap temperature distribution. With the implementation of a 2D or 3D geometry either built in COMSOL Multiphysics[®] or imported from a CAD file, the corresponding materials (with all their physical properties) can be chosen. In the heat transfer module, initial temperature values have to be defined. With the addition of heat sources, e.g. via radiation, different effects can be taken into account. After all basic physical conditions are specified, a mesh has to be defined for the geometry of each component. With the mesh, the geometry is simplified for example by triangular shapes. This step has an impact on the computation time and accuracy of the simulation results. In general, a triangular mesh is used.

COMSOL Multiphysics[®] offers the possibility to make either a stationary or a time-independent simulation. In this chapter only stationary simulations were performed, since the CPS conditions are stable during nominal KATRIN operation.

4.2. DPS reduction factor simulation

In order to simulate the DPS reduction factor the beamline geometry has been imported from the CAD model into MolFlow+, as shown in figure 4.1. It contains about 19000 facets and includes the downstream end of the WGTS. Inside the beam tube, the dipole and blocking electrodes are included since they affect the tritium flow.

The trajectory of a particle ends when it is either pumped out by one of the six TMPs, it hits the valve V2, or it is backscattered into the WGTS reaching the last WGTS pump port. For the last two cases, a sticking coefficient $\alpha = 1$ is assigned to the corresponding surfaces, since the probability for a particle which enters the WGTS or the CPS to be pumped away is assumed to be close to 1. This setup allows a proper connection condition for the CPS MolFlow+ simulation discussed in section 4.3.2. The pumping speed of the TURBOVAC MAG W 2800 can be transformed into a sticking probability $\alpha = 0.252$ (for $M = 6 \text{ g mol}^{-1}$) by using an empirical model by Malyshev [Mal07] (see appendix D). An uncertainty of 20% is assumed for the model.

Simulating the DPS geometry in one process is very time consuming. In order to avoid long simulation times, the geometry is subdivided into several parts, which

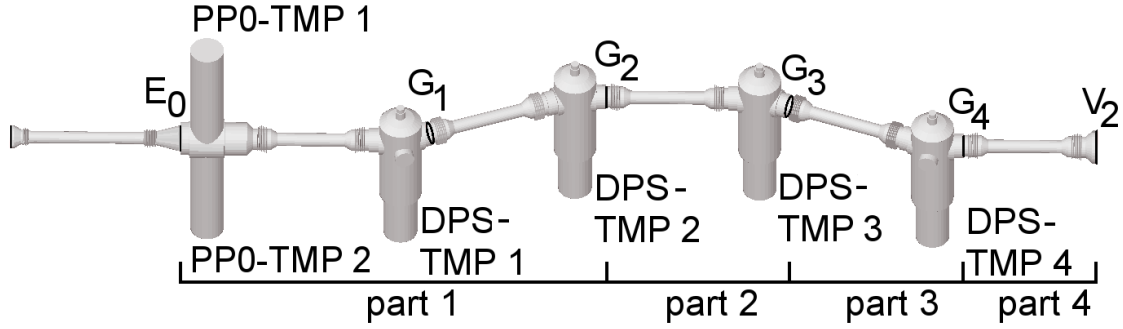


Figure 4.1.: Model for DPS MolFlow+ simulation. The DPS beam tube is split into four different parts, which are marked below. All the six TMPs, the virtual facets G1-G4 used for the reduction factor calculation, and the two valves E0 (corresponds to V1) and V2 are labeled [FRS⁺19].

Table 4.1.: DPS tritium reduction factor simulation. Results of the DPS gas flow simulation with MolFlow+ for tritium.

Part	Desorption	Inlet & outlet	Inlet counts	Outlet counts
1	E_0	E_0 & G_2	36901582	466310
2	G_1	G_2 & G_3	3385527	342948
3	G_2	G_3 & G_4	809346	82173
4	G_3	G_4 & V_2	2142160	104502

are simulated independently. This results in higher statistics (more hits) for the downstream end of the DPS [Jan15]. For the calculation of the total DPS reduction factor, the simulated results of the individual parts are combined to

$$\begin{aligned}
 R_{\text{tot}} &= R_1 \cdot R_2 \cdot R_3 \cdot R_4 \\
 &= \left(\frac{N_{\text{des},E_0}}{N_{\text{hit},G_2}} \right)_{\text{part 1}} \cdot \left(\frac{N_{\text{hit},G_2}}{N_{\text{hit},G_3}} \right)_{\text{part 2}} \cdot \left(\frac{N_{\text{hit},G_3}}{N_{\text{hit},G_4}} \right)_{\text{part 3}} \\
 &\quad \cdot \left(\frac{N_{\text{hit},G_4}}{N_{\text{ads},V_2}} \right)_{\text{part 4}} .
 \end{aligned} \tag{4.1}$$

Here N_{des,E_0} denotes the number of desorbed particles from E_0 , while N_{ads,V_2} accounts for the adsorbed particles on V_2 . In the brackets $N_{\text{hit},G_{2-4}}$ correspond to the number of hits on the facet separating the particular simulation part. In order to have a comparable forward-pointed velocity distribution to a single-pass simulation, the particles were started at G_{1-3} from the preceding beam tube part using the cosine law. Under this condition, the factorization of the reduction in equation (4.1) is allowed.

With the results given in table 4.1, the DPS reduction factor is calculated using equation (4.1)

$$R_{\text{T2}} = (1.577 \pm 0.008_{\text{stat.}}) \times 10^5 . \tag{4.2}$$

For the statistical uncertainty of each ratio in equation (4.1) binomial statistics is used. In order to tackle the high systematic uncertainty for the TMP sticking coefficient, a simulation with a 20% reduced pumping probability was performed.

Table 4.2.: DPS deuterium reduction factor simulation. Results of the DPS gas flow simulation with MolFlow+ for deuterium.

Part	Desorption	Inlet & outlet	Inlet counts	Outlet counts
1	E_0	E_0 & G_2	3093804	590269
2	G_1	G_2 & G_3	3357767	385326
3	G_2	G_3 & G_4	1761579	202524
4	G_3	G_4 & V_2	3142989	152250

The reduction factor is thereby reduced to

$$R_{T_2}^{\text{lower}} = (8.99 \pm 0.05_{\text{stat.}}) \times 10^4 . \quad (4.3)$$

Even for the lower limit, the simulated reduction factor is close to the requirement of 10^5 .

Since deuterium is used for commissioning measurements, new simulations had to be performed with the different sticking coefficient for the TMP. The pumping speed of the MAG W2800 for deuterium is given by

$$C_{D_2} = 255 \ell \text{ s}^{-1} , \quad (4.4)$$

which corresponds to $\alpha_{D_2} = 0.195$.

The results are listed in table 4.2. Therefore, the reduction factor

$$R_{D_2} = (8.20 \pm 0.03) \times 10^4 \quad (4.5)$$

is smaller than the one for tritium.

In order to measure a reduction factor, the pressure gauges at the DPS pump ports are used. Since they are not located at the beginning (V1) and the end (V2) of the DPS beam tube, two ad-hoc factors $k_{PP1/PP2,D_2}$ and $k_{PP1/PP3,D_2}$ have to be introduced to calculate the DPS reduction factor from the observed pressure ratio

$$R_{D_2} = k_{PP1/PP2,D_2} \cdot \frac{p_{PP1}}{p_{PP2}} = k_{PP1/PP3,D_2} \cdot \frac{p_{PP1}}{p_{PP3}} \quad (4.6)$$

Therefore, the pressures at the facets corresponding to the location of the pressure gauges have to be evaluated. Using the linear relation of the pressure and the number of hits divided by the surface area [KA14], the ad-hoc factors yield

$$k_{PP1/PP2,D_2} = 9500 \pm 3000 , \quad (4.7)$$

and

$$k_{PP1/PP3,D_2} = 200 \pm 80 . \quad (4.8)$$

The uncertainties are large due to the limited statistics. With these ad-hoc factors the measurement discussed in section 5.1.1 can be analyzed but have to be treated carefully because of the uncertainty.

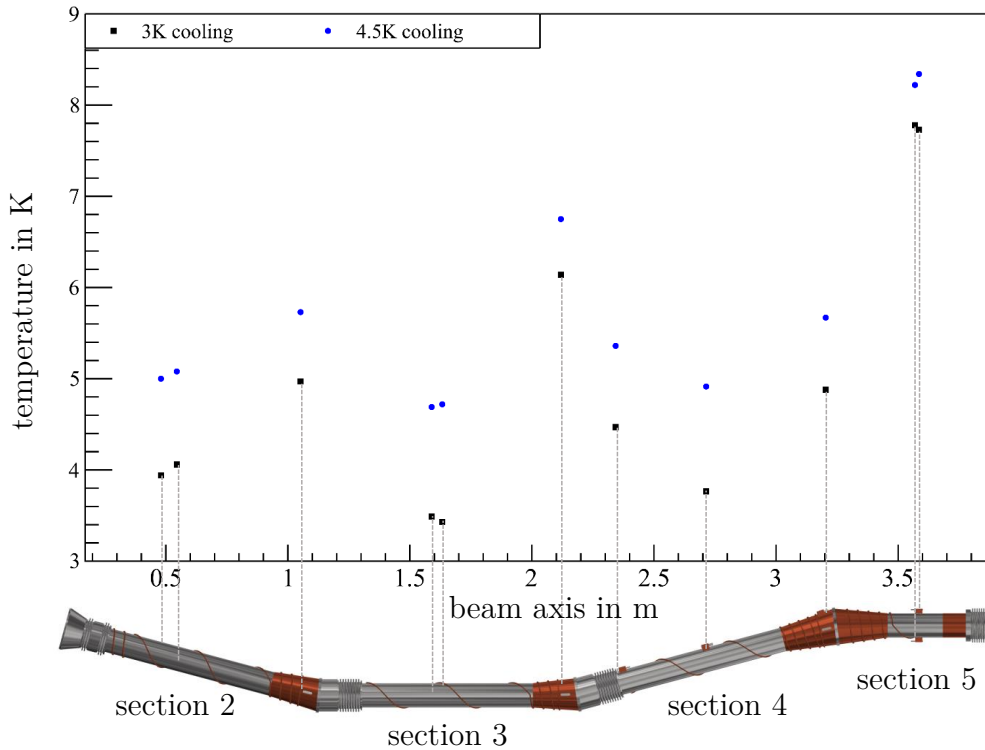


Figure 4.2.: Temperature values of CPS cold trap. The measured values of the cold trap temperature sensors are plotted over their position for both the 3 K and 4.5 K cooling. At the bottom a CAD drawing of the cold trap is shown, which is connected with the measured temperatures. The cones referred to in the text are the copper plated parts in between the sections.

4.3. CPS reduction factor simulations

For the second part of the transport and pumping section, the requirements for a reduction factor simulation are more complex, since it has to take into account additional desorption processes. In order to calculate the mean sojourn time (see equation (3.10)) of an absorbed particle on a cold surface, the temperature of the beam tube has to be known. Therefore a simulation with COMSOL Multiphysics[®] was performed as shown in section 4.3.1. Using these parameters as input, MolFlow+ simulations are performed. In order to take thermal desorptions into account, a slicing method was developed, which will be described in section 4.3.2. In section 4.3.3 a semi-analytical tracking model is used to include desorption from tritium β -decays inside the CPS beam tube.

4.3.1. Cold trap temperature simulation

The measured temperature values after the first cool-down of the CPS showed that no temperature sensors attached to beam tube elements 2-5 did reach the nominal temperature of 3 K. The measured data is shown in figure 4.2 for the 3 K and the 4.5 K cooling. At beam tube section 3 two temperature sensors reach a minimum close to 3.4 K if the 3 K cooling is activated. All sensors located at the cones connecting the beam tube sections show a temperature higher than the ones in the middle of

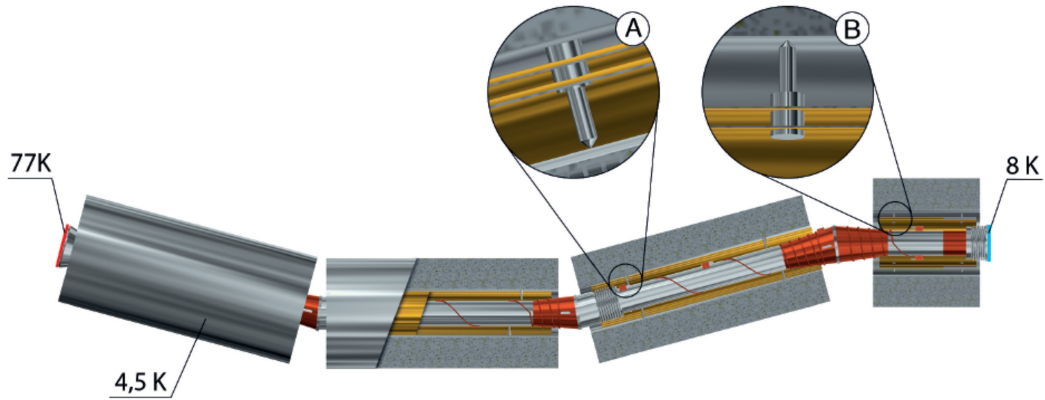


Figure 4.3.: Schematic drawing of the imported cold trap model. In gold the two radiation shields can be seen, which are located in between the surrounding magnet housing and the beam tube of each section. In the zoom A and B, the different orientation of the bolts connecting to the beam tube in case of sections 2-4 and to the magnetic coil in case of section 5 are displayed. This figure is taken from [Sch17].

the beam tube. The only exception is beam tube section 5, where the temperature is around 8 K. The deviation of the set point and the actual temperatures for both 3 K and 4.5 K cooling are correlated for each sensor, which indicates that there has to be a relation with the position on the beam tube.

Since the temperature has a strong influence on the desorption time (see equation (3.10)), a study of the temperature profile is important for the simulations of the CPS reduction factor. With the commercial simulation program COMSOL Multiphysics® a detailed analysis of the temperature distribution was made using the heat transfer module.

In figure 4.3 the model of the cold trap is shown. In order to improve the calculation efficiency, some parts of the real set-up were omitted in the model, for example the heating belt since their influence on the outcome of the temperature distribution is negligible. Therefore, only the magnetic coils 2-5, the inner radiation shields, the 3 K cooling loop, which is connected to the beam tube, and the beam tube itself have been included. The other parts which influence the temperature distribution by radiation have been taken into account by setting an ambient temperature. This assumes a uniform thermal black body radiation with a specific temperature from parts where no geometry element is defined. Furthermore, the radiation was only enabled between facets directly facing each other, which further reduced the calculation time. However, inside the beam tube, the radiation was turned off since it is only a minor effect compared to the heat load, which comes from the outer regions.

The following fixed settings were used:

- i) The cooling loop around the beam tube was set to 3 K.
- ii) The surface of the magnetic coils is at 4.5 K.
- iii) The temperature at the beginning of the CPS beam tube section was set to 77 K.

- iv) The cold gate valve was assumed to be closed with a temperature of 8 K.
- v) Emissivity, specific heat, and thermal conductivity were set to the respective material properties.

During the simulations, the ambient temperature was adjusted minimizing the temperature difference between measurement and simulation. Another reference point was the temperature of the inner radiation shield of section 3, which is equipped with an additional temperature sensor. This sensor measured an extrapolated value of about 27 K¹. Since the inner radiation shields are not actively cooled, but connected to the beam tube (in case of section 2-4), they directly indicate the temperature that is reached in thermal equilibrium with the surrounding radiating surfaces. If the temperature of the surrounding helium shield (13 K on average) is assumed as ambient temperature, the result is a uniform temperature distribution of 3 K, which is in contradiction with the measured values. In order to adjust the simulation temperature of the radiation shield, the ambient temperature was increased to 71 K to 87 K depending on the beam tube section [Sch17].

In figure 4.4, the final result of the simulation can be seen. The deviations are smaller for the sensors which are located in the middle of the beam tube where radiation has less impact. Since these are also the points with the lowest temperature, and therefore, a higher desorption time they dominate the tritium retention efficiency. It is important to describe these sections most accurately. Especially for the beam tube sections 2-4 the simulations are in very good agreement with the measured data, while at beam tube 5 the deviations are larger. A possible explanation for this behavior is that after a repair during the manufacturing of the CPS a 180 mm stretch of the cooling loop was not properly brazed to the beam tube resulting in an unpredictable thermal contact. In general, the simulation shows that the temperature of those parts close to the cooling loop of the beam tube can reach the nominal temperature of 3 K, while further away the temperature increases. For parts with narrow windings of the cooling loop (for example at the end of beam tube section 2), the temperature is more homogeneous. The influence of connecting bolts of the radiation shields can be seen as hot spots at beam tube sections 2-4. However, their influence is negligible compared to the heat load, which results from radiation at the bellows. The thermal radiation looks through a gap between the magnetic coils and the corresponding inner radiation shields. The origin of the dominant radiation are the pump ports, which are only partly cooled by nitrogen. The power radiated from a surface is proportional to T^4 according to the Stefan-Boltzmann law. Therefore, a temperature in the range of 80 K represents a major heat load.

Another point which confirms this hypothesis is the influence of the state of cold gate valve V3. With V3 closed the temperature at beam tube 5 decreases by about 3 K because V3 is cooled to a temperature of about 7 K. When V3 is open, the radiation from beam tube 6 at 70 K dominates the heat load.

In retrospect, a better solution would have been to install denser windings over the whole beam tube to decrease the temperature inhomogeneities. With the present set-up, the sections with the highest pumping efficiencies will be in the middle of beam tubes. In order to investigate the influence of the temperature profile on the

¹The temperature sensor is only specified down to 30 K; however, the measured resistance was extrapolated linearly to 27 K.

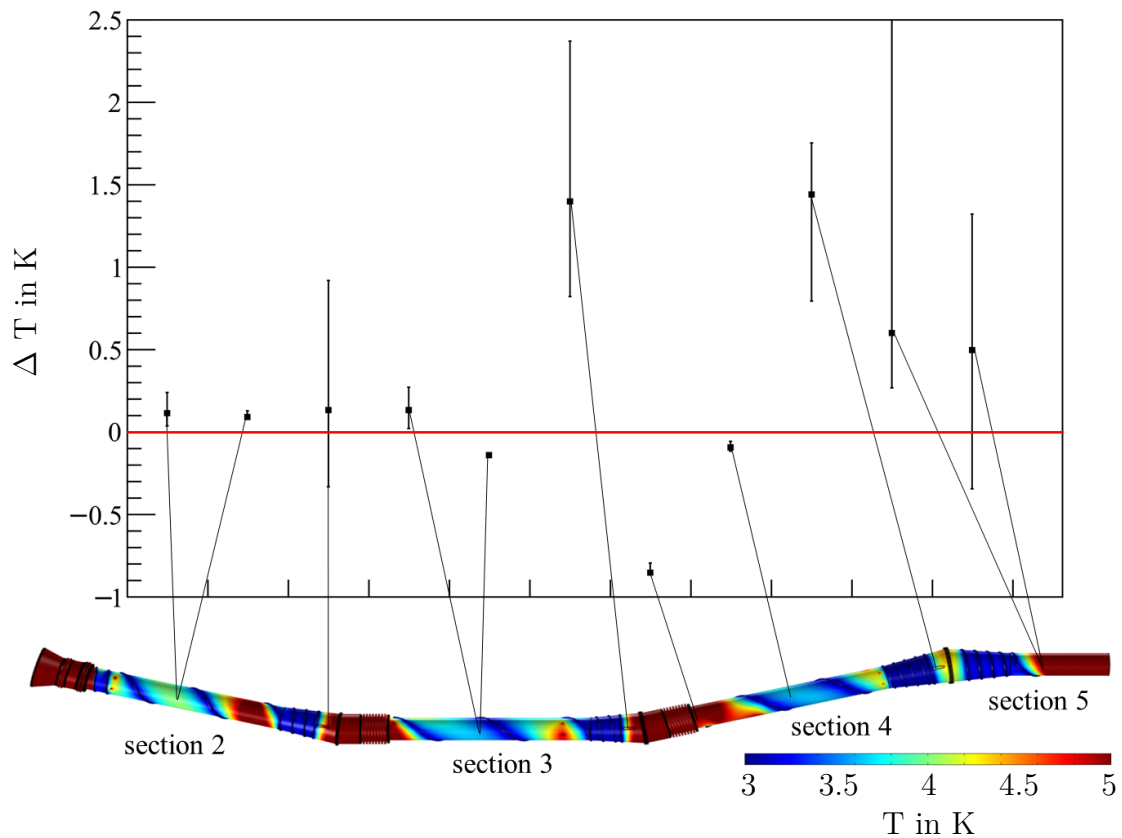


Figure 4.4.: Temperature deviation between measurement and simulation. The upper plot shows the temperature difference between measurement and simulation for the corresponding sensor. The error bars indicate the temperature uncertainty at the locations (which are partly caused by the sensor housing). For each sensor a line connects the associated value to the location on the temperature distribution of the beamline shown on the bottom plot [FRS⁺19].

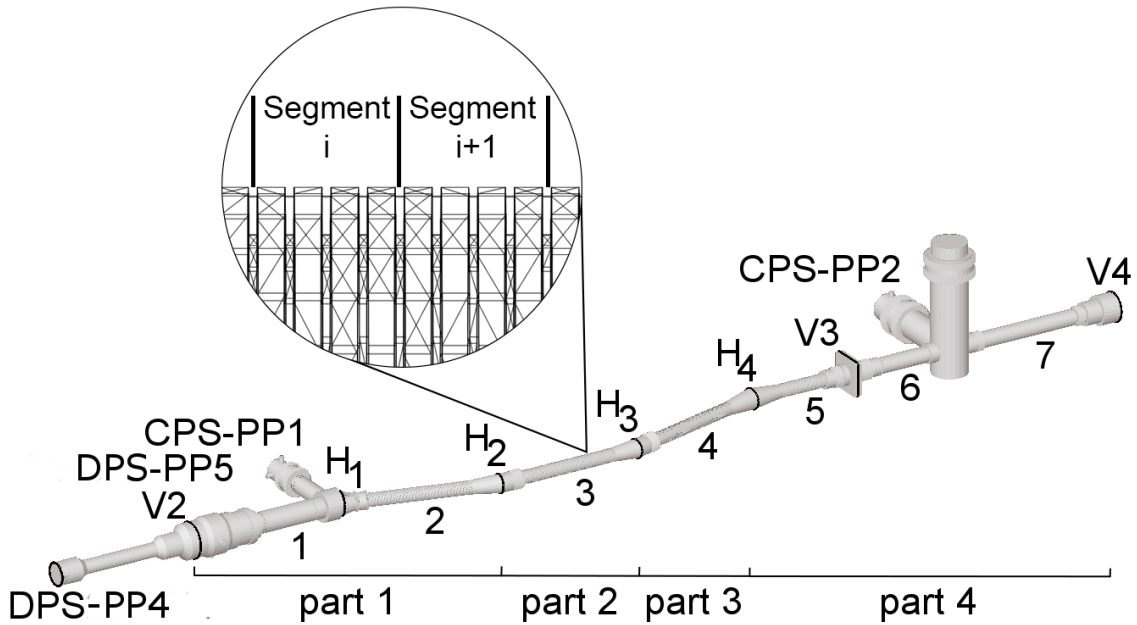


Figure 4.5.: MolFlow+ model for CPS simulation. The 7 CPS beam tube sections (1-7) are combined into four parts. They connect valve V2 at the end of the DPS and valve V4 at the pre-spectrometer. The cold gate valve V3 marks the end of the cold trap (beam tube section 2-5). The pump ports (CPS-PP1/2) contain vacuum gauges. The connecting beam tube element of the DPS between DPS-PP4 and V2 is also part of the model. In the enlargement, the geometry of two of the 107 segments is shown. In general, a segment consists of 4 fins. The virtual facets H_i separate the different beam tube sections. The figure is adapted from [FRS⁺19].

reduction factor, the simulated temperature values are used in the following vacuum simulations.

4.3.2. MolFlow+ simulation

The first simulation of the CPS reduction factor was performed with MolFlow+. In contrast to the DPS simulation, for the cold trap not only adsorption has to be taken into account but also the desorption of tritium after a mean sojourn time defined by equation (3.10). Since the desorption rate depends on the surface density of the tritium, the cold CPS beam tube sections (figure 4.5, sections 1-5) were subdivided into 102 segments with a length of 3.2 cm each in the straight beam tube parts. The cones at both ends of each section count as one segment each. For each segment, the number of hits, adsorptions, and desorptions are counted. During commissioning measurements the two TMPs at PP1 and PP2 were turned off. Their pumping speed was not included in the simulation. Particles which are reflected back into the DPS reaching the last DPS TMP are considered to be pumped out in the DPS-PP4 and so a sticking coefficient of $\alpha = 1$ is appointed there. This is in agreement with the previous DPS simulation, where all particle tracks entering the CPS were also terminated. If a particle enters the pre-spectrometer, it is also assumed to be pumped away due to the high pumping speed of the NEG pumps for hydrogen isotopologues compared to the conductance between cold trap and pre-spectrometer.

Similar to the DPS simulation the geometry again was subdivided into four parts reduce the simulation time. For all surfaces, except V2, V4, and the cold trap the sticking coefficient is set to 0. Since the cold trap sticking coefficient is unknown, several simulations were performed with α varying from 0.0 to 0.7 in 0.1 steps².

A simulated particle track always started at V2 and stopped when the particle was adsorbed. However, due to the thermal desorption (see equation (3.10)) the gas diffuses towards the pre-spectrometer following the density gradients. Shortly after starting a simulation with clean CPS walls, this results in a decreasing reduction factor over time for a constant inlet flow from the DPS.

When dividing the cold trap into $n = 102$ segments, each segment is treated as an individual cryo pump, where a particle can adsorb and redesorb. For more details see reference [Fri17]. With this setup, the number of adsorbed particles A_i on the corresponding surface i is defined by a coupled differential equation system

$$\frac{dA_i(t)}{dt} = \Phi_{\text{in}} \cdot U_{\text{des,V2}}^{\text{ads},i} + \sum_{j=1}^n \left(\frac{A_j(t)}{\tau_{\text{des}}} \cdot U_{\text{des},j}^{\text{ads},i} \right) - \frac{A_i(t)}{\tau_{\text{des}}}. \quad (4.9)$$

The first term accounts for the constant inlet flow Φ_{in} from the DPS multiplied with the probability $U_{\text{des,V2}}^{\text{ads},i}$ that a particle desorbing from V2 is adsorbed on segment i . The second term describes the sum of adsorbed particles on i , which originate from desorption off other segments j taking into account the amount of already adsorbed particles on j . The last term accounts for the desorption off the surface i . Equivalent to the decay probability $\lambda = 1/\tau$ of a radioactive decay, the desorption probability per time is described by $\lambda = 1/\tau_{\text{des}}$.

The main task of the simulation is to get values for the desorption matrix

$$U_{\text{des},j}^{\text{ads},i} = \frac{N_{\text{ads},i}}{N_{\text{des},j}}, \quad i \in [1,103] \text{ and } j \in [0,102] \quad (4.10)$$

and the hit matrix

$$V_{\text{des},j}^{\text{hit},i} = \frac{N_{\text{hit},i}}{N_{\text{des},j}}, \quad i \in [1,105] \text{ and } j \in [0,102] \quad (4.11)$$

which is proportional to the pressure. Both matrices U and V represent the probability for a desorbed particle from segment j to be adsorbed on respectively hits segment i . While i and j include all 102 segments, there are some other surfaces specified; V2 is defined as segment $j = 0$, V4 as segment $i = 103$, and two facets $i = 104$ and $i = 105$ for the pressure gauges at CPS-PP1 and CPS-PP2. These facets are needed for converting measured pressure ratios into a reduction factor.

Due to the long beam tube and huge reduction factor, a concatenation algorithm was used similar to the DPS. This affects the calculation of $V_{\text{ads},i}^{\text{des},j}$ and $U_{\text{ads},i}^{\text{des},j}$ probabilities for desorptions by segments in part 1 corresponding to $j \in [1,27]$. Three different cases have to be distinguished for $j \in [1,27]$:

- i) The segments i and j are located in the same or in the neighboring beam tube part implying:

$$U_{\text{des},j}^{\text{ads},i} = \frac{N_{\text{ads},i}}{N_{\text{des},j}} \text{ and } V_{\text{des},j}^{\text{hit},i} = \frac{N_{\text{hit},i}}{N_{\text{des},j}}.$$

²In case of a well prepared argon frost layer $\alpha = 0.7$ holds.

- ii) The segments i and j are separated by exactly one beam tube part from the virtual facet H_3 implying:

$$U_{\text{des},j}^{\text{ads},i} = \frac{N_{\text{hit},H_3}}{N_{\text{des},j}} \cdot \left(\frac{N_{\text{ads},i}}{N_{\text{hit},H_3}} \right)_{\text{part } 3} \quad \text{and}$$

$$V_{\text{des},j}^{\text{hit},i} = \frac{N_{\text{hit},H_3}}{N_{\text{des},j}} \cdot \left(\frac{N_{\text{hit},i}}{N_{\text{hit},H_3}} \right)_{\text{part } 3}.$$

- iii) The segments i and j are separated by exactly two beam tube parts with the virtual facets H_3 and H_4 implying:

$$U_{\text{des},j}^{\text{ads},i} = \frac{N_{\text{hit},H_3}}{N_{\text{des},j}} \cdot \left(\frac{N_{\text{hit},H_4}}{N_{\text{hit},H_3}} \right)_{\text{part } 3} \cdot \left(\frac{N_{\text{ads},i}}{N_{\text{hit},H_4}} \right)_{\text{part } 4} \quad \text{and}$$

$$V_{\text{des},j}^{\text{hit},i} = \frac{N_{\text{hit},H_3}}{N_{\text{des},j}} \cdot \left(\frac{N_{\text{hit},H_4}}{N_{\text{hit},H_3}} \right)_{\text{part } 3} \cdot \left(\frac{N_{\text{hit},i}}{N_{\text{hit},H_4}} \right)_{\text{part } 4}.$$

Since another simulation approach, which is described in section 4.3.3 hint to a dominant coverage in the first part of the cold trap³, the concatenation for $j \in [28,102]$ has not been applied.

The coupled differential equations (4.9) can be integrated numerically with discrete time steps Δt using the Euler method. At the starting point $t_0 = 0$, the stable gas injection Φ_{in} into CPS starts at V2, with no particles in other parts of the system ($A_i(0) = 0$). For the first iteration at $t_1 = \Delta t$, the first particles adsorbed on the surface are emitted from V2

$$A_i(t_1) = \Phi_{\text{in}} \cdot \Delta t \cdot U_{\text{des},V_2}^{\text{ads},i}. \quad (4.12)$$

After n steps at $t_n = n \cdot \Delta t$ the number of adsorbed particles on segment $i \in [1,102]$ is

$$A_i(t_n) = A_i(t_{n-1}) + \Phi_{\text{in}} \cdot \Delta t \cdot U_{\text{des},V_2}^{\text{ads},i} + \sum_{j=1}^{102} \left(A_j(t_{n-1}) \frac{\Delta t}{\tau_{\text{des}}} U_{\text{des},j}^{\text{ads},i} \right) - A_i(t_{n-1}) \frac{\Delta t}{\tau_{\text{des}}}. \quad (4.13)$$

The first term is calculated by the iterative approach, starting with equation (4.12). The constant gas inlet through V2 is considered in the second term. The third term takes into account the amount of desorbed gas from segments j which depends on the adsorbed amount of particles $A_j(t_{n-1})$ one time step before, the desorption rate $1/\tau_{\text{des}}$, and the adsorption probability at segment i , $U_{\text{des},j}^{\text{ads},i}$. Finally, the particles desorbed from segment i have to be subtracted.

In order to determine the reduction factor, the outlet flow has to be calculated first by looking at the adsorptions of V4 ($i = 103$)

$$\Phi_{\text{out}} = \frac{A_{103}(t_n) - A_{103}(t_{n-1})}{\Delta t} = \Phi_{\text{in}} \cdot U_{\text{des},V_2}^{\text{ads},103} + \sum_{j=1}^{102} \left(\frac{A_j(t_{n-1})}{\tau_{\text{des}}} U_{\text{des},j}^{\text{ads},103} \right). \quad (4.14)$$

This leads to the reduction factor

$$R(t_n) = \frac{\Phi_{\text{in}}}{\Phi_{\text{out}}} = \frac{\Phi_{\text{in}}}{\Phi_{\text{in}} \cdot U_{\text{des},V_2}^{\text{ads},103} + \sum_{j=1}^{102} \left(\frac{A_j(t_{n-1})}{\tau_{\text{des}}} U_{\text{des},j}^{\text{ads},103} \right)}. \quad (4.15)$$

³Therefore, the desorption of the other parts 2-4 is negligible.

Since we measure the pressure ratio between PP1 and PP2, the simulated reduction factor has to be related to a measured pressure ratio. According to reference [KA14] the partial pressure p_{ij} on surface i caused by continuously desorbing gas from surface j can be derived from

$$p_{ij}(t) = \frac{4 q_j(t)}{\bar{c}} \frac{N_{\text{hit},i}}{F_i} = \frac{4 Q_j(t)}{\bar{c}} \frac{1}{F_i} \cdot V_{\text{des},j}^{\text{hit},i}, \quad (4.16)$$

with the mean thermal velocity \bar{c} , the gas flow into the chamber $q_j(t)$, and the area of the segment F_i . In order to replace $q_j(t)$ with the particle flow $\Phi_j = A_j(t-1)/\tau_{\text{des}}$, it has to be multiplied with the Boltzmann constant k_B and the temperature T . With similar iterative approach as before, the pressure after $t_1 = \Delta t$ is

$$p_i(t_1) = \frac{4 \Phi_{\text{in}} \cdot k_B T}{\bar{c}} \frac{1}{F_i} \cdot V_{\text{des},V2}^{\text{hit},i}, \quad (4.17)$$

For $t_n = n \cdot \Delta t$, the desorptions from the other segments j have to be taken into account

$$\begin{aligned} p_i(t_n) &= p_i(t_1) + \sum_{j=1}^{102} p_{ij} \\ &= p_i(t_1) + \sum_{j=1}^{102} \left(\frac{4 A_j(t_{n-1}) \cdot k_B T}{\bar{c}} \frac{1}{F_i \cdot \tau_{\text{des}}} \cdot V_{\text{des},j}^{\text{hit},i} \right) \\ &= \frac{4 \cdot k_B T}{\bar{c} \cdot F_i} \left(\Phi_{\text{in}} \cdot V_{\text{des},V2}^{\text{hit},i} + \sum_{j=1}^{102} \left(\frac{A_j(t_{n-1})}{\tau_{\text{des}}} \cdot V_{\text{des},j}^{\text{hit},i} \right) \right). \end{aligned} \quad (4.18)$$

With the pressure gauges located at CPS-PP1 ($i = 104$) and CPS-PP2 ($i = 105$) the simulated pressure ratio of these two segments can be calculated

$$\frac{p_{\text{PP1}}(t_n)}{p_{\text{PP2}}(t_n)} = \left(\frac{\Phi_{\text{in}} \cdot V_{\text{des},V2}^{\text{hit},\text{PP1}} + \sum_{j=1}^{102} \frac{A_j(t_{n-1})}{\tau_{\text{des}}} \cdot V_{\text{des},j}^{\text{hit},\text{PP1}}}{\Phi_{\text{in}} \cdot V_{\text{des},V2}^{\text{hit},\text{PP2}} + \sum_{j=1}^{102} \frac{A_j(t_{n-1})}{\tau_{\text{des}}} \cdot V_{\text{des},j}^{\text{hit},\text{PP2}}} \right) \cdot \frac{F_{\text{PP1}}}{F_{\text{PP2}}}. \quad (4.19)$$

With equations (4.15) and (4.19), an ad-hoc factor $k(t_n)$ can be defined allowing the reduction factor to be expressed in dependence of the pressure ratio

$$R(t_n) = k(t_n) \cdot \frac{p_{\text{PP1}}(t_n)}{p_{\text{PP2}}(t_n)}. \quad (4.20)$$

The results of the COMSOL Multiphysics® simulation in section 4.3.1 revealed an inhomogeneous temperature profile of the cold trap. Thus their influence on the mean sojourn time τ_{des} has to be taken into account. For calculating the effective mean value, τ_{des} is weighted with the area A_i of a segment i at the corresponding temperature T_i resulting in

$$\begin{aligned} \bar{\tau}_{\text{des}} &= \frac{\sum_{i=1}^n \tau_0 \cdot \exp\left(\frac{E_{\text{des}}}{RT_i}\right) A_i}{\sum_{i=1}^n A_i} \\ &= \begin{cases} 5.4 \times 10^6 \text{ s} \approx 62.5 \text{ d} & \text{for } E_{\text{des}} = 1200 \text{ J mol}^{-1} \\ 1.5 \times 10^{10} \text{ s} \approx 475.3 \text{ a} & \text{for } E_{\text{des}} = 1400 \text{ J mol}^{-1} \\ 4.1 \times 10^{13} \text{ s} \approx 1.3 \times 10^6 \text{ a} & \text{for } E_{\text{des}} = 1600 \text{ J mol}^{-1} \end{cases} \end{aligned} \quad (4.21)$$

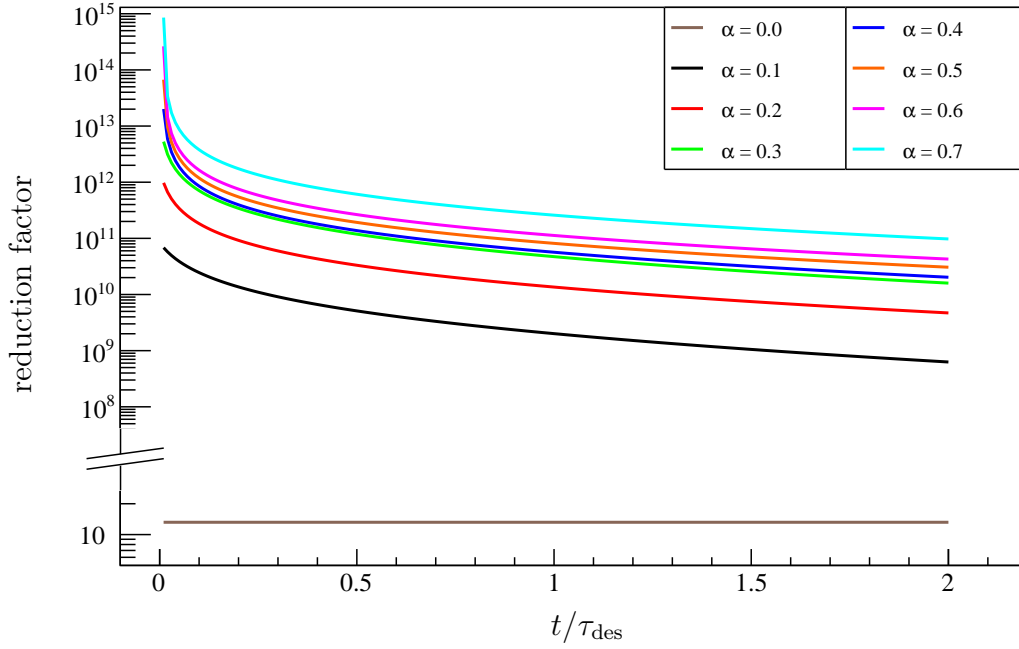


Figure 4.6.: Simulated CPS reduction factor with MolFlow+. The temporal development of the different reduction factors are shown versus the normalized time for various sticking factor α . Here the nominal KATRIN settings were used with valves V2 and V4 open [FRS⁺19].

Because there is no literature value for the desorption energy E_{des} of tritium on an argon layer, three fixed values from 1200 J mol^{-1} to 1600 J mol^{-1} are analyzed based on estimations given in reference [LD08] (lower boundary), as well as measurement results discussed in section 5.1.2.5. Since the valves V2 and V4 were closed during the commissioning measurements, additional simulations were performed for this changed conditions, which are used for the calculation of the ad-hoc factor.

The results of the simulations are shown in figures 4.6 - 4.8. With the unknown desorption energy, the time on the x-axis was normalized to the mean sojourn time. For the iterative approach, time steps of $\Delta t = 0.01 \cdot \tau_{\text{des}}$ were used over a time interval from $t = 0$ to $2 \cdot \tau_{\text{des}}$. As expected, a larger sticking coefficient α leads to a larger reduction factor (figure 4.6), as well as a larger pressure ratio (figure 4.7). This can be explained by the higher number of adsorptions/desorptions a particle has to endure for an increasing α when traveling through the CPS cold trap. For $\alpha = 0$ (corresponding to no cryosorption at all) the reduction factor $R \approx 10$ is independent of the mean sojourn time. In this case the value, which is larger than 1, is defined by the ratio of the conductance of the CPS beam tube and the last DPS beam tube section. In general the pressure ratios plotted in figure 4.7 follow the trends of the reduction factor values. The small deviations, which can be seen in figure 4.8 possibly originate from the different settings of opened (nominal KATRIN setting for reduction factor) and closed (commissioning setting for pressure ratios) valves V2 and V4. Ignoring $\alpha = 0$, the simulated ad-hoc factors lie between 8.5 and 21. For a sticking coefficient of $\alpha = 0.7$ an ad-hoc factor average of

$$k_{\alpha=0.7} \approx 18 \pm 10\% \quad (4.22)$$

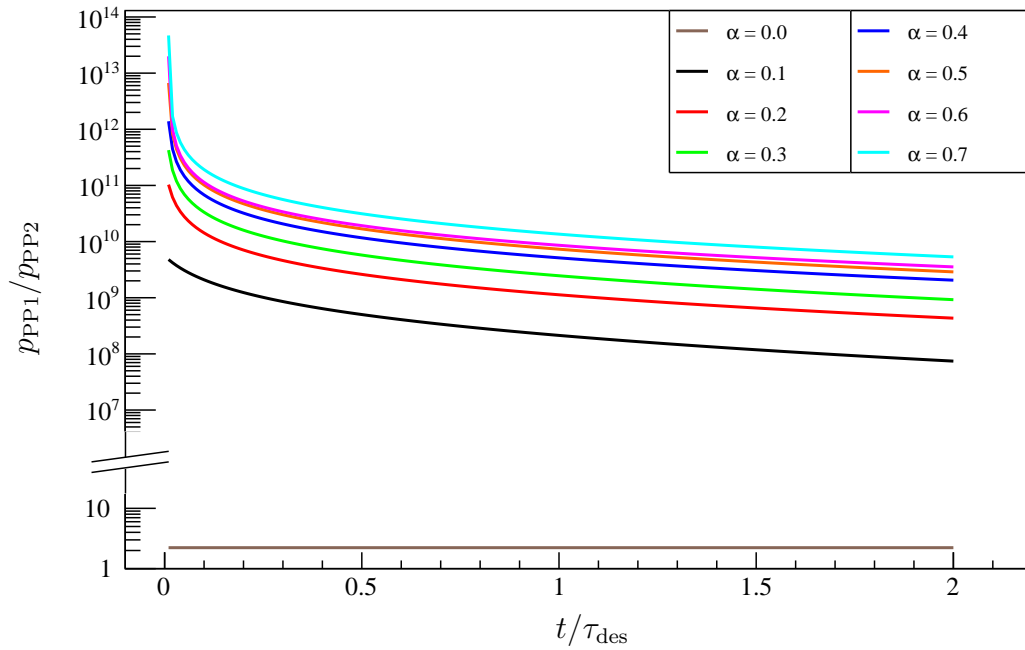


Figure 4.7.: Simulated CPS pump port pressure ratio with MolFlow+. The temporal development of the pressure ratios for the commissioning setting (V2 and V4 closed) are shown for various sticking factors α .

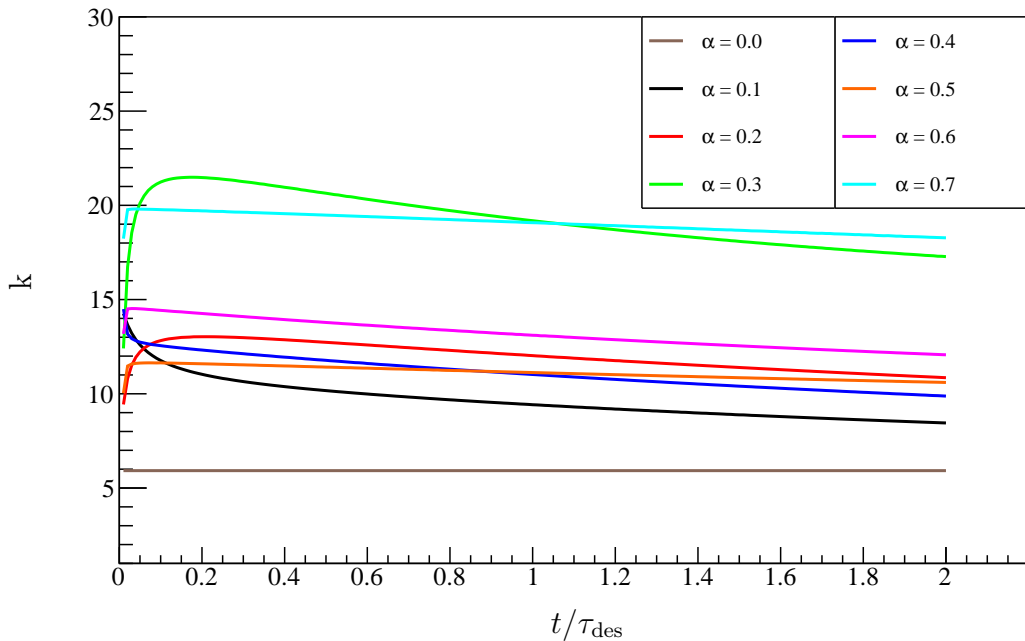


Figure 4.8.: Simulated CPS ad-hoc factors with MolFlow+. The ad-hoc factors $k(t)$ to 0.7 are plotted over the normalized time for different sticking factors $\alpha = 0$. The results of figures 4.6 and 4.7 were used to determine the ad-hoc factors [FRS⁺19].

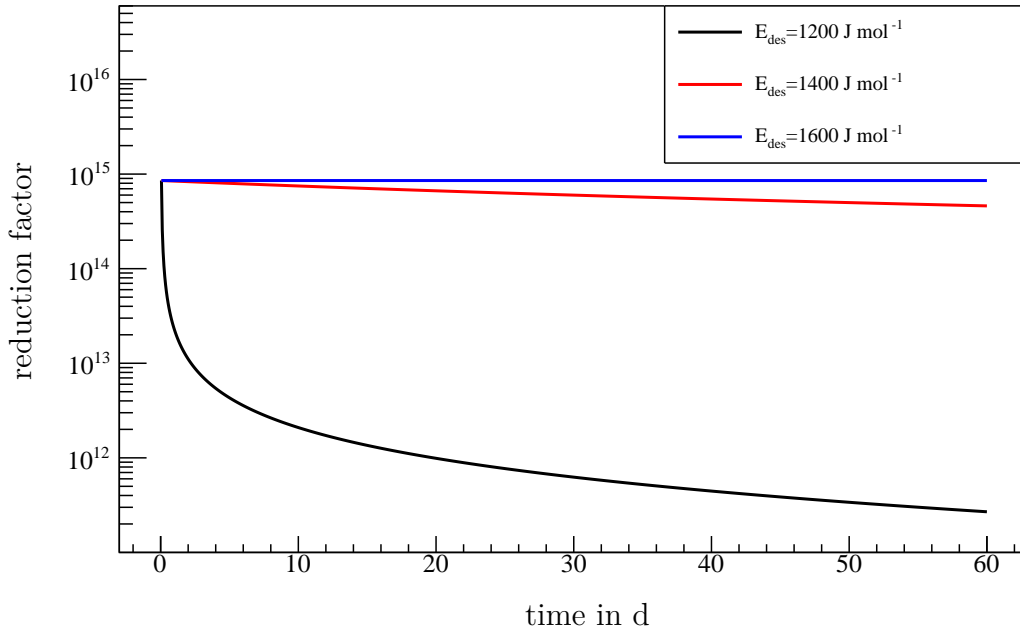


Figure 4.9.: Simulated CPS reduction factor for different desorption energies with MolFlow+. The CPS reduction factor trend is shown within the nominal 60 d CPS argon frost layer operation for three different desorption energies. A sticking factor of $\alpha = 0.7$ is used [FRS⁺19].

can be derived, which will be used in section 5.1.2.5. For the uncertainty a value of 10% is estimated defining the variation over the normalized time.

In order to estimate the cold trap performance within a nominal 60 d run, specific values for the desorption energy have to be chosen to calculate τ_{des} , which allows us to multiply the relative time of the x-axis with a fixed mean sojourn time. In figure 4.9, the reduction factor is shown for the three different E_{des} used in equation 4.21 with a sticking coefficient of $\alpha = 0.7$. Even for the most conservative approach of $E_{\text{des}} = 1200 \text{ J mol}^{-1}$, the simulation results in a reduction factor of more than 10^{11} , which is four orders of magnitude larger than the requirement.

Nevertheless, there are some simplifications, which were used for the simulation. The large number of adsorptions of a particle on its way through the cold trap allows using an averaged mean sojourn time for all segments. Since in MolFlow+ each particle track is computed independently from the others, a possible change of the sticking factor due to fully covered cold trap segments cannot be taken into account. Based on the result in reference [Jan15], the first 1.7%⁴ of the cold trap is supposed to be covered to 100%, while the coverage in rest of the cold trap can be neglected. The change of the sticking coefficient for a partly covered surface is given by

$$\alpha(\theta) = \alpha_0 \cdot (1 - \theta) , \quad (4.23)$$

with the coverage θ . Therefore, a fully covered surface will result in a sticking coefficient $\alpha = 0$, which will have an impact on the reduction factor. Assuming an

⁴Beginning from the start of the cold trap at beam tube section 2.

exponential drop of the reduction factor along the beam tube results in a decrease of the simulated value by 36%.

Another source of uncertainty is the concatenation of the CPS beam tube geometry. An estimation of the influence can be made by comparing the simulation results for a sticking factor of $\alpha = 0.1$ with concatenation and after a single-pass simulation. The lowest sticking coefficient was chosen since particles have a higher probability to migrate through the whole CPS with fewer simulation steps for a single pass run. By this approach a factor of two can be estimated for the uncertainty induced by the concatenation.

The largest uncertainty for the central value of the reduction factor arises from the unknown desorption energy. Since commissioning measurements discussed in section 5.1.2.5 favor a desorption energy significantly larger than $E_{\text{des}} = 1200 \text{ J mol}^{-1}$, the corresponding reduction factor can be assumed to be a conservative lower limit.

In contrast to deuterium commissioning measurements, the desorptions induced by radioactive decays have to be taken into account for tritium operation. This will reduce the reduction factor further and is covered in section 4.3.3. In conclusion, the MolFlow+ simulations enable us to convert CPS commissioning results into a reduction factor by applying the calculated ad-hoc factor $k(t)$. Due to the described uncertainties, the simulated reduction factor value can only be stated in an order of magnitude range. However, even with this large uncertainty the simulated value is larger than the stringent requirement CPS reduction factor.

4.3.3. Semi-analytical tracking model

In another approach, a second simulation model was developed, which can implement the temperature inhomogeneities, as well as desorptions induced by β -decays. Therefore, a custom made C++ semi-analytical tracking model was developed. In order to determine the interaction points for a particle hitting the inner beam tube, the same geometry as for MolFlow+ simulations (see figure 4.5) was implemented by splitting it into basic shapes, such as cylinders, cones, and cuboids. This allows to analytically calculate the particle's trajectory and to simulate all the possible interactions, such as adsorptions, and thermal desorptions with respect to the temperature and the surface density, and β -induced desorptions. This way, it is possible to integrate a detailed temperature profile, which is important to validate simulation results, since there are regions where particles are more likely to be adsorbed than in others. An average temperature (weighted by the surface only), as in the MolFlow+ simulations, cannot take this effect into account. With the implementation of more than 12000 equally distributed temperature values from the COMSOL Multiphysics[®] simulation this effect can be considered. For all simulations, a sticking coefficient $\alpha = 0.7$ was used for the cold trap. For the calculation of the desorption time equation (3.13) was used, while the direction of particles desorbing from the cold trap surface was simulated by a cosine law sampling [Gre02]. When calculating τ_{eff} , a specific value for the desorption energy E_{des} had to be chosen. Therefore, a new simulation was started for each value of E_{des} .

For the reduction factor calculation, the time for a particle leaving the CPS into the pre-spectrometer is simulated. As particles will not always enter the pre-

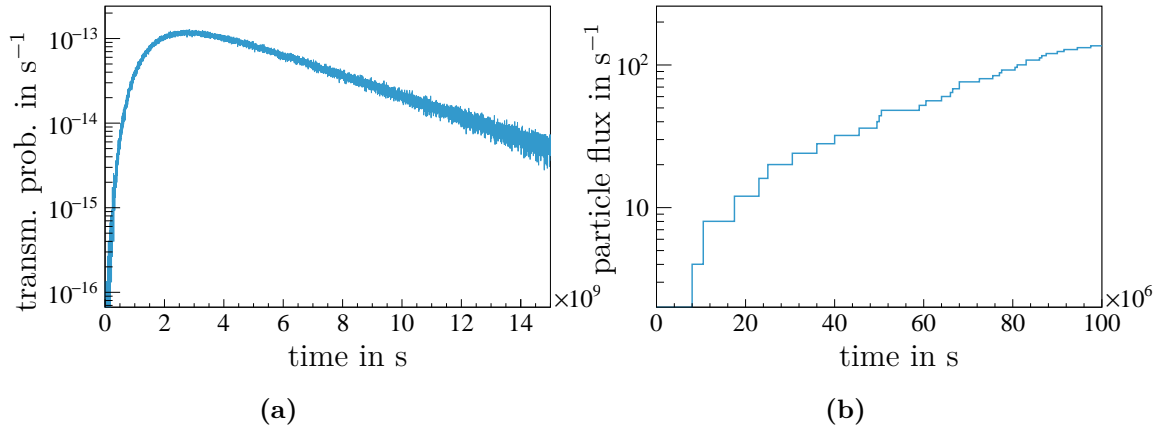


Figure 4.10.: Histograms for semi-analytical tracking method. (a) Transmission probability function for the whole simulation time. A desorption energy of 1200 J mol^{-1} and pure tritium ($\sigma = 2$) were used for this distribution; (b) particle flux for the first 1150 d [FRS⁺19].

spectrometer, there are two cases, in which a particle is only accounted in the incoming flow:

- i) The maximal integration time is reached before hitting V4.
- ii) A reflection into DPS-PP4 occurs, where it is assumed to be pumped away.

Since the number of particles reaching V4 within the nominal operation time of 60 d is small, a very high number of simulations (up to 2.5×10^{11}) has to be made. After the simulations were finished all migration times were filled in a histogram. Normalizing the histogram to the total number of simulated particles results in a probability density distribution $m(t)$ for reaching the pre-spectrometer after a time t , which depends on the temperature, desorption energy, sticking probability, and tritium purity. Integrating $m(t)$ over a specific time t and multiplying the result with the incoming flux $\Phi_{\text{in}} = 10^{12} \text{ molecules/s}$ into the CPS [Jan15] yields the outgoing flux into the pre-spectrometer

$$\Phi_{\text{out}}(t) = \Phi_{\text{in}} \int_0^t m(t') dt' . \quad (4.24)$$

As the reduction factor $R(t)$ is defined by the ratio of the incoming flux and the outgoing flux, it follows

$$R(t) = \frac{\Phi_{\text{in}}}{\Phi_{\text{out}}(t)} = \left(\int_0^t m(t') dt' \right)^{-1} . \quad (4.25)$$

In figure 4.10(a) $m(t)$ is shown for a desorption energy of 1200 J mol^{-1} . The resulting outgoing flux obtained via integration of the probability density distribution is plotted in figure 4.10(b) for the first 1200 d. Due to the low number of events within the first 60 d, a linear curve was fitted between the origin ($t = 0 \text{ d}$) and the first non-zero bin.

In order to consider the effect of $\eta(s)$ on τ_{eff} (see equation (3.11)), the surface density s along the cold trap was investigated. The resulting surface density is shown in figure 4.11. The influence of the temperature distribution can be seen since the

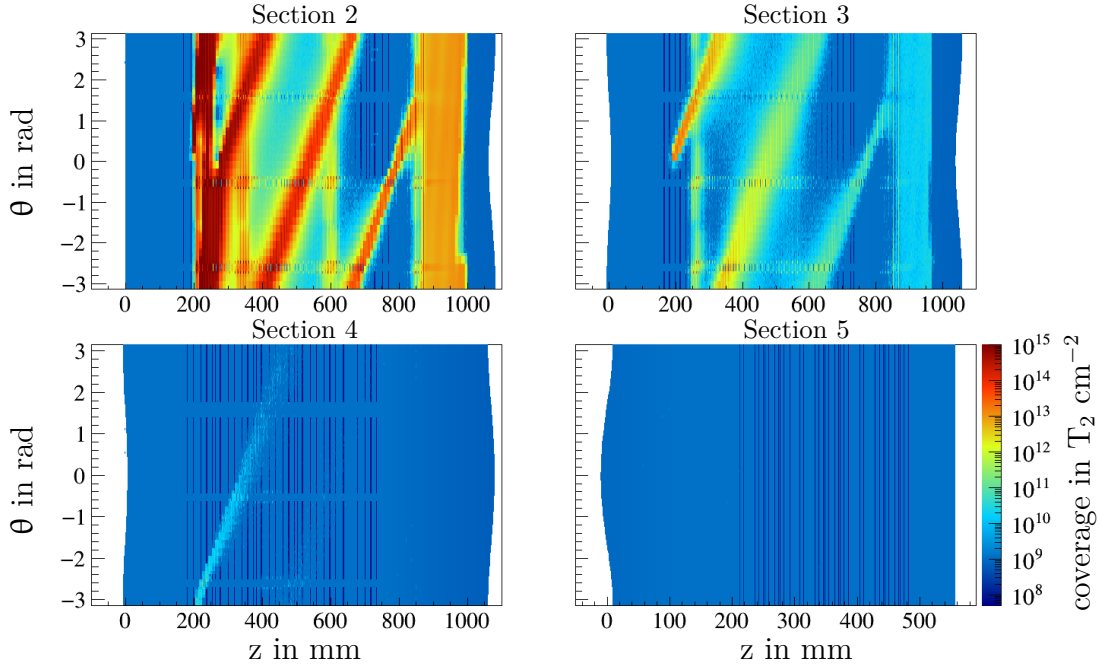


Figure 4.11.: Simulated cold trap coverage. The tritium coverage is plotted in a 2D histogram along the central beam tube axis after a nominal 60 d run. Θ is defined as the azimuthal angle along the cold trap. The coverage follows the simulated temperature profile in section 4.3.1 [FRS⁺19].

parts covered most are the ones where the temperature is at 3 K close to the cooling loop. Due to the higher mean sojourn time τ_{des} at a lower temperature, this behavior was expected. The mean surface density

$$\bar{s} = \frac{\sum_i s_i \cdot n_i}{n_{\text{tot}}} \quad (4.26)$$

plotted in figure 4.12 confirms the visible trend of a decreasing coverage over the length of the cold trap. s_i is the surface density of bin i with n_i molecules. Except for the last point in beam tube section 5, the trend can be approximated by an exponential decrease from a coverage of about $10^{15} T_2 \text{ cm}^{-2}$ down to $10^9 T_2 \text{ cm}^{-2}$. A known \bar{s} allows a bin-wise calculation of the effective desorption time.

In contrast to the MolFlow+ simulations in section 4.3.2, a reduction factor for $E_{\text{des}} = 1400 \text{ J mol}^{-1}$ and 1600 J mol^{-1} cannot be calculated for non-radioactive hydrogen isotopologues since with the number of simulated particles there are no events in the first 60 d bin. Therefore, the uncertainty in case of an extrapolation would be too high.

However, it is possible to include the radioactive desorption, which reduces the reduction factor and allows an analysis for desorption energies above 1200 J mol^{-1} . The results are shown in figure 4.13, in which for all three desorption energies simulation for the three tritium isotopologues (HT, DT, and T_2) were performed. Similar to figure 4.6, the reduction factor decreases over time. As expected, an injection of pure T_2 leads to the worst reduction factor, which is still larger than 10^{10} in the most conservative approach exceeding the required 10^7 . With the introduction of

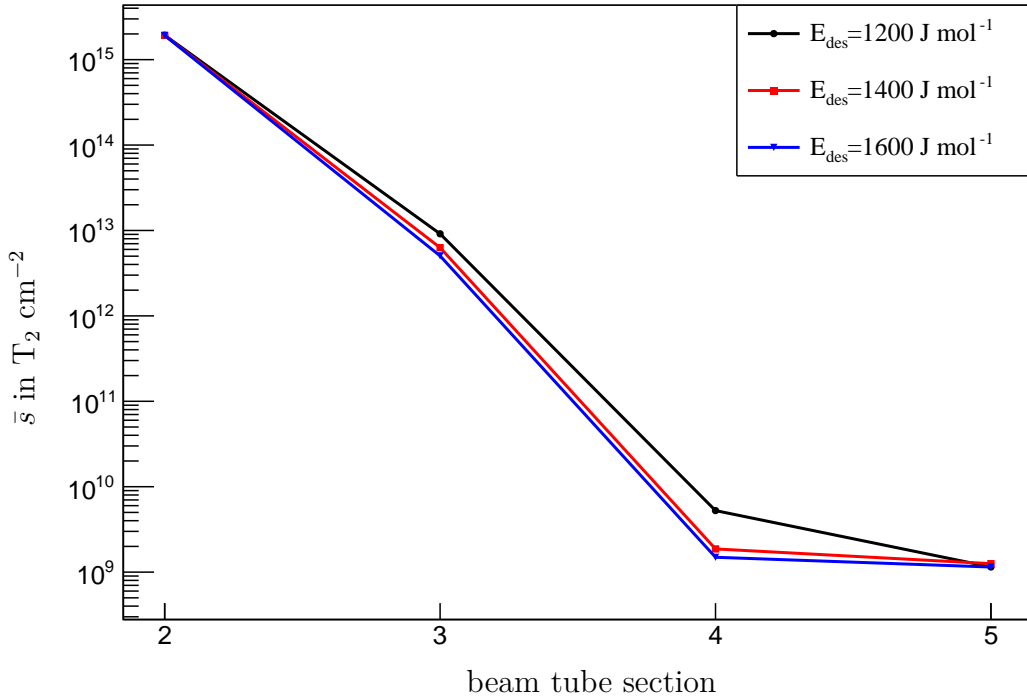


Figure 4.12.: Mean surface density of CPS cold trap. The mean surface density \bar{s} is shown for each beam tube part of the cryo pump. As the number of molecules reaching beam tube 5 was too low, an upper limit has been given [FRS⁺19].

the radioactive decay, the variation of the reduction factor for desorption energies between $E_{\text{des}} = 1200 \text{ J mol}^{-1}$ and 1600 J mol^{-1} is smaller than a factor of 100 compared to almost four orders of magnitude in figure 4.9. The simulated values for all scenarios are given in table 4.3.

As a simplification a static surface density after 60 d was used for the calculation of the effective desorption time τ_{eff} . The result was obtained from a simulation with a non-radioactive adsorbate and its corresponding desorption energy between $E_{\text{des}} = 1200 \text{ J mol}^{-1}$ and 1600 J mol^{-1} . An averaged surface density per section can be used as the effect of a radioactive decay for τ_{eff} is only important for the parts with a high amount of adsorbates. Since this approach overestimates the amount of adsorbed tritium, the reduction factor results are a lower limit.

The largest uncertainty originates from the linear extrapolation for the first 60 d due

Table 4.3.: CPS reduction factors for different isotopologues. The different simulated reduction factors after 60 days are listed for different desorption energies and isotopologues. The star corresponds to values above 2.5×10^{11} , which were interpolated linearly between zero molecules at the beginning and the shortest time.

E_{des} in J mol^{-1}	H_2/D_2	HT/DT	T_2
1200	$4.0 \times 10^{11*}$	2.1×10^{11}	7.7×10^{10}
1400	–	$9.6 \times 10^{11*}$	$4.3 \times 10^{11*}$
1600	–	$1.8 \times 10^{12*}$	$1.2 \times 10^{12*}$

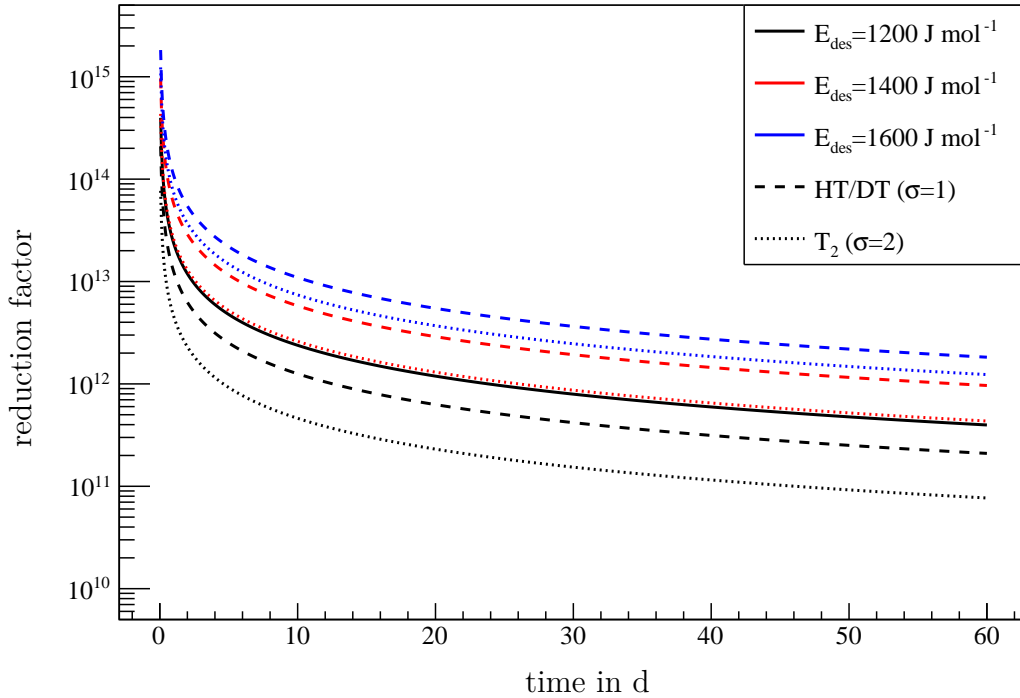


Figure 4.13.: Simulated CPS reduction factor with tritium β -decay. The reduction factor for different adsorbates are plotted versus the time for the first 60 d. The different colors indicate the desorption energy, while the solid (non-radioactive case), dashed, and dotted lines are for distinction of the different hydrogen isotopologues [FRS⁺19].

to the low amount of entries in the probability density distribution $m(t)$. Therefore, a reduction factor larger than 2.5×10^{11} is only a lower limit.

Additionally, the result can be compared with the MolFlow+ simulation for a desorption energy of 1200 J mol^{-1} , which is shown in figure 4.14. With a difference smaller than a factor 2, the results are in good agreement considering all the uncertainties, which are in the order of magnitude range.

4.4. Summary

In this chapter simulations for the gas reduction factors of the differential and cryogenic pumping sections were performed. First, a MolFlow+ simulation for the DPS was executed, in which the geometry was split into four parts. Taking the high uncertainty for the TMP pumping speed into account, the simulated reduction factor meets the required 10^5 . Additionally, a simulation for deuterium was made in order to compare the simulation with commissioning measurements. Therefore two ad-hoc factors were calculated allowing to convert a measured pressure ratio into a reduction factor.

For the simulation of the CPS not only cryo-pumping has to be considered but also thermal desorption of particles adsorbed on the cold trap. With the implementation of 102 segments, an adsorption and hit matrix was calculated for each segment. Similar to the DPS simulation, the beam tube geometry was subdivided into four parts for the concatenation of partial simulations. The simulations were repeated

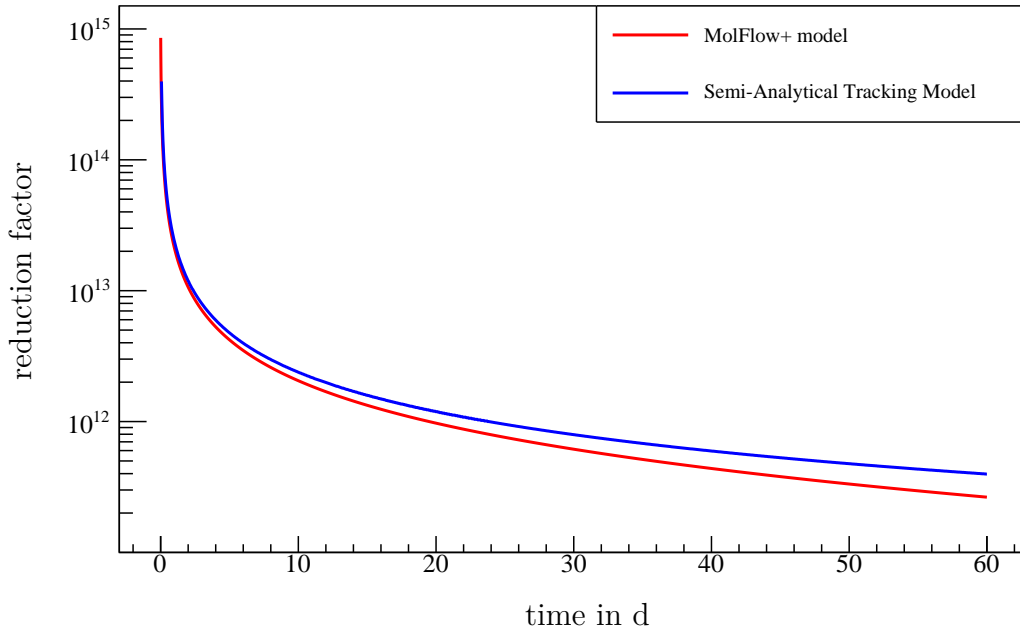


Figure 4.14.: Comparison of MolFlow+ and semi-analytical tracking model.

The reduction factor is plotted over the 60 d of nominal operation. Both results agree within a factor of two for $\alpha = 0.7$ and $E_{\text{des}} = 1200 \text{ J mol}^{-1}$.

for different sticking factors in the range of $\alpha = 0.0 \dots 0.7$ in steps of 0.1. The results were given for a relative time scale normalized to the mean sojourn time. As the temperature is an important parameter for the calculation of τ_{des} , a dedicated COMSOL Multiphysics[®] simulation was performed, investigating the cold trap temperature distribution. Since there are no literature values for the desorption energy, three values were used to estimate the reduction factor with the lowest one as a conservative limit. The results showed that the reduction factor is larger than 10^{11} for the lowest desorption energy. Furthermore, ad-hoc factors were determined, which are used in section 5.1.2.5 for calculating the reduction factor from the measured pressure ratio.

In another approach, a semi-analytical tracking model was constructed in order to include the effects of desorption induced by β -decays, as well as the temperature distribution of the cold trap. With this method the surface density of adsorbed tritium was determined. A reduction factor was calculated for the three different desorption energies as a function of time. As a crosscheck the results were compared with the MolFlow+ simulation. The agreement within a factor of two is good, considering the uncertainty to be in the order of magnitude range. Even with the inclusion of the β -decay, the CPS reduction factor is more than three orders of magnitude larger than the requirement.

The results of this chapter were published in [FRS⁺19].

5. Measurements of the gas flow reduction factor

The sensitivity of KATRIN for the effective neutrino mass depends on the background rate superimposed on the measured tritium β -decay spectrum. A process that would result in an elevated background rate is the contamination of the spectrometer section with tritium due to an ineffective tritium retention system. Therefore, test measurements with deuterium were performed for the DPS and CPS as part of the STS IIIa campaign to compare the measured gas flow reduction factor of the source and transport section (STS) to the simulation from chapter 4 before operation with tritium. These demanding measurements due to the large expected reduction factors of more than eight magnitudes of order are described and analyzed in section 5.1. The positive results of achieved retentions larger than seven orders of magnitude with D_2 were mandatory to start operations of KATRIN with tritium. A major milestone for the KATRIN experiment was then the First Tritium campaign. Its results with respect to the reduction factor and thereby the background rate are analyzed and presented in section 5.2.

5.1. Measurements with deuterium

In order to avoid a possible radioactive contamination of the flux tube volume or spectrometer surfaces with tritium, first tests of the gas flow reduction factor of the STS components were performed with deuterium. As the physical properties of deuterium are close to the ones of tritium, the results for the reduction factor should be an excellent indicator for the real measurement situation. Already in smaller scaled precursor experiments [Eic09] no differences in adsorption properties were observed. Concerning the DPS, the deuterium pumping speed of the turbomolecular pump (TMP) *Leybold MAGW 2800* is lower than for tritium leading to a lower reduction factor for deuterium operation. The difference is due to the lower atomic mass and can be corrected reliably for T_2 -operation. In case of the CPS, the most important difference between deuterium and tritium is the radioactivity, which plays only a major role for reduction factors larger than 10^{11} (see section 4.3). Despite these expected differences, the deuterium studies play a major role in the commissioning

of the STS components as they provide a first test of the DPS and CPS working principle.

In both pumping sections of the source and transport section the tritium flow is in the molecular flow range. This has to be taken into account for the test measurement set-ups and execution. The DPS measurements were performed with the nominal KATRIN set-up, where deuterium is injected via the inner loop system. Based on the pressure ratios at the DPS pump ports, the reduction factor of the DPS is analyzed in section 5.1.1. Simulation results predict a reduction factor for the CPS larger than 10^{10} , which proves a challenge for the measurement instrumentation to cover the large range. Therefore, two different methods will be used for the investigation of the reduction factor. Additional to the nominal deuterium injection via the inner loop system, a dedicated inlet system was installed between DPS and CPS. This allows a larger injection flow of deuterium, resulting in a better sensitivity for the estimation of the reduction factor as well as shorter measurement times. The set-up of this inlet system together with its properties is described in section 5.1.2.1.

The reduction factor measurements of the CPS were performed for different temperatures of the cryo pump. In the following, the labelling ‘3 K’ and ‘4.5 K’ cooling of the CPS refers to the nominal throughput temperature of the cold trap piping. As described in section 4.3.1, this is not equivalent to the temperature in the whole cold trap due to the inhomogeneous temperature distribution. Wherever a reference temperature for the cold trap is given, this will be data of the temperature sensor *RTY-3-3101* (located in beam tube section 3, see figure E.3), as it is the sensor with the smallest discrepancy between beam tube and throughput temperature (compare figure 4.2).

5.1.1. Reduction factor of the differential pumping section

The differential pumping section is the first part of the transport and pumping section. Besides the ion retention through beam tube electrodes, six TMPs are installed at five pump ports, two of which are situated at PP0. As the outlet of each TMP is connected to the outer loop, the DPS can not be operated independently. Additionally, the DPS reduction is linked to the WGTS: Six TMPs are installed to the front side of the WGTS as a first reduction stage of the tritium flow. It is therefore difficult to state a standalone DPS reduction factor.

In contrast to the CPS, the reduction factor of the DPS is highly gas species dependent. Operation with deuterium strongly influences the performance of the TMPs because the sticking coefficient is proportional to the molar mass (see section 4.2). Accordingly, the reduction factor of the DPS for deuterium operation is expected to be smaller than for tritium operation. The reduction factor is determined through the ratio of the pressure sensors located at the DPS pump ports. Due to an enhanced outgassing of some parts of the FT-ICR in the last beam tube element between PP4 and PP5, the pressure at PP4 (location of the last DPS TMP) may not be used for the reduction factor calculation.

Because of time constraints, measurements with open valves V1 and V2 could be performed for about 1.5 h. V1 controls the gas flow between WGTS and DPS, while

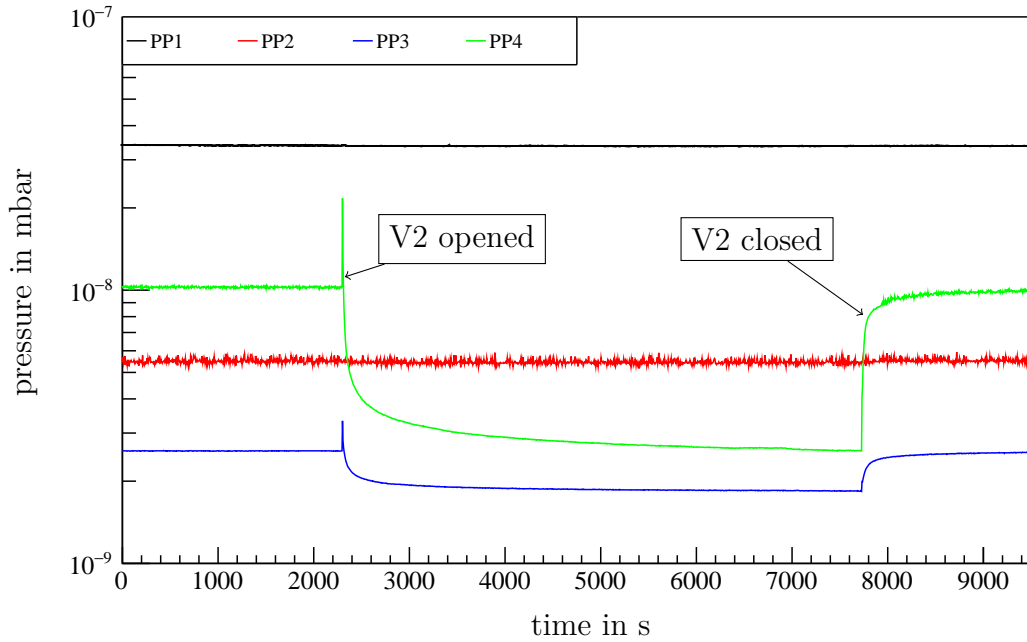


Figure 5.1.: DPS reduction factor measurement. The plot shows the pressure at DPS pump ports 1-4. The timespan with open valve V2 ranges from 2400 s to 7800 s, spanning 1.5 h.

V2 is located between DPS and CPS. During the measurement the magnets of the STS section were shut down¹ and the CPS cold trap was at 4.5 K.

In figure 5.1 the pressures at the DPS pump ports 1-4 show the effect of opening valve V2. Several insights can be gained from this plot:

- i) The pressure at PP4 is higher than the one at PP3. This is caused by the outgassing of the FT-ICR. Normally it is expected that the pressure will decrease from PP1 to PP4.
- ii) When opening V2, the pressure at PP3 and PP4 rises. This is caused by residual gas, originating from small cavities within the valve.
- iii) The pressure at PP1 and PP2 is stable over the whole time range and therefore not affected by the CPS cryo trap.
- iv) After opening V2, the pressures at PP3 and PP4 take time to stabilize. As V2 controls the gas flow between DPS and CPS, a new pressure equilibrium with open V2 is defined by the CPS cold trap. In contrast to PP3, the pressure at PP4 does not reach its equilibrium within 1.5 h. As the high PP4 pressure is mainly caused by the FT-ICR outgassing, the PP4 pressure is not used for the reduction factor estimation.
- v) After V2 is closed again, the pressures at PP3 and PP4 reach their values before opening.

¹The pressure read-out should be independent of magnetic fields because they are equipped with passive shielding against it.

With the simulated ad hoc factors $k_{\text{PP1/PP2,D}_2} = 9500 \pm 3000$ and $k_{\text{PP1/PP3,D}_2} = 200 \pm 80$, and the measured pressures of PP1/2/3, the reduction factor can be estimated.

The reduction factor obtained from the pressure ratio between PP1 and PP2 is given by

$$\begin{aligned} R_{\text{PP1/PP2,com}} &= k_{\text{PP1/PP2,D}_2} \cdot \frac{p_{\text{PP1,com}}}{p_{\text{PP2,com}}} \\ &= k_{\text{PP1/PP2,D}_2} \cdot \frac{3.37 \times 10^{-8} \text{ mbar}}{5.47 \times 10^{-9} \text{ mbar}} = (5.8 \pm 2.1) \times 10^4 . \end{aligned} \quad (5.1)$$

The uncertainty for the pressure is given by the accuracy of the cold cathodes of 10% [MIa].

For the second pressure ratio the following relation applies

$$\begin{aligned} R_{\text{PP1/PP3,com}} &= k_{\text{PP1/PP3,D}_2} \cdot \frac{p_{\text{PP1,com}}}{p_{\text{PP3,com}}} \\ &= k_{\text{PP1/PP3,D}_2} \cdot \frac{3.37 \times 10^{-8} \text{ mbar}}{1.84 \times 10^{-9} \text{ mbar}} = (3.6 \pm 1.6) \times 10^3 . \end{aligned} \quad (5.2)$$

Compared to the simulated reduction factor of $(8.20 \pm 0.03) \times 10^4$, the measured value of $R_{\text{PP1/PP2,com}}$ is close in consideration of the systematic uncertainties. However, the calculation with PP3 results in an order of magnitude lower reduction factor. Possible explanations will be discussed at the end of this section.

A second measurement during the commissioning phase was executed five days later. Due to the continuous pumping of the TMPs the pressure values in all pump ports were smaller compared to the first measurement.

Another possibility to estimate the DPS reduction factor was given by the First Tritium campaign (for details see section 5.2.1). During the two weeks of the FT campaign, trace amounts of tritium were injected into the WGTS with deuterium as carrier gas. As V2 was open all the time, this campaign enables estimation of the DPS reduction factor over two weeks. With these pressures follows

$$\begin{aligned} R_{\text{PP1/PP2,FT}} &= k_{\text{PP1/PP2,D}_2} \cdot \frac{p_{\text{PP1,FT}}}{p_{\text{PP2,FT}}} \\ &= k_{\text{PP1/PP2,D}_2} \cdot \frac{2.69 \times 10^{-8} \text{ mbar}}{4.09 \times 10^{-9} \text{ mbar}} = (6.2 \pm 2.2) \times 10^4 , \end{aligned} \quad (5.3)$$

$$\begin{aligned} R_{\text{PP1/PP3,FT}} &= k_{\text{PP1/PP3,D}_2} \cdot \frac{p_{\text{PP1,FT}}}{p_{\text{PP3,FT}}} \\ &= k_{\text{PP1/PP3,D}_2} \cdot \frac{2.69 \times 10^{-8} \text{ mbar}}{1.00 \times 10^{-9} \text{ mbar}} = (5.3 \pm 1.3) \times 10^3 . \end{aligned} \quad (5.4)$$

Similar to the STS-IIIa campaign, the first ratio is more than one order of magnitude larger compared to the second one. $R_{\text{PP1/PP2,FT}}$ is closer to the simulated value than $R_{\text{PP1/PP2,com}}$, which shows that during the commissioning phase the equilibrium pressures were not reached. As the set-up was the same for the STS-IIIa and FT campaign, the large systematic uncertainties can not be decreased. One of the

systematic effects is the possible change of the hydrogen isotopologue composition as the gas flows through the DPS beamline. This is caused by gas molecules scattering off the beam tube surface or other gas molecules. As the cold cathode output depends on the dominant gas, the read-out pressure does not represent the actual pressure. Measured cold cathode values are calibrated on nitrogen as the dominant gas component. With deuterium as dominant gas species the read-out value has to be divided by 0.35 (hydrogen 0.46)². Because deuterium atoms in a molecule will mainly transform into hydrogen atoms, the actual pressure ratios will become larger since the pressure in PP1 is larger than the one in subsequent pump ports. This would be a possible explanation for the discrepancy between simulation and experiment. Not only the pressure reading is influenced by this effect but also the pumping speed of the TMPs. With these (mentioned) systematic effects, the result of the pressure ratio between PP1 and PP2 seems more reliable.

Other systematic uncertainties originate from backscattering of gas molecules off the TMP and possible outgassing from the beam tube surface. The DPS is at room temperature without the possibility to bake out the beam tube. Therefore, the water in the laboratory air, which has entered the beam tube during the installation, may still reside on the inner surface.

Another uncertainty of the reduction factor measurement described here is that the cold cathodes were not calibrated against each other, resulting in the large uncertainty of 10% for each sensor.

For a better sensitivity of a reduction factor measurement a dedicated deuterium inlet system would be needed. In this case a higher injection flow rate and thereby higher pressures³ would be possible. With this set-up the *MKS 626B Baratron*[®] absolute capacitance manometers at PP1 and PP2 could be used, which have a smaller uncertainty than the cold cathode pressure gauges.

As changes of the hardware set-up would have an impact on the pumping performance itself, possibilities are limited. Since the results of the CPS commissioning measurements described in the following show larger reduction factors than the requirement, no further measurements are considered.

With a different approach, presented in section 5.2.2, a combined reduction factor for the WGTS and DPS can be estimated and the compliance with the requirement can be demonstrated. With the DPS part of the KATRIN pumping section showed satisfying reduction factor results, the following part discusses the reduction factor measurements of the CPS.

5.1.2. Reduction factor of the cryogenic pumping section

The CPS represents the second part of the KATRIN pumping section. As during standard operation a tritium flow of about 10^{-7} mbar ℓs^{-1} reaches the CPS, the pressure inside the CPS is magnitudes smaller than 10^{-9} mbar. For commissioning measurements aimed to determine the reduction factor of the CPS with the nominal set-up, those pressures are below the sensitivity of the installed pressure gauges.

²See <https://www.mksinst.com/n/gas-correction-factors-for-ionization-vacuum-gauges> (accessed on Mar 21, 2019)

³The only constraint is to stay in the molecular flow range.

In order to overcome this experimental challenge, a dedicated deuterium inlet system was installed, allowing to have a higher pressure at PP1 and thereby a higher pressure ratio while keeping molecular flow conditions. The experimental set-up of this system together with the proper and accurate calibration of the devices are described in section 5.1.2.1. After a test of the inlet system with helium in section 5.1.2.2, a first reduction factor measurement with deuterium is described with the same experimental setup in section 5.1.2.4.1. The measurement results with and without an argon frost layer on the cold trap are presented in sections 5.1.2.4 and 5.1.2.5. Finally, the temperature dependency of the cold trap is investigated in section 5.1.2.5.3.

5.1.2.1. Deuterium inlet system

In order to measure the reduction factor of the CPS an inlet system was installed at DPS PP5 to increase the deuterium injection flow into the CPS. Figure 5.2(a) shows the P&I diagram of the realized setting. The injection flow can be regulated by a leak valve (*nenion standard leak valve* [vl16]) in front of a pressure control unit (PIR-3). By multiplying the pressure with the calibrated conductance of the orifice with a diameter of 0.5 mm the injection flow is defined by

$$q_{\text{in}} = p_{\text{in}} \cdot C_{\text{orifice}, \text{D}_2} , \quad (5.5)$$

where p_{in} is the recorded pressure (installed gauge: *MKS Baratron 690A 1 Torr*), and $C_{\text{orifice}, \text{D}_2} = (4.893 \pm 0.029) \times 10^{-2} \ell \text{ s}^{-1}$ the conductance of the orifice for deuterium (calibrated by an independent measurement [Fri17]). With this setup an injection flow between 10^{-5} and $10^{-3} \text{ mbar } \ell \text{ s}^{-1}$ can be achieved. In order to evacuate the inlet system a combination of a scroll pump and a turbo molecular pump is connected to the 15.86ℓ buffer vessel, which serves as a deuterium reservoir during measurements. VMO-9 and VMO-10 provide a bypass, which is useful for evacuating the corrugated tubes that connect the orifice to DPS PP5. As the pipes directly connected to the buffer vessel have an inner diameter of 4 mm, the effective pumping speed of the TMP is strongly reduced when not using the bypass. The buffer vessel is filled via a manual valve (VMO-4) or a flow controller.

5.1.2.1.1. Determination of buffer vessel volume

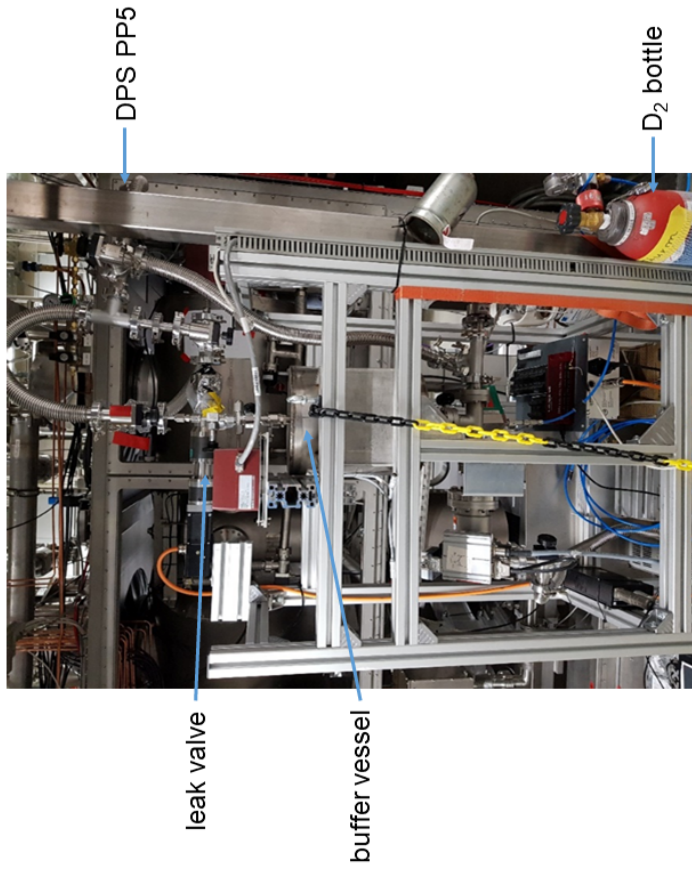
With the same set-up and procedure as described in section 3.2.5.2 the volume of the buffer vessel V_{buf} was determined. The reference volume V_{ref} was installed between VMO-9 and VMO-10, leaving an intermediate volume V_{int} between V_{ref} and V_{buf} . Similar to 3.2.5.2 the measurement was repeated three times. The starting pressure p_0 was 500 mbar, ensuring that the end pressure p_2 is still of the same order of magnitude. Thereby, the uncertainty on the pressure reading is decreased. With the measured values listed in table B.2, and equation (3.16), the buffer vessel volume can be determined as

$$V_{\text{buf}} = (15\,863 \pm 46) \text{ m}\ell . \quad (5.6)$$

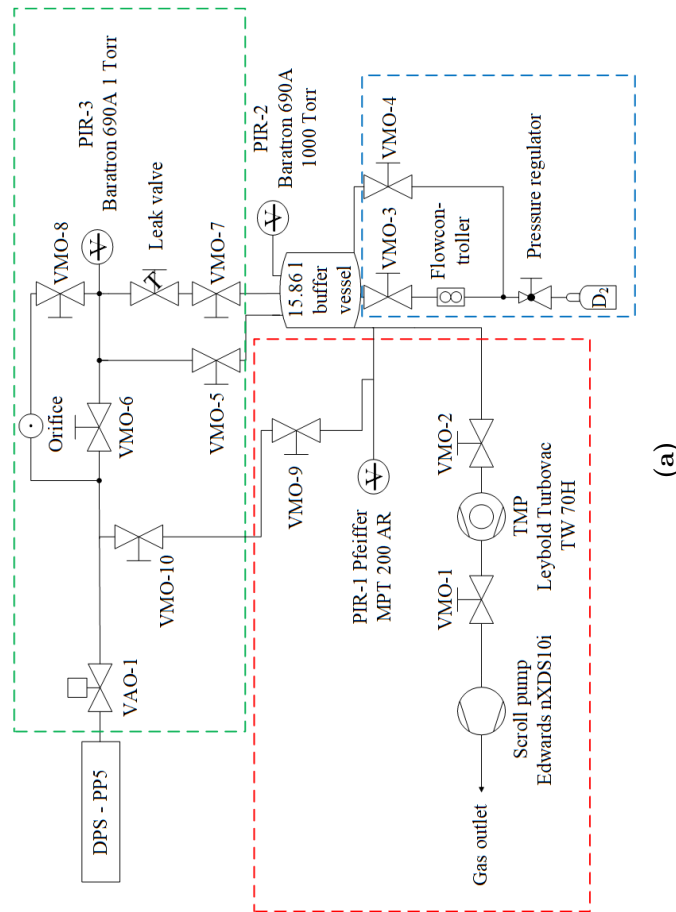
For the uncertainty estimation the same conditions as in 3.2.5.2 are valid.

5.1.2.2. Test measurement with helium

In order to test the functionality of the deuterium inlet system, in particular the handling of the leak valve and the read-out of the pressure sensors at both CPS



(b)



(a)

Figure 5.2.: P&I diagram and picture of deuterium inlet system. (a) The P&I diagram of the deuterium inlet system connected to DPS PP5 is shown. It can be divided into four parts. The first part surrounded by a red box consists of a scroll pump and a turbo molecular pump and three manual valves. In the blue segment the 15.86 l buffer vessel can be filled with deuterium either via a manual valve (VMO-4) or via a flow controller. The third part (green) mainly contains a leak valve, an MKS Baratron 690A 1 Torr, an orifice ($\varphi = 0.5$ mm) and several valves with the purpose to control the injection flow inside the CPS. (b) This picture shows the deuterium inlet system connected to the DPS PP5.

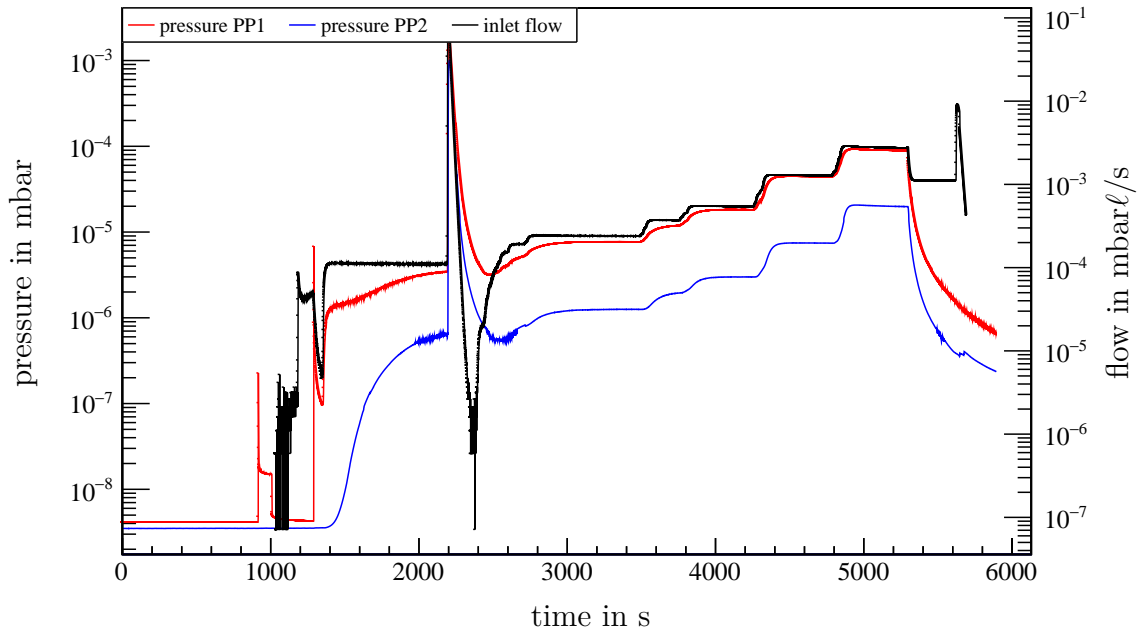


Figure 5.3.: Helium injection into the CPS. The plot shows the pressure at both CPS pump ports (red and blue line) during helium injection into DPS PP5 at different helium injection flow settings (black line). The disturbance between 2100 s and 2300 s is attributed to too fast operations of the manual valve.

pump ports, a commissioning measurement with helium was performed. Helium is not affected by the cold trap at 4.5 K [WZB54], therefore the beam tube conductance can be estimated from the reduction of the flow rate. Additionally, the TMP at CPS-PP2 was running to prevent an overfilling of the beam tube volume with helium.

Figure 5.3 shows the variation of the pressures at both CPS pump ports over time during injection of different helium injection flows. In the beginning the system takes some time to reach stable conditions. While the injected flow rate is then constant between 1400 s and 2200 s, both pressures are still increasing. Before reaching stable pressures the flow rate was increased. The peak at around 2250 s underlines the importance of a proper handling of the manual leak valve. An improper operation causes the flow rate to increase too fast, disabling the determination of the injected gas amount. Therefore the leak valve was closed temporarily so that enough helium could be pumped out before the injection started again. Afterwards the flow rate was only increased again after the pressure was stabilized. Given that the pressure at both CPS pump ports afterwards increases simultaneously with the injected flow rate, the system behaves like expected. The pressure ratios between PP1 and PP2 can be used to estimate the conductance $C_{\text{CPS-BT}}$ in between or the pumping power of the cold trap respectively. As the only active pump is the TMP at PP2, the flows at PP1 and PP2 can be described by

$$q_{\text{PP1}} = q_{\text{PP2}} \rightarrow S_{\text{eff,PP1}} \cdot p_{\text{PP1}} = S_{\text{eff,PP2}} \cdot p_{\text{PP2}} , \quad (5.7)$$

with the effective pumping speed S_{eff} given by [Jou08]

$$S_{\text{eff}} = \left(\frac{1}{S} + \frac{1}{C} \right)^{-1}. \quad (5.8)$$

In case of PP1, the conductance C is defined by the geometry from the CPS-PP1 pressure sensor to the TMP at PP2 (including the cold trap), while for PP2 the conductance between the PP2 cold cathode and the TMP has to be taken into account. The helium pumping speed $S_{\text{He}} = 255 \ell \text{ s}^{-1}$ is given by reference [Vach] and the conductance of PP2 can be derived of its geometry properties to $C_{\text{PP2}} = 100 \ell \text{ s}^{-1}$. Using equation (5.8) and solving equation (5.7) for $C_{\text{CPS-BT}}$ leads to

$$C_{\text{CPS-BT}} = \left(\left(\frac{1}{S_{\text{He}}} + \frac{1}{C_{\text{PP2}}} \right) \frac{p_{\text{PP2}}}{p_{\text{PP2}}} - \frac{1}{S_{\text{He}}} \right)^{-1}. \quad (5.9)$$

The evaluation of p_{PP1} and p_{PP2} for $t = 3400 \text{ s}$ results in

$$C_{\text{CPS-BT}} = (12.2 \pm 2.5) \ell \text{ s}^{-1}. \quad (5.10)$$

Due to the approximation of equation (5.8) as well as the estimation of C_{PP2} the uncertainty is assumed to be in the 20% range. It has to be noted that this conductance was calculated for helium, therefore for tritium operation the value has to be multiplied by a factor $\sqrt{M_{\text{D}_2}/M_{\text{T}_2}} = \sqrt{2/3}$. The influence of the 3 K cooling (4.5 K cooling during measurement) can be neglected because the parts with the nitrogen cooling and room temperature will dominate.

5.1.2.3. Calibration of the residual gas analyzer

The *Pfeiffer Vacuum Prisma QME 200* residual gas analyzer (RGA) was used for the commissioning measurements, enabling a more sensitive measurement of the pressure at PP2. Since the RGA only records ion currents, the calculation of the reduction factor requires calibration of the corresponding partial pressure. Therefore, the cold cathode located at PP2 was used as a reference. The cold cathode measures the full pressure p_{ges} , whereas the RGA only records certain ion currents i_j , leading to

$$\sum_j c_j \cdot i_j = p_{\text{ges}}, \quad (5.11)$$

where c_j is the calibration factor for the corresponding ion mass j . The calibration was performed during a regeneration of the cold trap after a deuterium reduction measurement (without argon frost layer). The valve to the DPS and prespectrometer were closed while the TMP at PP2 was running. Consequently, the pressure increase is mainly induced by the outgassing deuterium from the inner beam tube surface, which was released during slowly heating up the cold trap. As the temperature distribution of the cold trap is inhomogeneous it is also not possible to warm up the beam tube simultaneously in equal steps. In order to obtain a preferably small temperature rise gradient, the return valve *VAI-2-9004* of the 3 K cooling circuit was changed to different openings.⁴

In figure 5.4 the process of the calibration is shown. After about 400 s the pressure at PP1 and the 4 amu^5 ion current (corresponding to deuterium) increase. The

⁴Normally it is at 100%.

⁵Atomic mass unit.

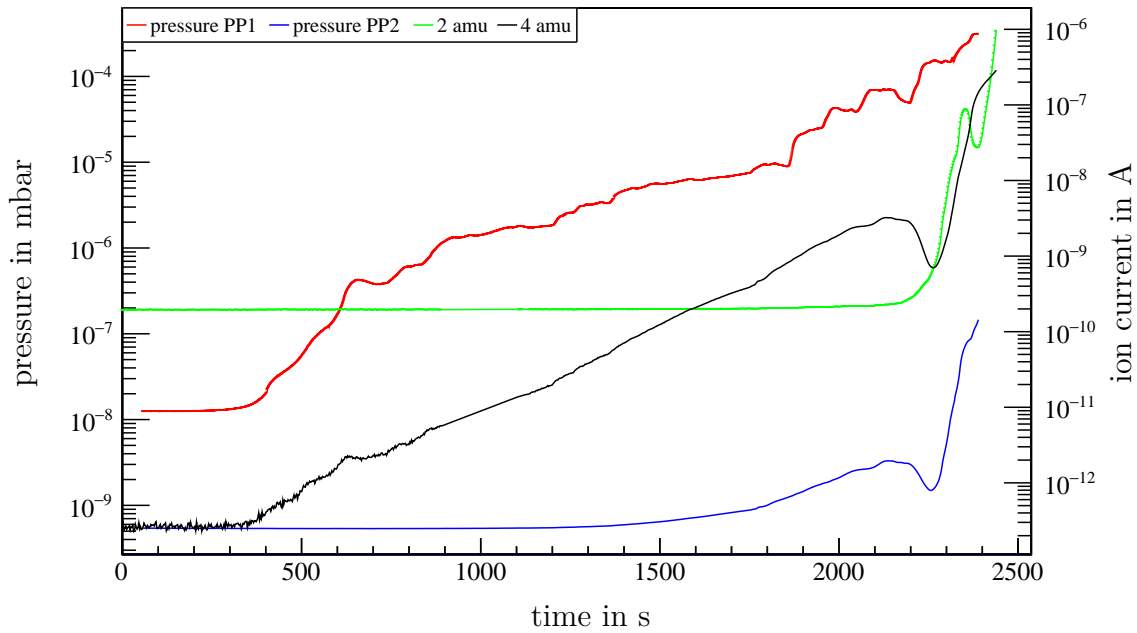


Figure 5.4.: CPS regeneration. The pressures at PP1 and PP2 (cold cathode) are shown in red and green over time in seconds (left-hand axis). Additionally, on the right-hand axis ion currents recorded with the RGA are drawn in green and black.

pressure gauge at PP1 is located closer to the cold trap than the one at PP2 so that the outgassing deuterium is detected at PP1 first. Furthermore, most of the previously injected D_2 is stored in beam tube 2 (compare section 4.3.3). Because the RGA is more sensitive than the cold cathode, it detects the pressure rise at PP2 before the cold cathode. The cold cathode starts to detect an increase after 1400 s, which marks the begin of the calibration interval. Since a cold cathode has different calibration factors for the individual gases, this has to be considered for the correct read-out and evaluation. Therefore, for the time interval after the pressure increase, the calibration factor for deuterium $a_4 = 1/0.46$ (compare section 5.1) is used (shown in figure 5.5(a)). The pressure p_{beg} at the beginning of the regeneration was not corrected as was neither of the plotted ones in figure 5.4. Figure 5.5(a) shows the influence of the correction by using the D_2 calibration factor for the cold cathode: the corrected pressure becomes larger than the read-out value.

As the interesting part is the calibration factor of the RGA for D_2 , equation (5.11) can be rewritten as

$$c_4 \cdot i_4 + \sum_{j \neq 4} c_j \cdot i_j = p_{\text{ges}} . \quad (5.12)$$

Using the corrected pressure of the cold cathode and plotting it against the ion current i_4 in the time range between 1400 s and 2100 s, c_4 can be derived by a linear fit

$$c_4 \cdot i_4 + \sum_{j \neq 4} c_j \cdot i_j = a_4 \cdot p_4 + p_{\text{beg}} . \quad (5.13)$$

Considering the systematic uncertainties for both the cold cathode (10% of read-out

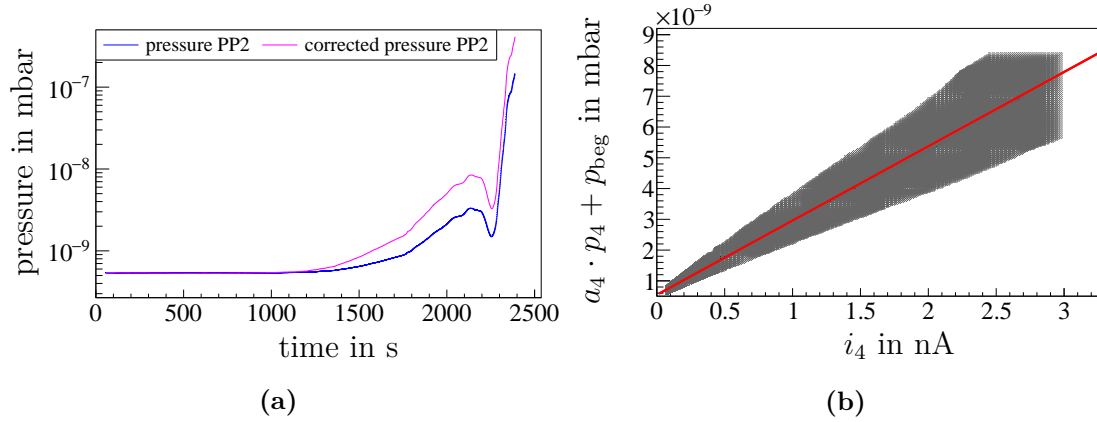


Figure 5.5.: Calibration of the RGA at CPS-PP2. (a) The D_2 -mass corrected pressure (magenta) is plotted together with the read-out pressure in blue (see figure 5.4) over the measurement time period. (b) Fit of the calibration factor for the RGA.

value [MIA]) and the RGA (10% of read-out value [Vacc]), figure 5.5(b) was drawn.

Fitting of the data reveals the calibration factor

$$c_4 = (2.414 \pm 0.039) \text{ mbar A}^{-1}, \quad (5.14)$$

which will be used for all further measurements.

5.1.2.4. Reduction measurements without argon frost layer

After the successful commissioning of the deuterium inlet system with helium including the accurate calibration of the pressure sensors, deuterium is used to gain first information about the performance of the cryogenic pump. First deuterium measurements were performed without an argon frost layer. Since during the commissioning phase the pressure sensors were not yet linked into an automated alarm system to stop deuterium injection before overpressure occurs, the TMP at pump port 2 was running during the measurements. Therefore, the reduction factor cannot be calculated by the simulated ad-hoc factor k (see section 4.3.2) times the pressure ratio at PP1 and PP2 but k has to be updated taking the additional TMP into account.

Including the sticking probability of $\alpha = 0.104$ (corresponding to the deuterium pumping speed for a *HiPace 300* TMP) into the MolFlow+ simulation, a new ad-hoc factor $k_{\text{TMP}} = 14$ has been determined. Here only the case with a sticking probability of $\alpha = 0.7$ for the cold trap was investigated, backed up by reference [Hae81]. As shown in section 4.3.2 a decrease for $\alpha = 0.1$ results in a change by less than 10%. The reduction factor R is then given as

$$R = k_{\text{TMP}} \cdot \frac{p_{\text{PP1}}}{p_{\text{PP2}}}. \quad (5.15)$$

After each measurement, a regeneration cycle of the beam tube was performed. For this purpose, the beam tube sections 2-5 were warmed up to a temperature of 40 K, while the released deuterium was pumped out by the TMP at PP2. When the pressure in PP1 was back to its nominal level, the cold trap was cooled down back to 4.5 K, which allowed to start a new measurement with a regenerated gold surface. Such a regeneration cycle typically takes one day.

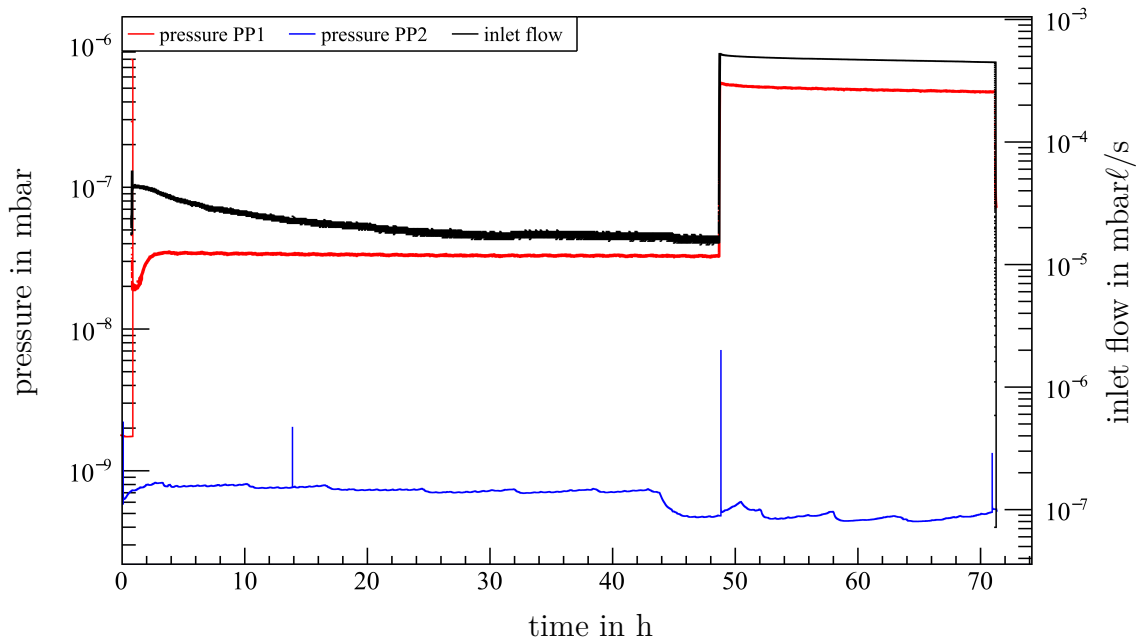


Figure 5.6.: CPS D_2 reduction measurement on gold surface. The pressures at PP1 and PP2 are plotted in red and blue, respectively, over time in hours. In black the injected flow into DPS PP5 is drawn.

5.1.2.4.1. First deuterium reduction factor measurement

In the beginning of the measurement, the deuterium injection flow was regulated to about $4 \times 10^{-5} \text{ mbar } \ell \text{ s}^{-1}$. Because of problems with the RGA at PP2 during data taking⁶, only the values from the cold cathode can be used.

In figure 5.6, the course of the measurement can be seen. The PP1 pressure quickly reaches equilibrium and stays constant until the injection flow is increased. As the pressure in PP2 did not change significantly (by less than a factor of 2), the injection flow was increased by about a factor of 10. The higher flow enabled a better sensitivity for the reduction factor by a higher pressure ratio while still meeting the molecular flow requirement.

At PP2 three spikes can be seen over the whole measurement time range. Those are not related to the performance of the cold trap but can be explained by fluctuations in the CPS nitrogen cooling system. Another explanation for the second peak can be the change in PP1 due to the increase of the injection flow. Furthermore the pressure at PP2 seems to drop over the measurement time range. This effect is related to the outgassing of deuterium and other gases from the previous commissioning measurement behind the valve V3. As the TMP was running, this gas was pumped away resulting in a lower pressure, which gives a better sensitivity for the reduction factor.

From this measurement it can be learned that in contrast to the helium test the pressure at PP2 did not increase when starting the deuterium injection, proving

⁶The calibration of the RGA described in section 5.1.2.3 was performed after this measurement.

that the cryo trap can pump deuterium. With equation (5.15) a first lower limit⁷ for the reduction factor can be stated

$$\begin{aligned} R &\gtrsim k_{\text{TMP}} \cdot \frac{p_{\text{PP1}}(t = 65 \text{ h})}{p_{\text{PP2}}(t = 65 \text{ h})} \\ &\gtrsim 14 \cdot \frac{4.80 \times 10^{-7} \text{ mbar}}{4.39 \times 10^{-10} \text{ mbar}} \approx (1.53 \pm 0.22) \times 10^4. \end{aligned} \quad (5.16)$$

The result is limited because of the sensitivity of the pressure gauge installed at PP2. One has to mention that for the pressure at PP2 the calibration factor for D₂ is used over the whole time range. Since the calibration factor for deuterium is ¹/0.35, the pressure at CPS-PP2 will be smaller, if the cold cathode does not see any deuterium. The uncertainty calculation uses an uncertainty of 10% for the measured values of both pressure gauges as well as for the simulated ad-hoc factor k_{TMP} .

Since a pressure in the 10⁻¹⁰ mbar range reaches the sensitivity limitation of a cold cathode, and the requirement of a molecular flow into CPS has to be met, this measurement equipment does not allow for a more precise result. Nevertheless, the overall injected pV amount of D₂ was more than a factor 50 times the value of a standard 60 d run. Because of the decrease of the reduction factor over time (compare section 4.3), the lower limit can be seen as a very conservative estimation. After this measurement, the malfunctioning RGA at PP2 was exchanged in order to achieve a better sensitivity in the following measurements.

5.1.2.4.2. Reduction factor measurement with a residual gas analyzer

With the new RGA installed, a new reduction measurement was started. For the partial pressure at PP2, the calibration measurement described in 5.1.2.3 was used. The calibration was performed only after the measurement by releasing the deuterium stored in the cold trap. Using the result from initial measurements, the injection flow was set to $4 \times 10^{-4} \text{ mbar } \ell \text{ s}^{-1}$.

After about 20 h the opening of the leak valve was slightly increased to achieve the targeted flow, which can be seen in figure 5.7. This results in a marginal increase of the pressure at PP1 and a slightly higher slope in the pV amount curve. The pressure at PP2 shows no increase over the whole time range, only noise at the sensitivity of the RGA is visible. However, with the RGA the measured pressure is in the range of 10⁻¹³ mbar (a factor of 10³ lower than with cold cathode), enabling a better sensitivity for the reduction factor. A new lower limit for the reduction factor is calculated as

$$\begin{aligned} R &\gtrsim k_{\text{TMP}} \cdot \frac{p_{\text{PP1}}(t = 47.5 \text{ h})}{p_{\text{PP2}}(t = 47.5 \text{ h})} \\ &\gtrsim 14 \cdot \frac{4.50 \times 10^{-7} \text{ mbar}}{4.10 \times 10^{-13} \text{ mbar}} \approx (1.54 \pm 0.31) \times 10^7. \end{aligned} \quad (5.17)$$

The uncertainty for the partial pressure recorded by the RGA is assumed to be 10% of the measured value [Vacc]. As the sensitivity of the RGA is three orders of magnitude better sensitivity, the estimated lower limit is now in the range of the 10⁷ requirement. Though the total injected pV represented about 100×60 d

⁷A central value could only be stated if a pressure increase at PP2 were seen.

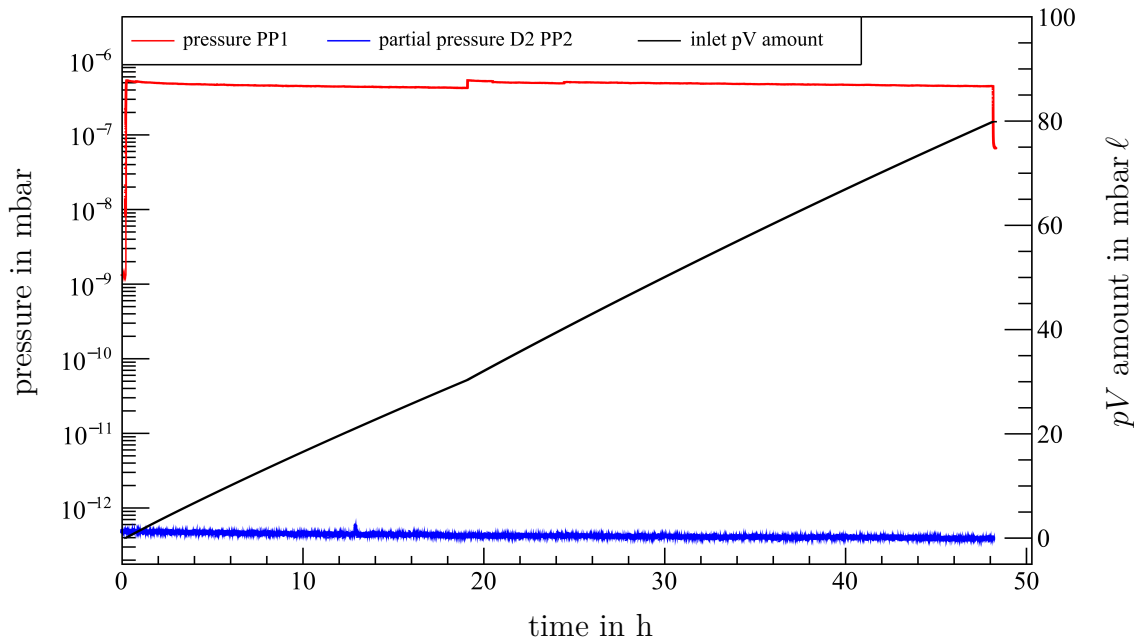


Figure 5.7.: Reduction factor measurement of gold surface with RGA. The pressures at PP1 and the partial pressure of deuterium at PP2 are plotted in red and blue, respectively, over time in seconds. The black line shows the injected pV amount by the deuterium inlet system.

measurements, the reduction factor requirement of $R > 10^7$ was still met. Therefore it can be concluded that the cold trap capacity is totally sufficient for standard operation of KATRIN. When the cold trap is operated at nominal temperature of 3 K, the reduction factor is presumably even larger as the measurement was executed at a cold trap temperature of 4.5 K instead of the designed 3 K.

In conclusion, the results without an argon frost layer are very promising with regard to the CPS reduction factor. As the nominal operation will include an argon frost layer, further measurements discussed in the following results focus on configurations with an argon frost layer.

5.1.2.5. Reduction factor measurements with an argon frost layer

After the first CPS reduction factor measurements showed promising results even without argon frost, the next step towards the final reduction factor estimation is described in this section. The design of the CPS relies on an argon frost prepared onto the beam tube surface to increase the pumping efficiency.

5.1.2.5.1. First reduction factor measurement with argon frost layer

Following the installation of the argon inlet system, the argon frost preparation procedure was tested. The test used a scheme that accounted for the argon conductances measurements of reference [Röt16] for the valve closing order (different to the scheme described in section 3.2.5). In the first filling all valves to the argon capillary were left open until the buffer vessel interlock triggered. Only during the

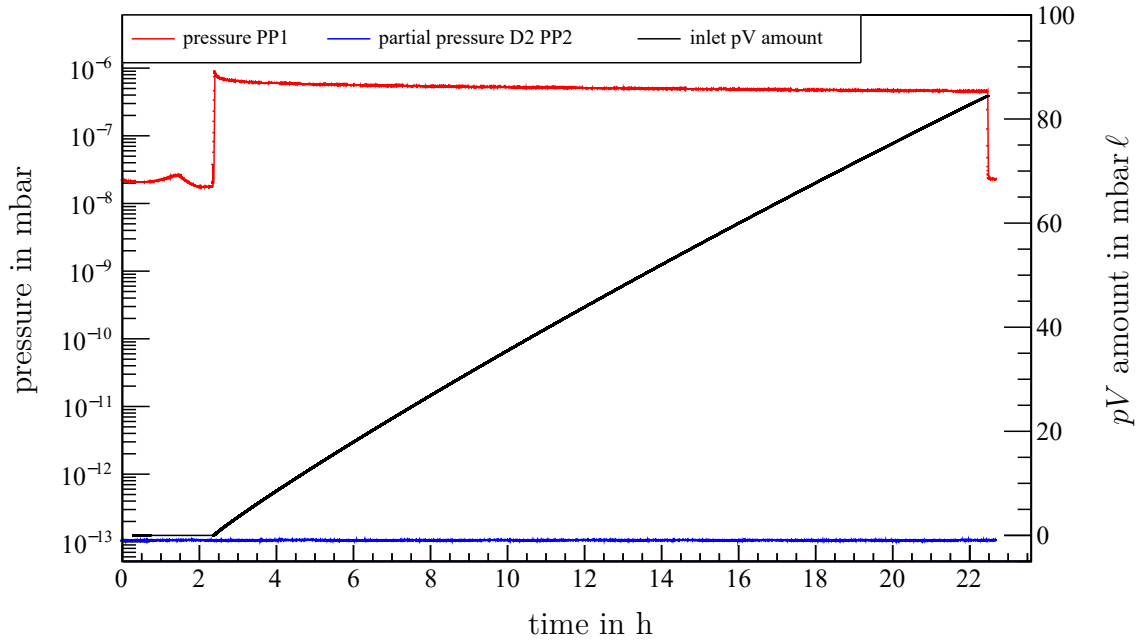


Figure 5.8.: Argon frost reduction factor measurement with a constant injection flow. The pressure at PP1 and the partial pressure at PP2 are plotted in red and blue, respectively, over time in seconds. The black line shows the injected pV amount by the deuterium inlet system.

second filling the valves to the argon capillary were closed manually at a different time. With the difference to the measured conductivities in section 3.2.5, this leads to an inhomogeneous argon frost layer distribution inside the cold trap.

As a first test of the performance, a constant deuterium flow was injected via the deuterium inlet system attached to DPS-PP5 for nearly a day. The temperature of the cold trap was set to the KATRIN standard conditions, switching on the 3 K cooling. For the first time during the CPS reduction measurement the TMP at PP2 was not running, allowing to use the simulated ad-hoc factor $k_{\alpha=0.7} = 18$ to calculate the reduction factor from the pressure ratio.

The result can be seen in figure 5.8, which shows the pressures at both CPS pump ports as well as the cumulative injected deuterium pV amount. The total amount of deuterium injected equals more than 100 times the amount of a 60 d KATRIN run at full tritium column density. Due to the sensitivity of the RGA and the molecular flow rate constraint, only a lower limit can be stated for the reduction factor. Using the ad-hoc factor $k_{\alpha=0.7}$ results in a lower reduction factor limit of

$$\begin{aligned}
 R_{\text{low}} &\gtrsim k \cdot \frac{p_{\text{PP1}}(t = 22 \text{ h})}{p_{\text{PP2}}(t = 22 \text{ h})} \\
 &\gtrsim 18 \cdot \frac{4.54 \times 10^{-7} \text{ mbar}}{1.06 \times 10^{-13} \text{ mbar}} \approx (7.7 \pm 1.1) \times 10^7. \quad (5.18)
 \end{aligned}$$

The reduction factor includes a 10% uncertainty on the measured value of the pressure at PP1 and the partial pressure at PP2 was used. In addition the evaluation

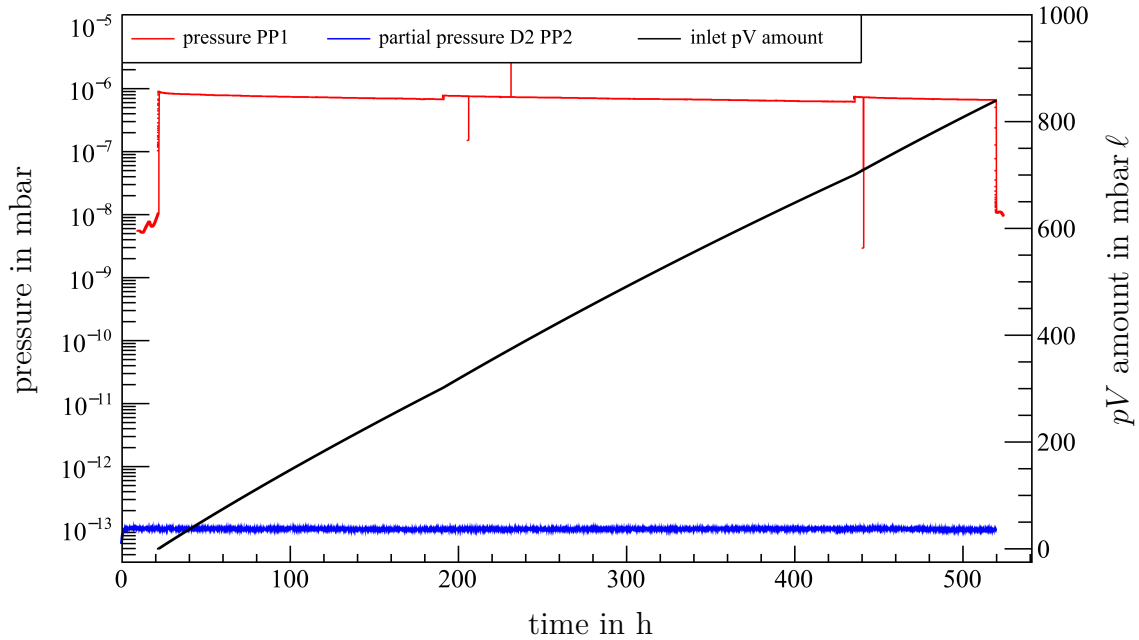


Figure 5.9.: Long time argon frost reduction factor measurement. The pressure at PP1 and the partial pressure at PP2 are plotted in red and blue, respectively, over time in seconds. The black line shows the injected pV amount by the deuterium inlet system.

of the reduction factor after 22 h underestimates the reduction factor due to the decrease of the pumping efficiency over time (see section 4.3). Despite the relatively large uncertainty and the inhomogeneous preparation of the frost layer, the required reduction factor of 10^7 is exceeded.

5.1.2.5.2. Second reduction factor measurement with an argon frost layer

After the first measurement was performed with a non-optimized argon frost preparation, the second measurement used the capillary conductance results (see 3.2.5.3). Furthermore the injection time was increased, to find the point of saturation for the cold trap capacity. The temperature of the beam tube was set to the nominal 3 K cooling setting.

Figure 5.9 shows the development of the pump port pressures over the course of the one-week measurement. During the measurement, two times (at $t_1 \approx 55$ h and $t_2 \approx 120$ h) the setting of the leak valve in the deuterium inlet system was adjusted. With this adjustment, the small decrease of the injection flow rate originating from a decreasing pressure inside the buffer vessel can be compensated. Further peaks in the CPS-PP1 pressure trend are outliers, which most likely originate from fluctuations of the nitrogen cooling regulation of the beam tube section and CPS-PP1. Therefore, they are not considered in the analysis of the measurement. Similar to the previous measurement, the partial pressure at PP2 is stable over the whole time period. With a total deuterium pV amount of 850 mbar ℓ stored inside the cold trap, the measurement was stopped before it could become a safety issue.

The sensitivity was similar as in the first measurement, resulting in a similar lower limit as the previous measurement:

$$\begin{aligned} R_{\text{low}} &\gtrsim k \cdot \frac{p_{\text{PP1}}(t = 140 \text{ h})}{p_{\text{PP2}}(t = 140 \text{ h})} \\ &\gtrsim 18 \cdot \frac{6.75 \times 10^{-7} \text{ mbar}}{9.92 \times 10^{-14} \text{ mbar}} \approx (1.22 \pm 0.17) \times 10^8. \end{aligned} \quad (5.19)$$

In combination with the simulations, the result confirms a high reduction factor.

5.1.2.5.3. Temperature dependence measurement of the CPS reduction factor

In order to further investigate the reduction factor for the CPS with high sensitivity, the limited residual gas analyzer sensitivity requires a different approach to determine the central value of the CPS reduction factor. The cold trap functionality is strongly correlated with its temperature. Therefore, the ratio of the pressures at both CPS pump ports is measured for different beam tube temperatures. Before analyzing the data, the physics conditions are described in the following. Assuming an average number of adsorptions \bar{N} per particle passing the cold trap, the average time $\bar{t}(T)$ for a particle to pass is

$$\bar{t}(T) \approx \bar{N} \cdot \bar{\tau}(T), \quad (5.20)$$

where $\bar{\tau}(T)$ is the average desorption time defined in equation (3.10) for a temperature T . Another assumption is that the pressure at pump port 1, p_{PP1} , is influenced by the injected flow only, which holds in first order. A constant injection flow rate q_{in} thereby should result in a constant pressure at CPS-PP1. For the pressure at CPS-PP2 the relation

$$p_{\text{PP2}}(T) \propto q_{\text{out}}(T) \propto \frac{1}{\bar{t}(T)} \approx \frac{1}{\bar{N} \cdot \bar{\tau}(T)} \quad (5.21)$$

applies. In this interpretation only the temperature dependence will be analyzed. It has to be noted that for the analysis the data points will be binned in temperature regions. During this time period the pressure rise due to the already stored gas is considered as a constant offset, which does not affect the pressure ratio:

$$\frac{p_{\text{PP1}}}{p_{\text{PP2}}(T)} \propto \frac{1}{\frac{1}{\bar{N} \cdot \bar{\tau}(T)}} \propto \bar{N} \cdot \bar{\tau}(T) \propto \exp\left(\frac{E_{\text{des}}}{RT}\right). \quad (5.22)$$

For this temperature dependent pressure ratio, the reduction factor is not just the product of pressure ratio and simulated ad-hoc factor k . The true reduction factor will be larger than the pressure ratio because the adsorbed deuterium will shift p_{PP2} to a higher value. Even with a smaller sticking coefficient α for higher temperatures, the measured pressure ratio will be smaller than the true reduction factor ($k \approx 6$ for $\alpha = 0$, see section 4.3.2).

Therefore, this measurement will state a lower limit for the CPS reduction factor, but with a better sensitivity than the measurements described so far.

The results of the measurement with the argon frost layer are shown in figure 5.10. For temperatures below 6 K, the pressure at PP2 is not influenced due to the limited

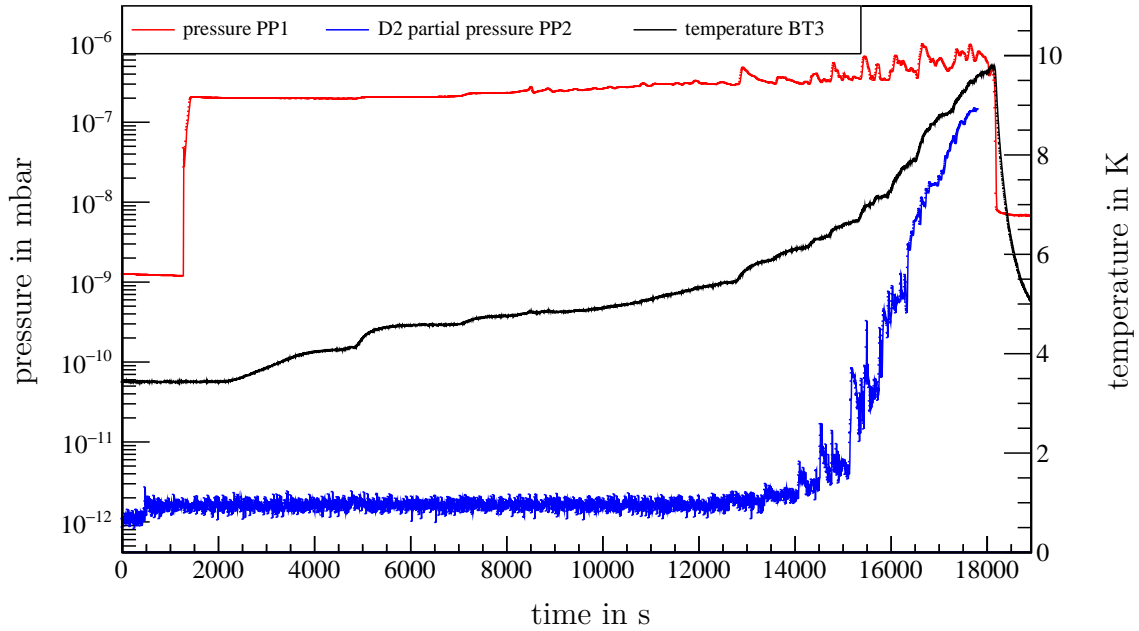


Figure 5.10.: Temperature dependent reduction factor measurement with argon frost. The pressures at PP1 and the D₂ partial pressure at PP2 are plotted in red and blue, respectively, over time in seconds. The black line shows the temperature of *RTY-3-3101*, which is manually increased during the measurement.

sensitivity of the RGA. The pressure at PP1 changes by less than a factor of 3 and will be treated as constant. The peaks in the PP1 pressure correlate to the immediate times when the beam tube temperature has been set to a new setpoint. Since those time intervals are excluded from the analysis by the requirement of a stable temperature (squared deviation smaller than 0.15 K for more than 100 s), this will not influence the measurement. After the D₂ partial pressure reached a value of 10⁻⁸ mbar, the RGA was turned off in order to prevent damage of the electron multiplier. At the corresponding temperature, the retention of the cold trap is close to 0; the gas flow reduction is mainly caused by the conductance of the geometry.

The averaged pressure ratios are plotted in logarithmic scale against the temperature in figure 5.11. Before the time stamp of 12 000 s, the RGA records only noise. Therefore, the analysis only includes data after 12 000 s. The statistical uncertainty is estimated as the standard deviation of the bins. Additionally, the systematic uncertainties for both pressures (10% of read-out value) and the temperature (0.12 K⁸) are added quadratically. The curve fitted is of the form

$$\frac{p_{PP1}}{p_{PP2}} = \exp(a) \cdot \exp\left(\frac{b}{T}\right), \quad (5.23)$$

where a and b are the fitting parameters. The fit was performed by taking the

⁸This uncertainty is based on an internal KATRIN report.

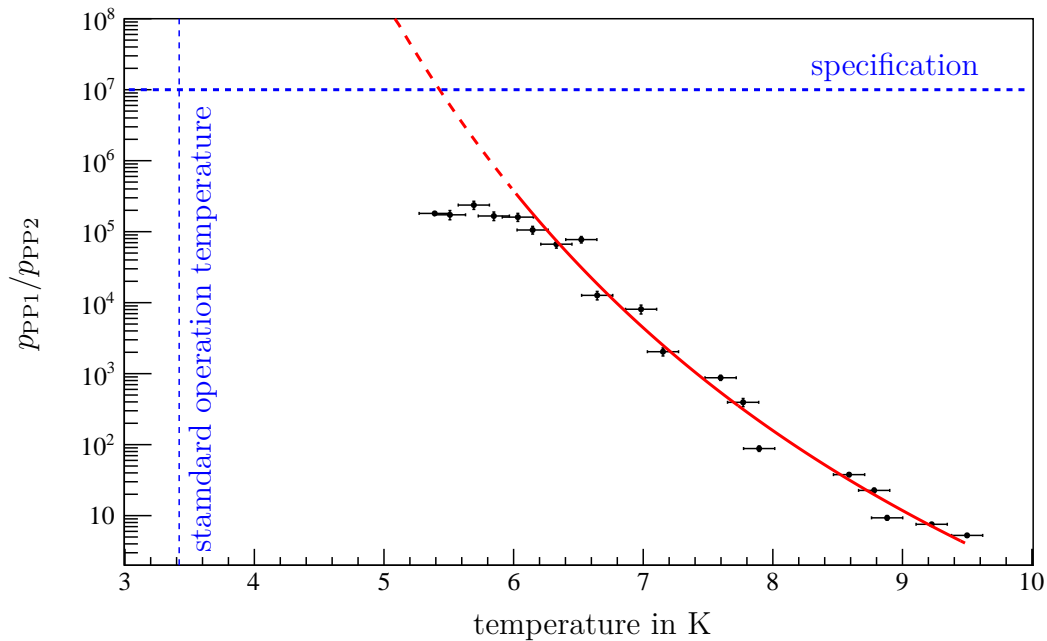


Figure 5.11.: Extrapolation of CPS reduction with an argon frost layer. The pressure ratio of PP1 and PP2 is plotted over the temperature. Between 6 K and 9.5 K an exponential curve is fitted, which can be extrapolated to lower temperatures. The horizontal dashed blue line represents the requirement for the cold trap, while the vertical one shows the nominal operation temperature. Values below 6 K are excluded due to the sensitivity of the RGA.

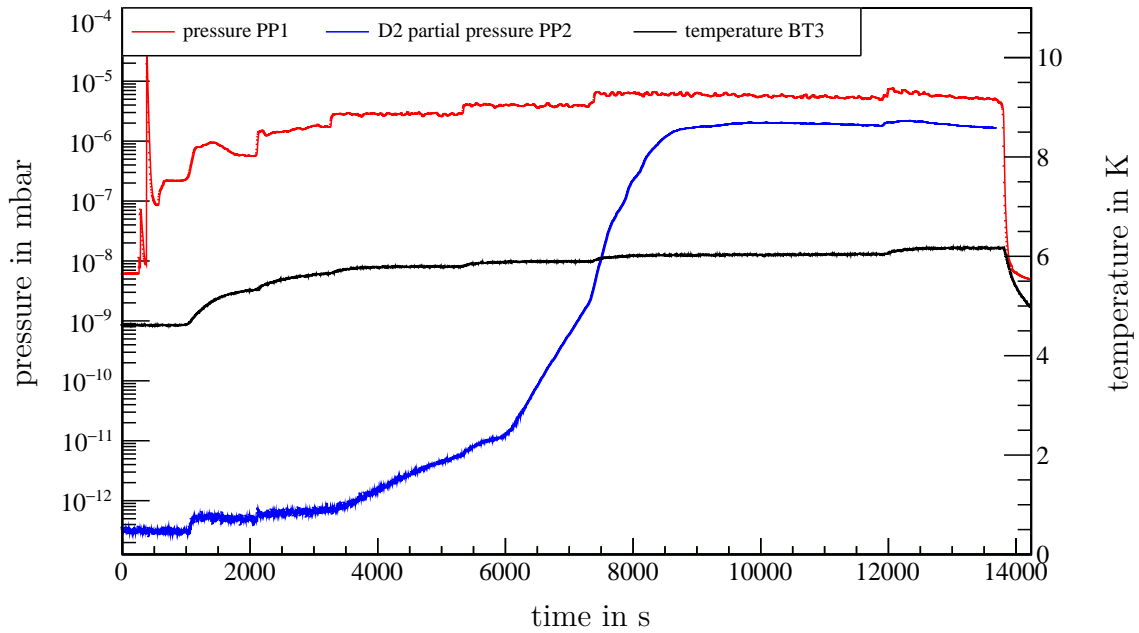


Figure 5.12.: Temperature dependent reduction factor measurement without argon frost layer. The pressures at PP1 and the D₂ partial pressure at PP2 are plotted in red and blue over time in seconds. The black line shows the temperature of *RTY-3-3101*, which is manually increased during the measurement.

logarithm of both sides of equation (5.23), which results in

$$\log \left(\frac{p_{\text{PP1}}}{p_{\text{PP2}}} \right) = a + \frac{b}{T} . \quad (5.24)$$

The fit yields

$$\begin{aligned} a &= -18.3 \pm 0.7 \\ b &= (186.7 \pm 5.6) \text{ K} . \end{aligned} \quad (5.25)$$

The fit parameter b can be translated according to equation (3.10) into a desorption energy

$$E_{\text{des,meas}} \approx b \cdot R = (1553 \pm 46) \text{ J mol}^{-1} . \quad (5.26)$$

This result on the desorption energy has to be treated very carefully since several assumptions hard to quantify completely in its uncertainties were made in its derivation. Remembering the previous measurements with a stable CPS cold trap temperature, a large binding energy does indeed seem reasonable. Extrapolation of the fitting curve to the operating temperature agrees with the different simulated values for $E_{\text{des,meas}}$ considering their relative large uncertainty (see section 4.3).

In summary, the measurements with an argon frost layer conclude that the required reduction factor of 10^7 is well exceeded by several orders of magnitude, while the capacity of the cold trap is also unexpectedly large.

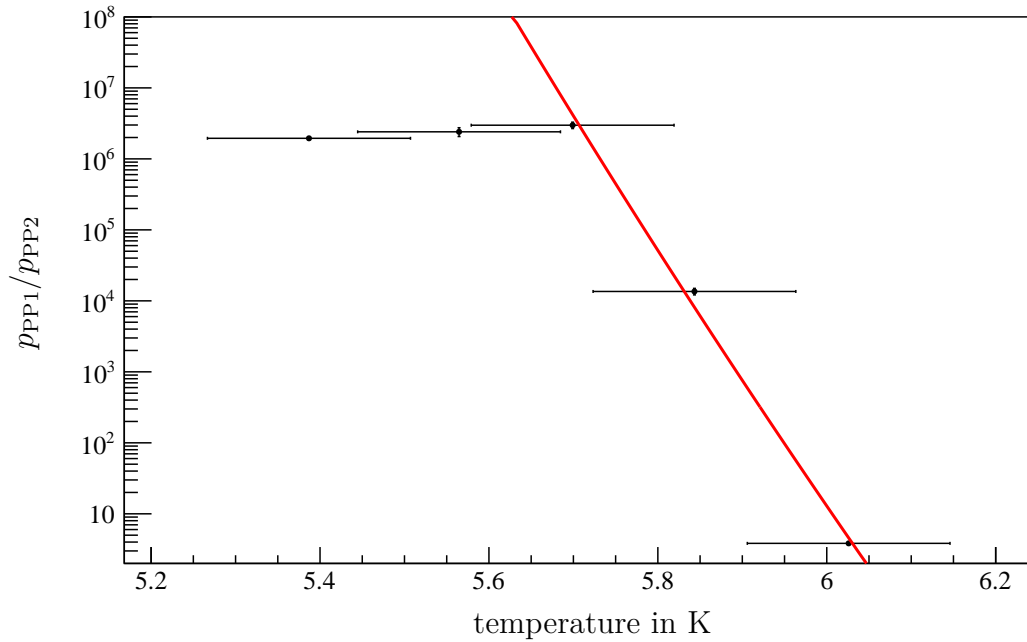


Figure 5.13.: Extrapolation of CPS reduction without argon frost layer. The pressure ratio of PP1 and PP2 is plotted over the temperature. Between 5.6 K and 6.2 K, an exponential fit was used to compare to the argon frost layer measurement.

In order to compare the cryo trap performance with and without argon frost layer, the same procedure was repeated without argon frost. The result is shown in figure 5.12. The pressure rises at PP1 originate from the readjustment of the leak valve in the deuterium inlet system, targeted for a higher pressure ratio to increase the sensitivity. As this measurement was performed after the argon frost layer measurement, the beam tube was already warmed up to 5 K expecting a similar temperature range for the start of a pressure rise in PP2. In contrast to the argon frost layer measurement, the D_2 partial pressure at PP2 rises fast in a narrow temperature window.

Analysis of the measurement is therefore difficult, as can be seen from figure 5.13. After the D_2 partial pressure recorded by the RGA rises above noise, there are only three points that can be used for a fit according to equation (5.23). A fitting range between 5.6 K and 6.2 K leads to

$$\begin{aligned} a &= -238 \pm 124 \\ b &= (1443 \pm 725) \text{ K} . \end{aligned} \quad (5.27)$$

The large uncertainties reflect the fact that two parameters are determined by three data points only. Therefore no desorption energy is calculated.

Nevertheless, the results show that the CPS cold trap exceeds its specified reduction factor at the designed temperature, even without argon frost operation. This is a key finding, as there is no possibility to check the true argon frost coverage of the beam tube, and as a fallback in case argon frost preparation fails out of technical reasons.

Table 5.1.: Summary of CPS reduction factor measurements. The results for the reduction factor R are listed in dependence of the cold trap temperature cooling T , the surface condition, and the measurement method.

T	surface	method	$\log_{10}R$	section
4.5 K	Au surface	cold cathodes	$\gtrsim 4$	5.1.2.4.1
4.5 K	Au surface	calibrated RGA	$\gtrsim 7$	5.1.2.4.2
3 K	Ar frost layer	calibrated RGA	$\gtrsim 7$	5.1.2.5.1
3 K	Ar frost layer	calibrated RGA	$\gtrsim 8$	5.1.2.5.2
3 K	Ar frost layer	extrapolation of temp. dependence	$\gg 10$	5.1.2.5.3
3 K	Ar frost layer	simulation	12-14	4.3

The results of this section are summarized in table 5.1. These measurements allow a start with tritium operation. As the retention systems work properly there are no indications that tritium will contribute to the background rate.

5.2. Measurements with tritium

As the DPS and CPS commissioning measurements exceeded the requirements on retention and capacity the next milestone of the KATRIN experiment was approached: Trace⁹ amounts of tritium with deuterium as carrier gas were circulated in the source system and first tritium spectra were recorded with the KATRIN experiment. This First Tritium campaign was aimed to test the spectroscopic performance of the as-built KATRIN set-up with nominal gas flow. Despite successfully recording first tritium β -spectra, the large statistical uncertainty during this commissioning operation does not allow as expected a neutrino mass analysis but allowed a series of sensitivity studies as described in section 5.2.1. In section 5.2.2 the overall reduction factor of WGTS and DPS is analyzed by using the accumulated tritium activity frozen on the argon frost layer of the CPS. In order to check whether the source activity affects the background rate, stability analyses of the background were performed, as described in section 5.2.3.

5.2.1. Goals of the First Tritium campaign

In May 2018, tritium was injected for the first time into the KATRIN beam line. The goal of this measurement campaign was to demonstrate the stability of the different subcomponents, which were in combined operation for the first time. However, a component not ready for operation was the rear section, for which the commissioning phase started after the First Tritium campaign in September 2018. The non-availability of the rear section implies that the column density cannot be determined with the designed systematic uncertainty budget [Hei19]. In order to minimize the risk of a tritium contamination of the spectrometers, the gas injected into the WGTS contained only 0.5% of tritium in deuterium as carrier gas. Dedicated measurements were performed to prove that the ion flux into the main spectrometer is smaller than 10^4 ions s^{-1} [Kle19]. With trace amounts of tritium the allowed limit for the ion rate can be increased by two orders of magnitude, since in this configuration deuterium ions are dominant. Only after the performance of the ion retention

⁹In the order of 0.5%.

system was validated with the instruments of the source and transport section, the valve to the spectrometers was opened. Before using the regular tritium loop supply, the Very First Tritium (VFT) measurement campaign used four sample cylinders filled with tritium as inventory that were connected to the inner loop system. The measured ion flux into the CPS enabled to open V4 on the next day [Kle19].

On May 18, the contents of the first tritium sample cylinder were injected to the inner loop. With V4 closed, a Faraday cup instead of the FBM was inserted into CPS-PP2. The Faraday cup is designed to determine both, electron and ion rate.

After using the second sample cylinder for ion measurements, technical issues (air contamination in cryo-circuits) with the *Helium Plant TCF50* cryocooler required a change of plans. The remaining two sample cylinders were injected to record the first eight tritium spectra with the KATRIN experiment. Out of the eight 30 min runs, four showed a stable column density while for the others it already decreased due to the limited inventory of the gas cylinders [Kle19].

Finally the cryogenic problems resulted in a failure of the cryogenic cooling system, the WGTS and CPS magnets were ramped down via a slow discharge (triggered by the safety interlock). As the repair of the cryocooler required WGTS and CPS cryostats to be separated from the cooling system, both components warmed up. It took two weeks to repair and bring back the cryo systems to standard operation, which then marks finally the start of the First Tritium (FT) campaign. During these two weeks of down-time the sample cylinders were removed and the tritium-deuterium mixture was prepared in a buffer vessel, which is connected to the loop system and will also be used in KATRIN standard operation. Ion measurements started the FT campaign on June 5, followed by two weeks of continuous gas circulation. Several measurements were performed to investigate different scanning strategies (e.g. randomized high voltage steps, different run lengths, ...), search for sterile neutrinos, stability runs, and continuation of the ion measurements. After these two weeks, the injection of gas into the WGTS was stopped and background measurements were started.

The following sections 5.2.2 and 5.2.3 focus from the rich field of first tritium measurements on the tritium retention in the pumping sections and the background rate stability.

5.2.2. Accumulated activity in the cryogenic pumping section

One possibility to check the overall reduction factor of WGTS and DPS is to measure the accumulated activity on the argon frost layer of the CPS cold trap and compare it to the activity injected into the WGTS. Since the commissioning results of the CPS showed a reduction factor larger than 10^7 , to first order tritium entering the CPS adsorbs completely on its cold trap. During regeneration of the cold trap, namely the helium purging process (see section 3.2.5.6), the argon frost adsorbate containing the adsorbed tritium is released from the cold trap and stored in a 506 ℓ buffer vessel. Information about the adsorbed amount of tritium can be gained from determining the activity stored this buffer vessel by a BIXS system (for working principle see section 2.2.2.1). During the helium purging, helium might also enter

the DPS and transport DPS activity into the buffer vessel¹⁰. The valves to the TMPs of the DPS and the valve between WGTS and DPS were closed.

Due to the warm-up after the VFT campaign, the argon frost layer was regenerated before FT so only tritium injected after June 5 has to be taken into account for the analysis. With the measured activity in the buffer vessel A_{BV} (considering the loss of activity since the begin of the tritium injection) and the injected activity into WGTS A_{WGTS} , the overall reduction factor of WGTS and DPS can be calculated as

$$R_{\text{WGTS+DPS}} = \frac{A_{\text{WGTS}}}{A_{\text{BV}}} . \quad (5.28)$$

The activity is proportional to the number of active tritium gas atoms N_{T} , defined through

$$A_{\text{WGTS}} = N_{\text{T}} \cdot \lambda_{\text{T}} , \quad (5.29)$$

with the tritium β -decay constant λ_{T} . Solving the ideal gas law for N_{T} and inserting the measured injected flow rate q_{pV} leads to

$$A_{\text{WGTS}} = \frac{q_{pV} \cdot 0.5 \cdot \epsilon_{\text{DT}} \cdot \lambda_{\text{T}} \cdot t_{\text{bin}}}{k_{\text{B}} \cdot T} . \quad (5.30)$$

Here the factor 0.5 accounts for half of the atoms in the DT molecule, ϵ_{DT} is the fraction of DT in the gas mixture, $t_{\text{bin}} = 300 \text{ s}$ is the binning time, k_{B} is the Boltzmann constant, and $T = 273.15 \text{ K}$ is the temperature, which is needed for the conversion of sccm¹¹ at the flow meter. The injected flow rate is determined from the flow meter in front of the pressure controlled buffer vessel (including a calibration factor). ϵ_{DT} is measured by the LARA system. From equation (5.30) an injected activity of $A_{\text{WGTS}} = (414.82 \pm 0.55) \text{ TBq}$ is determined. For the uncertainty calculation, a 2.5% uncertainty for q_{pV} is assumed.

With the activity $A_{\text{BV}} = (21.0 \pm 4.2) \text{ MBq}$ stored in the buffer vessel as measured by the BIXS detector system. The uncertainty of 20% is dominated by the low count rate in the 506 ℓ buffer vessel (close to the detection limit) together with only 1% DT, which circulated through the KATRIN beam line. Using these values, the reduction factor can be calculated as

$$R_{\text{WGTS+DPS}} = (1.98 \pm 0.40) \cdot 10^7 . \quad (5.31)$$

This value is close to the requirement of 10^7 . Keeping in mind the reduced pumping speed for D_2 and DT compared to pumping T_2 , the actual reduction factor for nominal tritium operation is likely to be larger. This result has been obtained at the designed pumping performance of WGTS and DPS, which is another important milestone for the standard KATRIN operation.

5.2.3. Stability of the background rate

Investigating the background rate behavior during and after injecting tritium provides a check of the tritium retention of the source and transport section. Using the background rate as a proxy for the performance of the tritium retention system

¹⁰The valve V2 between DPS and CPS was stuck in open position at that time

¹¹Standard cubic centimeters per minute.

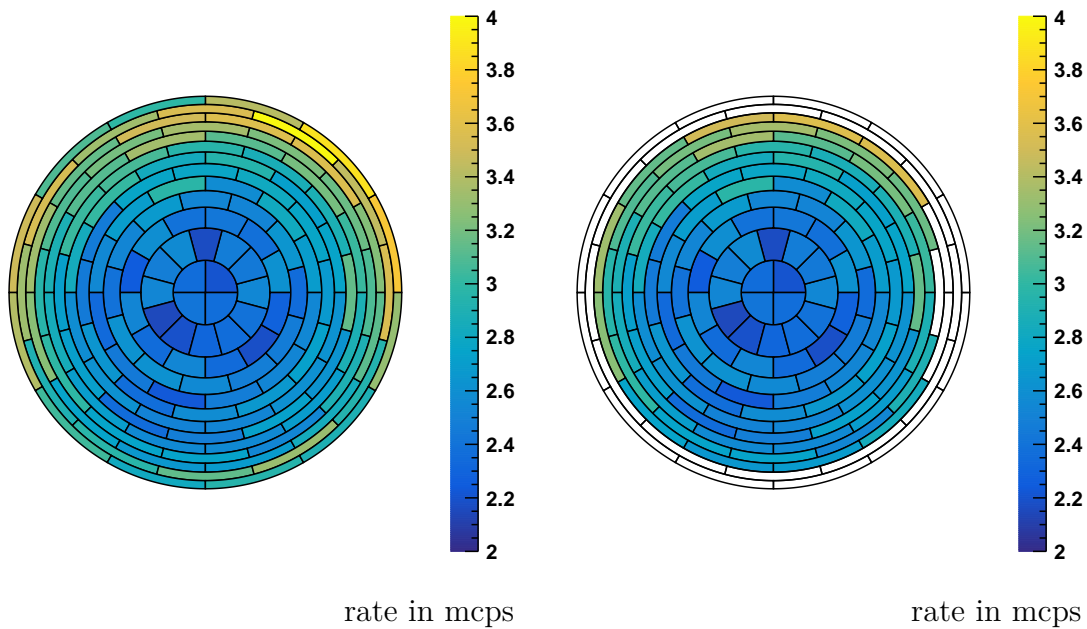


Figure 5.14.: Pixel map of the FPD for the background runs. The average rate of all background runs is shown for each pixel. The left picture shows the full detector, whereas the right picture excludes the pixels not used for the analysis.

assumes that the stability of the underlying processes causing background (see section 2.3) does not change during that time. Since between VFT and FT there were no hardware changes in the spectrometer and detector section (SDS), this assumption seems reasonable.

The reference background level was determined before the VFT campaign. In some cases, the runs used for the following analysis have slightly varying settings. During some runs the pre-spectrometer voltage was changed to investigate if this affects the background rate. Additionally, some runs were taken with a closed valve between the CPS and pre-spectrometer. The parameter most varying is the (sub-) run length; this is caused by the fact that not only the background sub-runs¹² of a tritium scan run were used but dedicated over-night background runs as well. The total run list with all the different settings can be found in appendix G.

A detector pixel map shows the spatial distribution of all pixel-wise averaged background rates in figure 5.14. The energy window for each pixel was set between 14 and 32 keV¹³. The spatial distribution matches the one expected from SDS-background only [Har15] with an increasing rate towards the outer rings of the detector. Furthermore, the rate is higher on the upper right sector compared to the lower parts. This can be explained by a slight misalignment of the beamline having the wall

¹²A sub-run during a β -scan run corresponds to one specific high voltage value of the main spectrometer. The background sub-runs were taken at high voltage values above the endpoint of the tritium spectrum.

¹³The energy resolution of some pixels was worsened unintentionally for this measurement campaign, leading to the selection of a wider region of interest (ROI) here.

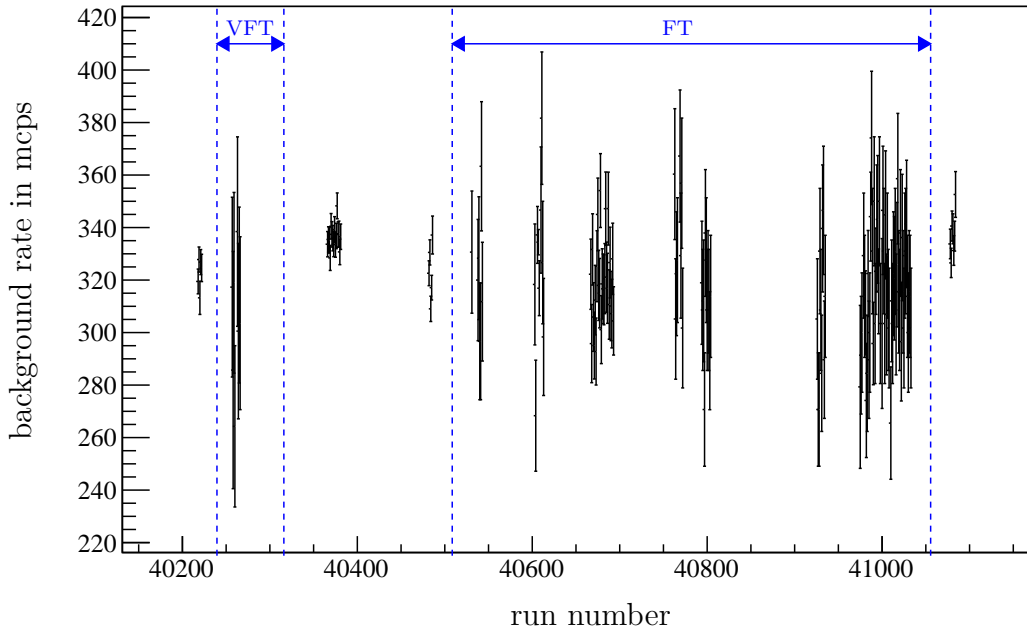


Figure 5.15.: Background rate trend during tritium measurements. The background rates are plotted over the corresponding run number. With the dashed blue lines the beginning and the end of the VFT as well as the FT measurement campaign are marked.

mapped to some outer pixels. Therefore, for a clean analysis the two outer most rings are excluded. Three more pixels on the right side¹⁴ are excluded as they are shadowed by the forward beam monitor. In total, this leaves 121 out of 148 pixels for the following analysis.

The background rates of the different runs are shown in figure 5.15. If a run has several background sub-runs e.g. during a tritium β -scan, a sub-run averaged background rate is shown. Due to the varying run lengths the uncertainties of each data point vary strongly. This holds for the background-specific runs in the time interval between VFT and FT also due to the relatively long measurement time and therefore a smaller uncertainty. The plot does not show an increase of the background rate; this is confirmed by a linear fit, which gives a slope of $(-5.7 \pm 2.8) \times 10^{-3}$ mcps per run and therefore is compatible with zero. The average rate is given by

$$\Gamma_{\text{runs}} = (328.74 \pm 0.77) \text{ mcps} . \quad (5.32)$$

The corresponding standard deviation is calculated as

$$\sigma_{\text{runs}} = 23.01 \text{ mcps} . \quad (5.33)$$

Another approach averages the background rate per day and not only per run.

¹⁴The pixel view looks from detector towards the source (upstream). The left side of the pixelmap therefore corresponds to the eastern side of the source.

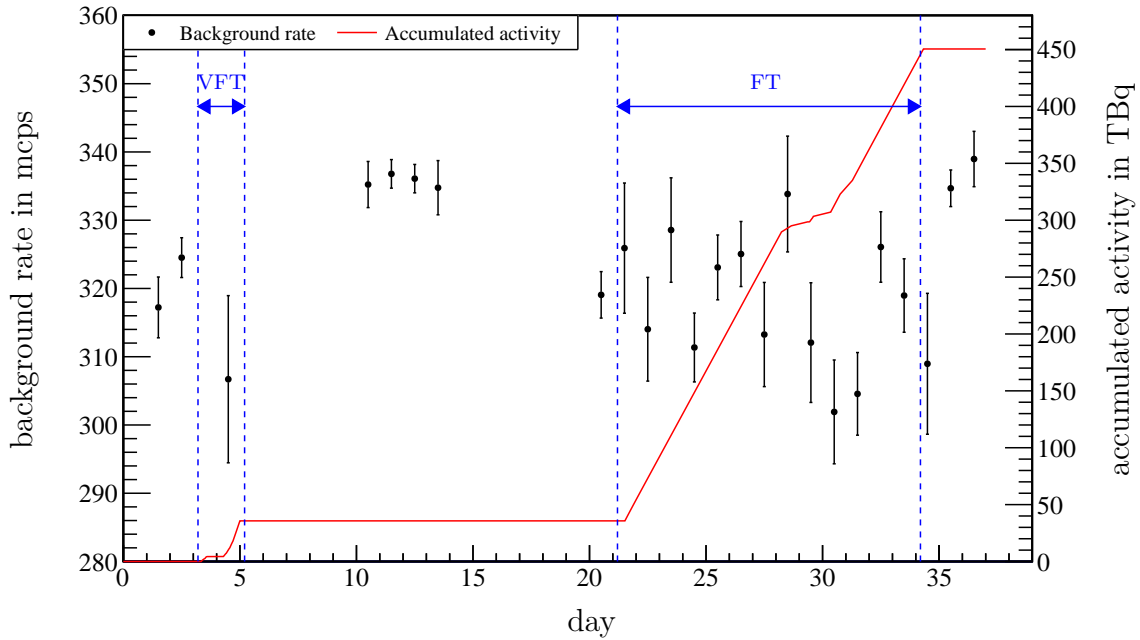


Figure 5.16.: Background rate development over tritium campaign days. The black dots mark the average of the background runs (or sub-runs) measured at the same day with corresponding statistical uncertainty. Day 1 corresponds to May 16th, 2018. The red line represents the cumulative activity inserted into the WGTS.

Figure 5.16 shows the corresponding background rates over all days of the measurement campaign. Similar to figure 5.15 a linear curve was fitted, which results here in a slope of $(-1.3 \pm 0.7) \times 10^{-4} \text{ mcps d}^{-1}$ that is also compatible with zero. The average rate is given by

$$\Gamma_{\text{days}} = (328.97 \pm 0.84) \text{ mcps} , \quad (5.34)$$

with a standard deviation of

$$\sigma_{\text{runs}} = 13.28 \text{ mcps} . \quad (5.35)$$

Comparing this value to the result of equation (5.32), both agree within their uncertainties. This is expected as a different binning of the background rate should not affect the average rate.

In addition to the day-wise background rate, figure 5.16 shows the accumulated activity during the VFT campaign (day 3 and 4) and the FT campaign (day 22 to 34). Overall, an activity of about 419 TBq has been injected into the WGTS including 33 TBq from VFT. During and after tritium circulation, no statistically significant increase of the background rate can be observed.

From this non-observation of a background rate increase, a lower limit on the tritium flow reduction factor of the STS can be stated. First the injected tritium flow Φ_{in} has to be considered

$$\Phi_{\text{in}} = q_{\text{WGTS}} \cdot \epsilon_{\text{T}} , \quad (5.36)$$

with the measured flow $q_{\text{WGTS}} = 1.85 \text{ mbar } \ell \text{ s}^{-1}$ into the WGTS and the fraction of T in the gas mixture $\epsilon_{\text{T}} \approx 5 \times 10^{-3}$. As reported in [MDF⁺13], a tritium flow of $10^{-14} \text{ mbar } \ell \text{ s}^{-1}$ entering the spectrometers would induce a signal rate of 1 mcps. Therefore, the measurable tritium flow into the spectrometer is defined as

$$\Phi_{\text{out,spec}} = \frac{\Gamma_{\text{excl}}}{1 \text{ mcps}} \cdot 10^{-14} \text{ mbar } \ell \text{ s}^{-1} . \quad (5.37)$$

With a background rate of the order 100 mcps, the tritium flow would have to be of the order of $10^{-12} \text{ mbar } \ell \text{ s}^{-1}$ to measure an increase by $\Gamma_{\text{excl}} = 100 \text{ mcps}$ to be clearly identified as a tritium induced background. Therefore the reduction factor is

$$R = \frac{\Phi_{\text{in}}}{\Phi_{\text{out,spec}}} > \epsilon_{\text{T}} \cdot \frac{q_{\text{WGTS}}}{10^{-14} \text{ mbar } \ell \text{ s}^{-1}} \cdot \frac{1 \text{ mcps}}{\Gamma_{\text{excl}}} \approx 10^{10} \quad (5.38)$$

In FT only 0.5% of the circulated gas were tritium atoms, reducing the sensitivity by two additional orders of magnitude. Also the value for Γ_{excl} is high because of the limited background measurement time during and after the FT campaign. Therefore, this analysis states a lower limit of the tritium reduction factor of at least 10^{10} , which is four orders of magnitude less sensitive than needed for the requirement. However, the sensitivity will be increased by more than two orders of magnitude for nominal KATRIN tritium operation with $\epsilon_{\text{T}} > 0.95$ and longer measurement time.

In another approach, the background sub-runs were divided in 300 s long segments¹⁵, and afterwards the corresponding rates were filled in a histogram.

The 300 s binning results in nearly 1800 entries in the histogram, allowing to approximate the Poisson distribution by a Gaussian. The Gaussian fit shown in figure 5.17 reveals a mean μ of

$$\mu = (336.62 \pm 0.87) \text{ mcps} , \quad (5.39)$$

and a standard deviation of

$$\sigma = (35.96 \pm 0.62) \text{ mcps} . \quad (5.40)$$

In contrast to the average background rates given in equations (5.34) and (5.32), the mean of the Gaussian distribution is larger by about 8 mcps. This deviation could be explained by the relatively high reduced χ^2 , which reflects a non perfect Gaussian distribution. Measurements after FT support the statement of no contamination of the SDS with an averaged rate of

$$\Gamma_{\text{after FT}} = (335.83 \pm 2.24) \text{ mcps} . \quad (5.41)$$

As mentioned above, the sensitivity for the tritium reduction factor of the global beamline is very low in the FT set-up. The commissioning measurements with deuterium have shown that the overall reduction factor of the STS is larger than the required 10^{14} . With the elevated background rate (compared to the KATRIN design value), it is difficult to be sensitive to a tritium induced background. Additionally,

¹⁵If the segment length is larger than 240 s, the leftover time is used. Shorter segments were not considered.

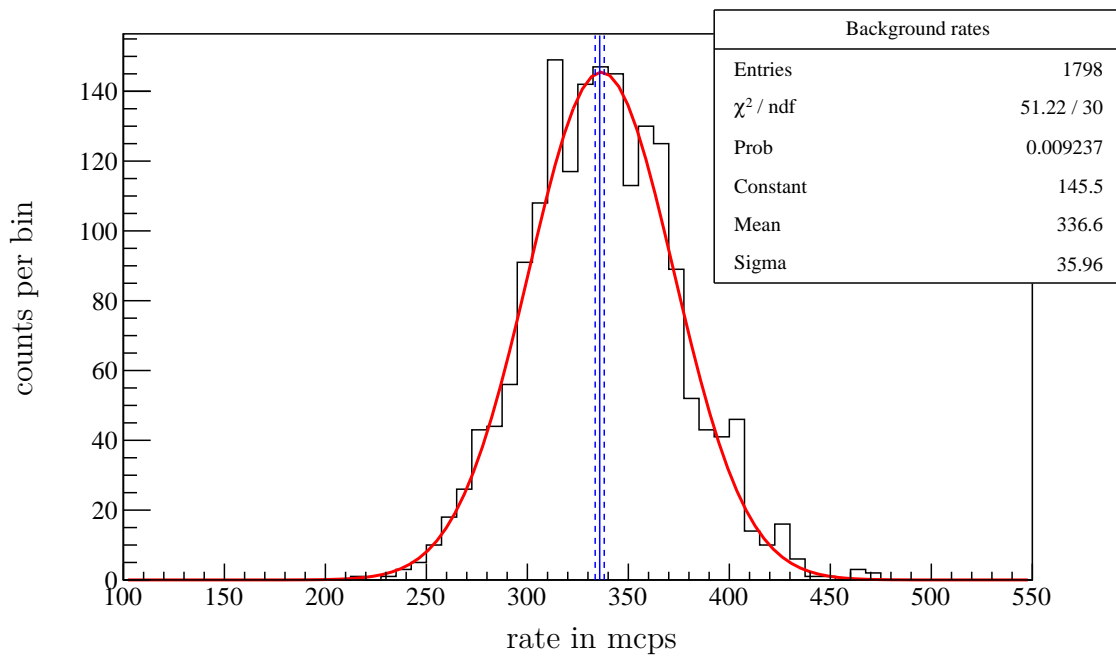


Figure 5.17.: Background rate histogram for tritium measurement campaign.

The histogram is filled with background rates binned within 300s of all runs and sub-runs. In red, a fitted Gaussian distribution is shown. The average background rate of all sub-runs after First Tritium is indicated in blue.

the widened region of interest¹⁶ for the detector pixels result in an approximately 20% higher background rate.

Nevertheless, the measurements show that there is no significant background rate increase, which indicates good conditions for standard tritium operation. In March 2019, KATRIN started routine tritium operation. The nominal 100% T₂ column density will enable a better sensitivity for the reduction factor determination. However, these measurements are not covered in this thesis.

5.3. Summary

One of the factors limiting the KATRIN neutrino mass sensitivity is the background rate. A process that would increase the background rate is tritium contamination of the spectrometer section even with tiny mass flows of 10^{-14} mbar ℓ s⁻¹ into the spectrometer. Therefore, the technical realizations of the required retention over 14 orders of magnitude was one of the biggest technological risks of KATRIN. In this chapter, the dedicated gas-flow reduction factor measurements for the DPS and CPS retention measurements were described, followed by a background rate analysis in the course of the FT measurement campaign. The first part focused on the commissioning measurements with deuterium, testing the general performance of both systems. For the DPS, a standalone reduction factor measurement was not possible. Therefore, the performance was tested together with the KATRIN loop system and the WGTS. As the gas flow into the DPS is very small under these conditions, the results have to be interpreted carefully. Furthermore, there is a distinct difference in the efficiency of the TMPs when pumping deuterium or tritium. From the DPS commissioning results, the DPS requirement of a tritium reduction factor larger than 10^5 could not be confirmed.

A dedicated inlet system was installed at the inlet of the CPS to measure reduction factors of the CPS while keeping molecular flow conditions. This system enabled a gas flow adjustable within six orders of magnitude. With this set-up, cold trap characterization measurements were executed with and without an argon frost layer. Simulation results expect the reduction factor to exceed its requirement (10^7) by at least four orders of magnitude, providing a challenge for the measurement. This challenge became visible in the long term measurements, where deuterium was injected with a constant inlet flow but no increase of the pressure at PP2 above noise level could be observed. Therefore, lower limits were estimated for the reduction factor, confirming the requirement of retentions stronger than 10^7 . An approach with improved sensitivity used the temperature dependence of the desorption time. While the beam tube temperature of the cold trap was slowly increased, the pressure ratio of both pump ports was observed. The results confirmed the previous measurements suggesting a reduction factor several orders of magnitude higher than 10^7 . Though this method has a better sensitivity, a reliable, quantitative central value for the reduction factor could not be determined due to the time dependent changes of adsorbed deuterium molecules with increasing temperature. From simulations, the conclusion can be made that the radioactive decay of tritium molecules adsorbed at the cold trap will be the dominant part, which have to be considered in the desorption processes.

¹⁶Energy range of the detector in which the counts are used for the analysis.

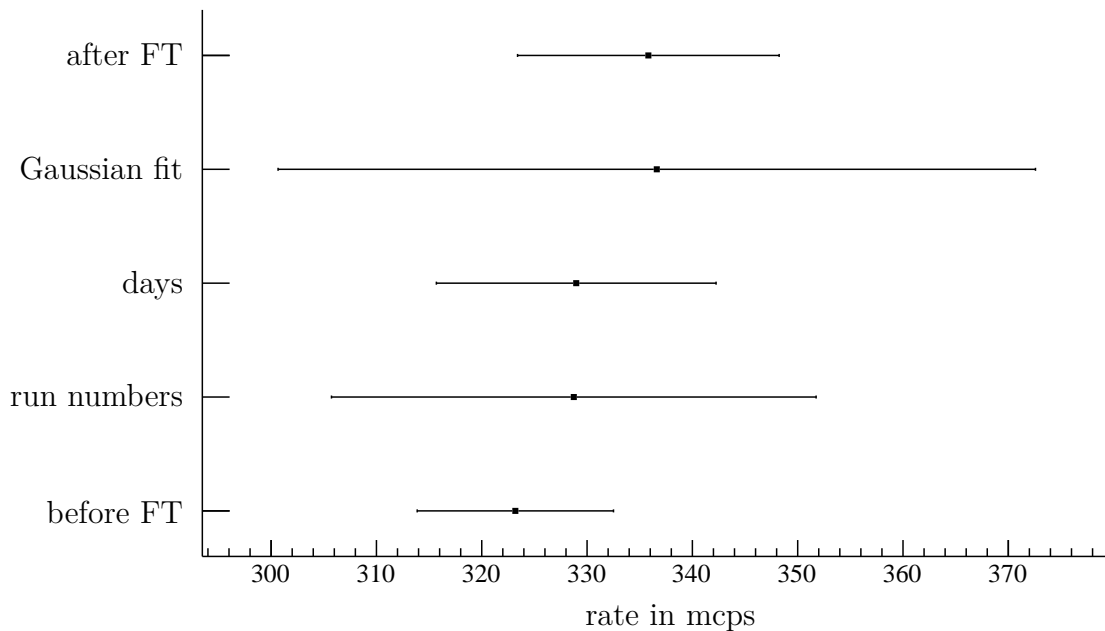


Figure 5.18.: Background rate results for different analyzing methods. The background rates and their standard deviation are shown in dependence of the corresponding analyzing method. See main text for details.

The clear demonstration of gas flow retention from the source system into the spectrometers enabled the first operation with tritium in the KATRIN beamline. In May 2018, the first tritium circulation started, which allowed to monitor the background rate to test for possible implantation of tritium into the spectrometers. A total amount of 420 TBq was circulated during the VFT and FT measurement campaigns. Two different aspects of this campaign were investigated within this thesis. First, the reduction factor of WGTS and DPS was analyzed using the activity stored on the CPS argon frost layer. With this approach, an overall reduction factor was measured to be of the required order of magnitude. As the TMP pumping speed is lower for DT and D₂ than for T₂, the reduction factor for nominal tritium operation will be larger.

Analyzing the background rate during and after FT revealed no indication for a drift which could potentially be credited to tritium entering the spectrometer section. Due to the trace amount of tritium in the circulated gas mixture, the sensitivity was limited. The rates obtained by different analysis approaches are summarized in figure 5.18. Nevertheless, the stable background rate confirms the operational readiness of the complete KATRIN beamline.

This chapter showed that the KATRIN transport and pumping section is ready for nominal tritium column density operation as in KATRIN neutrino mass configuration, starting in March 2019.

6. Summary and outlook

The discovery of neutrino oscillation was awarded with the Nobel prize in 2015. This prize underlines the importance of neutrinos in physics today. Despite their large abundance in the Universe, there are still several physical properties of neutrinos unknown. One of these parameters is the neutrino mass. There are several methods with which the neutrino mass can be measured, nonetheless no absolute value has been determined yet. The best limit for the sum of all neutrino masses can be derived from cosmological experiments. However, the analysis of these experiments is strongly model-dependent, which results in systematic dependencies. With another approach, namely the neutrinoless double beta decay, the neutrino mass can be measured if neutrinos are Majorana particles. But also those experiments have yet not found any value for a neutrino mass and report only upper limits. For model-independent measurements using the kinematics of the β -decay, the effective electron antineutrino mass is the observable.

With the tritium β -decay, the best results so far for an upper limit $m_{\nu_e} < 2.0$ eV (95% C.L.) have been found by the Mainz and Troitsk experiment. In this case, the advantage of the low endpoint energy of 18.6 keV, the relatively low half-life time of 12.3 years, and the super-allowed transition can be used in order to perform measurements with a high sensitivity. The KATRIN experiment located in Karlsruhe has the potential to improve the previous mass limit by one order of magnitude. As the actual observable is the effective electron antineutrino mass squared, the systematic uncertainties have to be reduced by a factor of 100.

In order to reach this ambitious goal, KATRIN consists of a 70 m long beamline, which guides the β -electrons adiabatically from the source on their way to the detector. In the WGTS, tritium decays with an activity of 10^{11} Bq providing a sufficient β -electron rate for the analysis of their energy by the MAC-E filter method. The tritium has to be pumped out before the spectrometer section since it would cause an irreproducible background component. For this purpose, the KATRIN transport and pumping section was designed combining turbomolecular pumps (TMPs) and a cryo pump with an argon frost layer.

In this thesis, the focus was set on the retention of neutral tritium preventing a contamination of the spectrometers. A retention of at least 14 orders of magnitude

is needed to keep the background level by tritium induced decays in the mHz level. The first differential pumping section (DPS) and cryogenic pumping section (CPS) commissioning measurements were done investigating the gas flow with non-active gases (D_2) through the components. The results of these measurements allowed the first operation of tritium in the KATRIN beamline during the First Tritium campaign in May 2018.

Before the measurements were started, dedicated and detailed simulations were made investigating the reduction factors of both pumping sections. The simulation results showed that the DPS reduction factor is right at the required level of five orders of magnitude. For the CPS, the temperature deviations to the nominal value of 3.0 K inside the cold trap were investigated first. With the simulation software COMSOL Multiphysics[®], a CPS cold trap temperature model was developed. The results indicated that the radiation of warmer CPS cryostat parts have a non-negligible effect on the beam tube temperature. Therefore, the designed homogeneous temperature distribution cannot be reached. In order to test the influence of the inhomogeneous temperature distribution on the pumping performance, two simulation models were constructed: one with MolFlow+ and a second semi-analytical tracking model. Both models achieved similar results: the CPS reduction factor exceeds the required reduction factor of 10^7 by several orders of magnitude. Additionally, the MolFlow+ simulation allowed to calculate ad-hoc factors for translating a measured pressure ratio into a reduction factor.

The results of the simulations were checked by the execution of the DPS and CPS commissioning measurements with deuterium. The sensitivity of the DPS measurements was limited due to the maximum flow rate at the entrance of the DPS beamline. Therefore, the designed reduction factor of 10^5 could not be confirmed by injecting deuterium into the WGTS. For the measurement of the CPS reduction factor, a dedicated inlet system had to be installed. This allowed the investigation of large inlet flows in a short measurement time. After first measurements with the golden inner beam tube surface of the cold trap, the first argon frost preparation was made. Similar to the measurements without the argon frost layer, both analysis showed a reduction factor larger than the requirement. The results were limited by the requirement of a molecular flow conditions and the sensitivity limit of the pressure gauges. With another measurement method, the reduction factor dependence on the temperature of the cold trap was investigated. Even though, from this method an absolute value for the reduction factor cannot be determined, the extrapolation yielded results in the order of 10^{12} to 10^{14} . The beginning of the First Tritium campaign allowed to check the influence of tritium on the spectrometer background. By comparing the background rates before, during, and after this campaign, no statistically significant increase of background could be found. The use of tritium also enabled to determine the combined reduction factor of WGTS and DPS, which showed to meet exactly the requirement. In general, the finding of this thesis is that the KATRIN pumping section meets its requirements.

In March 2019, the first KATRIN measurements with pure tritium were started. With the start of nominal tritium operation, the pumping sections remain an important part of the KATRIN experiment. The pumping of both sections has to be reliable in order to prevent tritium from entering the spectrometer. The developed argon frost preparation procedure allows reproducible conditions for the CPS cold

trap with their regular regeneration after 60 days of measurement time. The measurement results prove that the capacity of the CPS exceeds a 1 Ci limit by at least a factor of 100.

Within the next five years, KATRIN measurements will be performed with nominal tritium operation. The large collected dataset will allow to investigate the tritium background with a much better sensitivity. Together with a reduction of the non tritium induced background rate, a reduction factor larger than 10^{14} can then maybe stated. This is an integral part for the determination of the effective neutrino mass, which measured value would be an important milestone in neutrino physics.

Appendix

A. Measurement buffer vessel volume of argon inlet system

Table A.1.: Measurement buffer vessel argon inlet system. Measured values used for analysis in 3.2.5.2.

Measurement	p_0 in mbar	p_1 in mbar	p_2 in mbar
1	300	296	178
2	300	296	178
3	300	296	178

B. Measurement buffer vessel volume of deuterium inlet system

Table B.2.: Measurement buffer vessel deuterium inlet system. Measured values used for analysis in 5.1.2.1.1.

Measurement	p_0 in mbar	p_1 in mbar	p_2 in mbar
1	499.9	461.3	139.2
2	500.0	461.4	139.4
3	499.8	461.3	139.3

C. CPS loops piping and instrumentation diagram

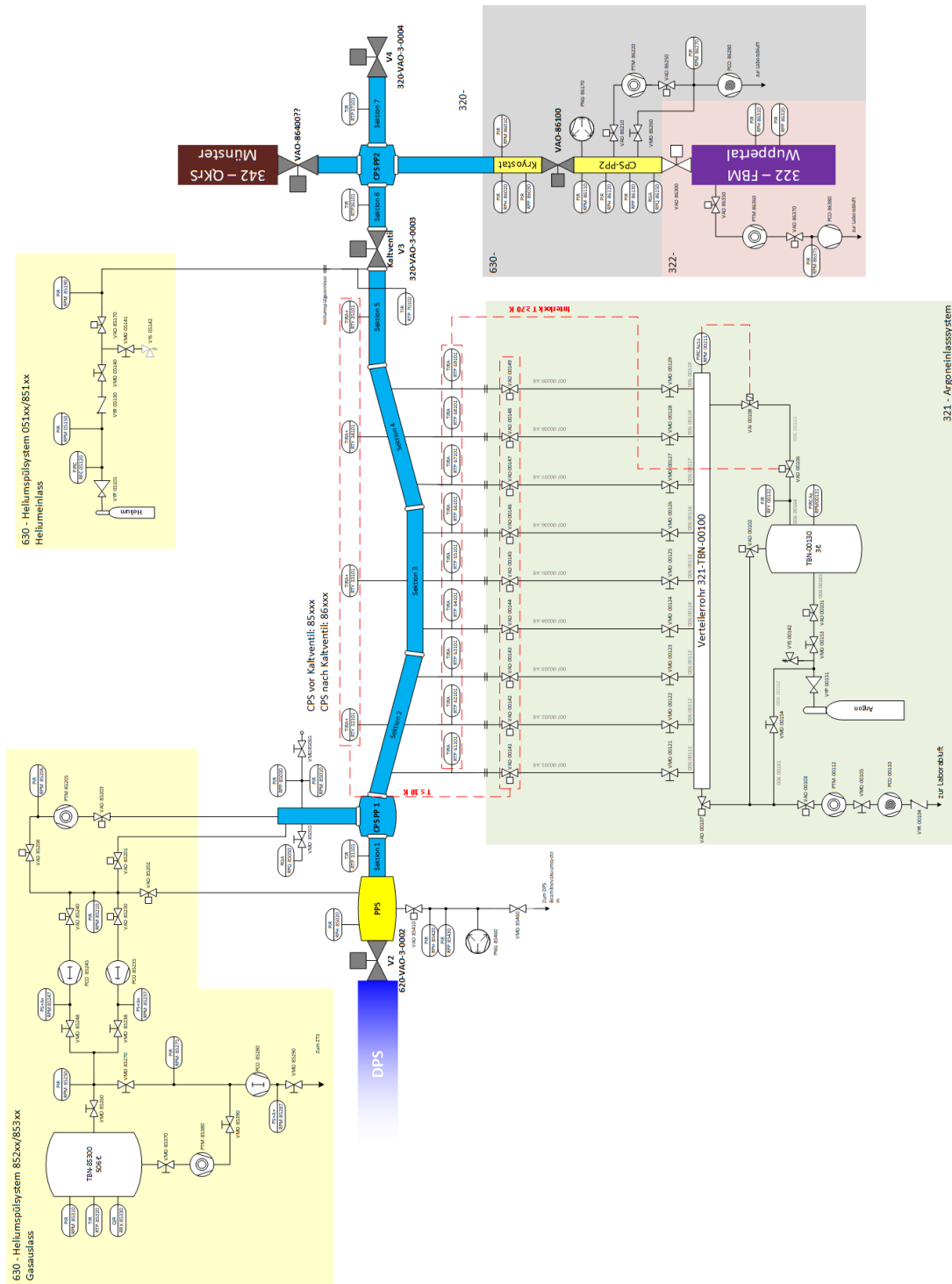


Figure C.1.: Piping and instrumentation (P&I) diagram of the CPS loops. The various components of the CPS loops are shown.

D. MAG W 2800 pumping speed

The pumping speed S of a MAG W 2800 can be estimated for a particular molar mass M by [Mal07]

$$S = S_{\text{H}_2} \cdot \sqrt{\frac{1}{M}} \cdot \frac{\log M}{\log 2} \quad (\text{D.1})$$

with the pumping speed S_{H_2} for hydrogen. In figure D.2, the resulting pumping speeds are shown

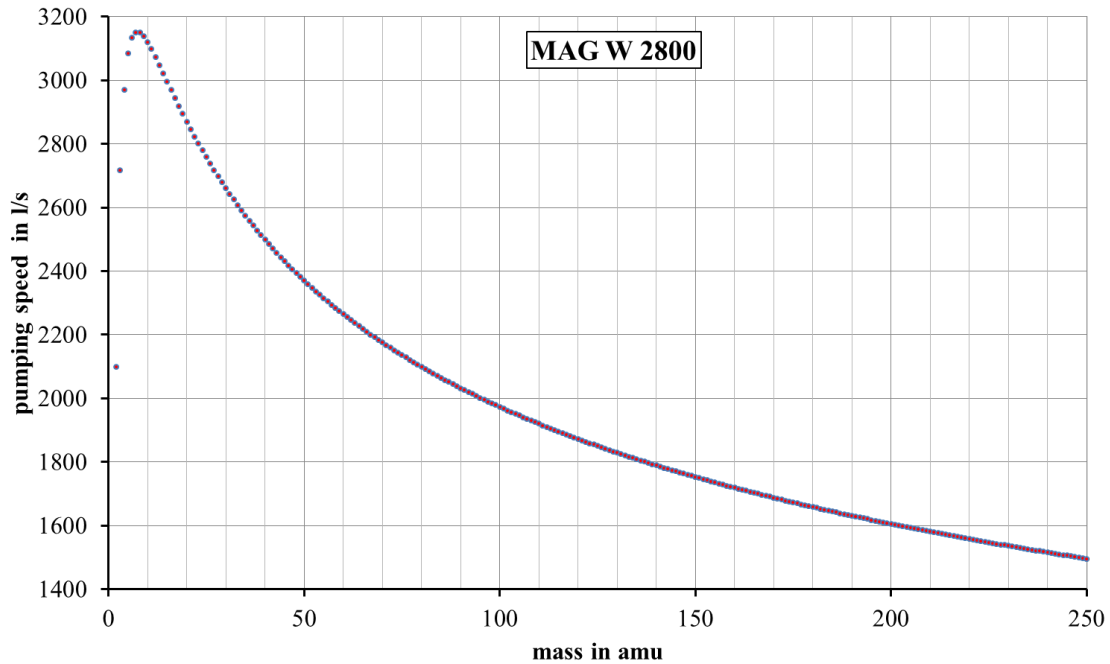


Figure D.2.: Pumping speed of MAG W 2800. The pumping speed of the MAG W 2800 is plotted over the molar mass of the pumped out gas.

F. Simulation of a hardware failure

In KATRIN standard operation, the flow into CPS is in the molecular flow range. In case there is a beam tube vacuum failure upstream of the DPS, a huge flow rate would impinge onto the spectrometer section, since this is the part with the lowest pressure. In such a case, a hardware interlock will be activated, where all beamline valves as well as the valves to the TMPs will be closed. However, the closing of beamline valves V2, V3, and V4 can take up to 15 s. With no TMPs available in this worst case scenario, the only working pump would be the CPS cryo trap. A temperature increase of the cold trap due the high flow rate can be neglected in this time range. In such an event, the incoming flow would not be in the molecular flow range, therefore the previous results (see section 5.1) might not be used for predictions.

In order to investigate a hypothetical vacuum failure, the deuterium inlet system was used. The worst case scenario includes coverage of the argon frost with a deuterium pV amount approximately equal to five times a 60 d run. In contrast to the previous measurements, the leak valve was fully opened for about 30 s. Because the measured conductance of the orifice is only valid in the molecular flow range, the injected flow cannot be determined. In addition, the pressure gauge at PP1 quickly went out of its range (the pressure was higher than 6.6×10^{-3} mbar) and therefore turned itself off to prevent damage of the cold cathode. The injected deuterium amount is therefore estimated from the difference in the buffer vessel pressure before and after deuterium injection. With the determined volume of the buffer vessel, a deuterium amount of

$$pV_{D_2, \text{fail}} = 157.52 \text{ mbar } \ell \quad (\text{F.1})$$

was injected. The tritium amount residing inside the WGTS will be approximately 0.125 mbar ℓ (the tritium gas in the rest of the beam line can be neglected), which is far less than the gas amount used. However, a vacuum failure might cause laboratory air to get into the beamline. In this case, most of the air gas components will freeze onto the cooled parts of WGTS and beam tube 1 of CPS, reducing the gas load onto the rest of the CPS beam tube.

Because of the unknown expectation, the RGA at PP2 was not turned on, having only the cold cathode to check for a pressure increase. During and after the injection, there was no change in either the temperature of the cold trap, or the pressure at PP2. Even for the approximately 1000 times larger pV amount compared to the tritium amount in WGTS and the 30 s injection time, the beam line valves would have enough time to close. In conclusion, the CPS cold trap acts as a safety device in case of a vacuum failure in the beam tube.

G. Run list first tritium background rate analysis

Table G.3.: Tritium β -scans. The runs all contain two background sub-runs with a measurement time of approximately 300s spent at a main spectrometer retarding potential of 18 595 V and 18 605 V.

Run number
40531
40538-40543
40603-40604
40610-40613
40666-40693
40763-40772
40794-40805
40926-40935
40976-40977
40979-40980
40982-40983
40985-40986
40988-40989
40991-40992
40994-40995
40997-40998
41001-41008
41010-41033

Table G.4.: Background runs before, during, and after first tritium. The runs are listed in dependence of the main spectrometer voltage, the pre-spectrometer voltage, and the V4 status.

Run number	MS voltage	PS voltage	V4 status
40218- 40222	18600	16400	closed
40366 - 40381	18600	16400	closed
40482 - 40486	18600	0	closed
40606 - 40608	19000	16400	closed
40975	18600	1000	open
40981	18600	1000	open
40984	18600	1000	open
40987	18600	1000	open
40990	18600	1000	open
40993	18600	1000	open
40996	18600	1000	open
41000	18600	ramping up	open
41078 - 41084	scanning	16400	close

List of Acronyms

- BIXS** Beta-Induced X-ray Spectroscopy
- CAD** Computer-Aided Design
- CERN** Conseil Européen pour la Recherche Nucléaire
- CDM** Cold Dark Matter
- CMB** Cosmic Microwave Background
- CPS** Cryogenic Pumping Section
- CUORE** Cryogenic Underground Observatory for Rare Events
- DPS** Differential Pumping Section
- ECHO** Electron Capture Holmium Experiment
- EXO** Enriched Xenon Observatory
- FBM** Forward Beam Monitor
- FT** First Tritium
- FT-ICR** Fourier-Transform Ion Cyclotron Resonance
- GERDA** Germanium Detector Array
- HOLMES** The Electron Capture Decay of Holmium-163 to Measure the Electron Neutrino Mass with sub-eV Sensitivity
- IMB** Irvine-Michigan-Brookhaven detector
- KamLAND-Zen** Kamioka Liquid Scintillator Antineutrino Detector - Zero-Neutrino double-beta decay experiment
- KATRIN** Karlsruhe Tritium Neutrino Experiment
- KIT** Karlsruher Institut für Technologie
- LARA** Laser Raman

- LEP** Large Electron Positron Collider
- MAC-E Filter** Magnetic Adiabatic Collimation combined with an Electrostatic Filter
- MARE** Microcalorimeter Arrays for a Rhenium Experiment
- NEG** Non-Evaporable Getter
- PP** Pump Port
- P&I** Piping and Instrumentation
- PULCINELLA** Precision Ultra-Low Current Integrating Normalization Electrometer for Low-Level Analysis
- RGA** Residual Gas Analyzer
- SDS** Spectrometer and Detector Section
- SM** Standard Model
- SNO** Sudbury Neutrino Observatory
- SQUID** Superconducting Quantum Interference Device
- STS** Source and Transport Section
- TMP** Turbomolecular pump
- VFT** Very First Tritium
- WGTS** Windowless Gaseous Tritium Source

List of Figures

1.1.	Inverse beta-decay detection	2
1.2.	Particles in the standard model	3
1.3.	SuperKamiokande result	8
1.4.	Neutrino mass hierarchy	10
1.5.	Neutrinoless double beta-decay spectrum	14
1.6.	Tritium β -spectrum	15
2.1.	KATRIN beam line	20
2.2.	WGTS cryostat with inner loop system	21
2.3.	Rear section	23
2.4.	DPS CAD drawing	25
2.5.	CPS cryostat	26
2.6.	MAC-E filter method	27
2.7.	KATRIN detector system set-up	31
2.8.	Background processes of the spectrometer and detector section	32
2.9.	Magnetically stored particle inside main spectrometer	33
2.10.	Muon-veto system	35
2.11.	Electron emission from radon decay	36
3.1.	Setup of the KATRIN loop system	40
3.2.	Piping and instrumentation (P&I) diagram of argon inlet system	45
3.3.	Experimental set-up for buffer vessel volume measurement	46
3.4.	Helium purging	49
4.1.	Model for DPS MolFlow+ simulation	53
4.2.	Temperature values of CPS cold trap	55
4.3.	Schematic draw of imported cold trap model	56
4.4.	Temperature deviation between measurement and simulation	58
4.5.	MolFlow+ model for CPS simulation	59
4.6.	Simulated CPS reduction factor with MolFlow+	63
4.7.	Simulated CPS pump port pressure ratio with MolFlow+	64
4.8.	Simulated CPS ad-hoc factors with MolFlow+	64
4.9.	Simulated CPS reduction factor for different desorption energies with MolFlow+	65
4.10.	Histograms for semi-analytical tracking method	67
4.11.	Simulated cold trap coverage	68
4.12.	Mean surface density of CPS cold trap	69
4.13.	Simulated CPS reduction factor with tritium β -decay	70
4.14.	Comparison of MolFlow+ and semi-analytical tracking model	71

5.1.	DPS reduction factor measurement	75
5.2.	P&I diagram and photograph of deuterium inlet system	79
5.3.	Helium injection into the CPS	80
5.4.	CPS regeneration	82
5.5.	Calibration of the RGA at CPS-PP2	83
5.6.	CPS D ₂ reduction factor measurement on gold surface	84
5.7.	Reduction factor measurement of gold surface with RGA	86
5.8.	Argon frost reduction factor measurement with a constant injection flow	87
5.9.	Long time argon frost reduction factor measurement	88
5.10.	Temperature dependent reduction factor measurement with argon frost	90
5.11.	Extrapolation of CPS reduction with an argon frost layer	91
5.12.	Temperature dependent reduction factor measurement without argon frost layer	92
5.13.	Extrapolation of CPS reduction without argon frost layer	93
5.14.	Pixel map of the FPD for the background runs	97
5.15.	Background rate trend during tritium measurements	98
5.16.	Background rate development over tritium campaign days	99
5.17.	Background rate histogram for tritium measurement campaign	101
5.18.	Background rate results for different analyzing methods	103
C.1.	Piping and instrumentation (P&I) diagram of the CPS loops	111
D.2.	Pumping speed of MAG W 2800	112
E.3.	CPS beam tube temperature sensors	113

List of Tables

1.1. Measured values for the neutrino oscillation parameters	9
3.1. Conductances of argon capillaries	48
3.2. Argon preparation pressures	49
4.1. DPS tritium reduction factor simulation	53
4.2. DPS deuterium reduction factor simulation	54
4.3. CPS reduction factors for different isotopologues	69
5.1. Summary of CPS reduction factor measurements.	94
A.1. Measurement buffer vessel argon inlet system	110
B.2. Measurement buffer vessel deuterium inlet system	110
G.3. Tritium β -scans	115
G.4. Background runs before, during, and after first tritium	115

Bibliography

- [A⁺13] B. Aharmim et al. Combined analysis of all three phases of solar neutrino data from the sudbury neutrino observatory. *Physical Review C*, 88:025501, 2013. doi:10.1103/PhysRevC.88.025501.
- [A⁺14] J. B. Albert et al. Search for Majorana neutrinos with the first two years of EXO-200 data. *Nature*, 510:229–234, 2014, 1402.6956. doi:10.1038/nature13432.
- [A⁺18a] N. Aghanim et al. Planck 2018 results. VI. Cosmological parameters. 2018, 1807.06209.
- [A⁺18b] M. Arenz et al. Calibration of high voltages at the ppm level by the difference of ^{83m}Kr conversion electron lines at the KATRIN experiment. *The European Physical Journal C*, 78(5):368, 2018. doi:10.1140/epjc/s10052-018-5832-y.
- [A⁺18c] M. Arenz et al. First transmission of electrons and ions through the KATRIN beamline. *Journal of Instrumentation*, 13(04):P04020, 2018. doi:10.1088/1748-0221/13/04/P04020.
- [A⁺18d] M. Arenz et al. The KATRIN superconducting magnets: Overview and first performance results. *Journal of Instrumentation*, 13(08):T08005, 2018. doi:10.1088/1748-0221/13/08/T08005.
- [A⁺19] K. Altenmüller et al. Gamma-induced background in the KATRIN main spectrometer. 2019, 1903.00563.
- [AAA⁺12] G. Aad, T. Abajyan, B. Abbott, et al. Observation of a new particle in the search for the standard model higgs boson with the atlas detector at the lhc. *Physics Letters B*, 716(1):1 – 29, 2012. doi:https://doi.org/10.1016/j.physletb.2012.08.020.
- [AAA⁺16] Fengpeng An, Guangpeng An, Qi An, et al. Neutrino physics with JUNO. *Journal of Physics G: Nuclear and Particle Physics*, 43(3):030401, feb 2016. doi:10.1088/0954-3899/43/3/030401.
- [AAA⁺18a] C. E. Aalseth, N. Abgrall, E. Aguayo, et al. Search for neutrinoless double- β decay in ⁷⁶Ge with the majorana demonstrator. *Phys. Rev. Lett.*, 120:132502, Mar 2018. doi:10.1103/PhysRevLett.120.132502.
- [AAA⁺18b] C. Alduino, K. Alfonso, D. R. Artusa, et al. Search for neutrinoless β^+ EC decay of ¹²⁰Te with cuore-0. *Phys. Rev. C*, 97:055502, May 2018. doi:10.1103/PhysRevC.97.055502.

- [AAB⁺19] K. Altenmüller, M. Arenz, W.-J. Baek, et al. Muon-induced background in the katrin main spectrometer. *Astroparticle Physics*, 108:40 – 49, 2019. doi:<https://doi.org/10.1016/j.astropartphys.2019.01.003>.
- [ABB⁺11] V. N. Aseev, A. I. Belesev, A. I. Berlev, et al. Upper limit on the electron antineutrino mass from the Troitsk experiment. *Physical Review D*, 84:112003, 2011. doi:10.1103/PhysRevD.84.112003.
- [ABB⁺15] J.F. Amsbaugh, J. Barrett, A. Beglarian, et al. Focal-plane detector system for the KATRIN experiment. *Nuclear Instruments and Methods in Physics Research Section A: Accelerators, Spectrometers, Detectors and Associated Equipment*, 778:40–60, 2015. doi:10.1016/j.nima.2014.12.116.
- [ABB⁺16] M. Arenz, M. Babutzka, M. Bahr, et al. Commissioning of the vacuum system of the KATRIN main spectrometer. *Journal of Instrumentation*, 11:P04011, 2016, 1603.01014. doi:10.1088/1748-0221/11/04/P04011.
- [ABB⁺17] F. P. An, A. B. Balantekin, H. R. Band, et al. Measurement of electron antineutrino oscillation based on 1230 days of operation of the daya bay experiment. *Phys. Rev. D*, 95:072006, Apr 2017. doi:10.1103/PhysRevD.95.072006.
- [ABB⁺18] M. Agostini, A. M. Bakalyarov, M. Balata, et al. Improved limit on neutrinoless double- β decay of ^{76}Ge from gerda phase ii. *Phys. Rev. Lett.*, 120:132503, Mar 2018. doi:10.1103/PhysRevLett.120.132503.
- [ABBW03] G. Audi, O. Bersillon, J. Blachot, and A.H. Wapstra. The nubase evaluation of nuclear and decay properties. *Nuclear Physics A*, 729(1):3 – 128, 2003. doi:<https://doi.org/10.1016/j.nuclphysa.2003.11.001>. The 2003 NUBASE and Atomic Mass Evaluations.
- [ABD⁺96] K. Assamagan, Ch. Brönnimann, M. Daum, et al. Upper limit of the muon-neutrino mass and charged-pion mass from momentum analysis of a surface muon beam. *Phys. Rev. D*, 53:6065–6077, Jun 1996. doi:10.1103/PhysRevD.53.6065.
- [AS79] H. Abe and W. Schulze. The sorption capacity of solid rare gas layers. *Chemical Physics*, 41(3):257 – 263, 1979. doi:[https://doi.org/10.1016/0301-0104\(79\)80032-4](https://doi.org/10.1016/0301-0104(79)80032-4).
- [Bab14] Martin Babutzka. *Design and development for the Rearsection of the KATRIN experiment*. PhD thesis, Karlsruher Institut für Technologie (KIT), 2014. doi:10.5445/IR/1000045598.
- [Bah64] John N. Bahcall. Solar neutrino cross sections and nuclear beta decay. *Phys. Rev.*, 135:B137–B146, Jul 1964. doi:10.1103/PhysRev.135.B137.
- [BBB⁺87] R. M. Bionta, G. Blewitt, C. B. Bratton, et al. Observation of a neutrino burst in coincidence with supernova 1987a in the

- large magellanic cloud. *Phys. Rev. Lett.*, 58:1494–1496, Apr 1987. doi:10.1103/PhysRevLett.58.1494.
- [BBB⁺12] M. Babutzka, M. Bahr, J. Bonn, et al. Monitoring of the operating parameters of the KATRIN windowless gaseous tritium source. *New Journal of Physics*, 14(10):103046, 2012. doi:10.1088/1367-2630/14/10/103046.
- [BBD⁺98] R Barate, Damir Buskucic, D Décamp, et al. An upper limit on the τ neutrino mass from three- and five-prong tau decays. *European Physical Journal C*, 2, 04 1998. doi:10.1007/s100520050149.
- [Beh16] Jan D. Behrens. *Design and commissioning of a mono-energetic photoelectron source and active background reduction by magnetic pulse at the KATRIN spectrometers*. PhD thesis, Westfälische Wilhelms-Universität Münster, 2016. URL http://www.katrin.kit.edu/publikationen/phd_behrens.pdf.
- [BLS⁺72] J Boardman, P Lynam, R.G. Scurlock, et al. International cryogenic engineering conference, 4th, icec4, proceedings. 05 1972.
- [BPT80] G. Beamson, H. Q. Porter, and D. W. Turner. The collimating and magnifying properties of a superconducting field photoelectron spectrometer. *Journal of Physics E: Scientific Instruments*, 13(1):64, 1980. doi:10.1088/0022-3735/13/1/018.
- [BRB⁺17] J. Behrens, P. C.-O. Ranitzsch, M. Beck, et al. A pulsed, mono-energetic and angular-selective UV photo-electron source for the commissioning of the KATRIN experiment. *The European Physical Journal C*, 77(6):410, 2017. doi:10.1140/epjc/s10052-017-4972-9.
- [BS57] H.A. Bethe and E.E. Salpeter. *Quantum Mechanics of One- and Two-Electron Atoms*. Oxford Master Series in Physics. Springer, 1957. doi:10.1007/978-3-662-12869-5.
- [CCC⁺16] J. H. Choi, W. Q. Choi, Y. Choi, et al. Observation of energy and baseline dependent reactor antineutrino disappearance in the reno experiment. *Phys. Rev. Lett.*, 116:211801, May 2016. doi:10.1103/PhysRevLett.116.211801.
- [CKSea12] S. Chatrchyan, V. Khachatryan, A.M. Sirunyan, and A. Tumasyan et al. Observation of a new boson at a mass of 125 gev with the cms experiment at the lhc. *Physics Letters B*, 716(1):30 – 61, 2012. doi:<https://doi.org/10.1016/j.physletb.2012.08.021>.
- [Coo] N.G. Cooper. Los alamos science, number 25 – 1997: Celebrating the neutrino. doi:10.2172/569122.
- [D⁺89] D. Decamp et al. Determination of the number of light neutrino species. *Physics Letters B*, 231:519, 1989. doi:10.1016/0370-2693(89)90704-1.
- [Dav94] R. Davis. A review of the Homestake solar neutrino experiment. *Prog. Part. Nucl. Phys.*, 32:13–32, 1994. doi:10.1016/0146-6410(94)90004-3.

- [DGG⁺62] G. Danby, J-M. Gaillard, K. Goulianos, et al. Observation of high-energy neutrino reactions and the existence of two kinds of neutrinos. *Phys. Rev. Lett.*, 9:36–44, Jul 1962. doi:10.1103/PhysRevLett.9.36.
- [DHCK⁺17] Mona Dentler, Álvaro Hernández-Cabezudo, Joachim Kopp, Michele Maltoni, and Thomas Schwetz. Sterile neutrinos or flux uncertainties? — status of the reactor anti-neutrino anomaly. *Journal of High Energy Physics*, 2017(11):99, Nov 2017. doi:10.1007/JHEP11(2017)099.
- [DHMW13] G. Drexlin, V. Hannen, S. Mertens, and C. Weinheimer. Current direct neutrino mass experiments. *Advances in High Energy Physics*, 2013, 2013. doi:10.1155/2013/293986.
- [DJ57] E R Dobbs and G O Jones. Theory and properties of solid argon. *Reports on Progress in Physics*, 20(1):516–564, jan 1957. doi:10.1088/0034-4885/20/1/309.
- [EB64] F. Englert and R. Brout. Broken symmetry and the mass of gauge vector mesons. *Phys. Rev. Lett.*, 13:321–323, Aug 1964. doi:10.1103/PhysRevLett.13.321.
- [EBB⁺08] F. Eichelhardt, B. Bornschein, L. Bornschein, et al. First tritium results of the KATRIN test experiment trap. *Fusion Science and Technology*, 54(2):615–618, 2008. URL http://www.new.ans.org/pubs/journals/fst/a_1890.
- [EBB⁺14] M. Erhard, S. Bauer, A. Beglarian, et al. High-voltage monitoring with a solenoid retarding spectrometer at the KATRIN experiment. *Journal of Instrumentation*, 9(6):P06022, 2014. doi:10.1088/1748-0221/9/06/P06022.
- [EBB⁺15] S. Eliseev, K. Blaum, M. Block, et al. Direct measurement of the mass difference of ¹⁶³Ho and ¹⁶³Dy solves the q -value puzzle for the neutrino mass determination. *Phys. Rev. Lett.*, 115:062501, Aug 2015. doi:10.1103/PhysRevLett.115.062501.
- [EG06] The ALEPH CollaborationThe DELPHI CollaborationThe L3 CollaborationThe OPAL CollaborationThe SLD CollaborationThe LEP Electroweak Working GroupThe SLD Electroweak and Heavy Flavour Groups. Precision electroweak measurements on the z resonance. *Physics Reports*, 427(5):257 – 454, 2006. doi:<https://doi.org/10.1016/j.physrep.2005.12.006>.
- [Eic09] Frank Eichelhardt. *Measurement of the Tritium Pumping Properties of a 4.2 K Argon Condensate for the Cryogenic Pumping Section of KATRIN*. PhD thesis, Universität Karlsruhe (TH), 2009. doi:10.5445/IR/1000010434.
- [Erh16] Moritz G. Erhard. *Influence of the magnetic field on the transmission characteristics and neutrino mass systematic of the KATRIN experiment*. PhD thesis, Karlsruher Institut für Technologie (KIT), 2016. doi:10.5445/IR/1000065003.

- [FBD⁺11] F.M. Fränkle, L. Bornschein, G. Drexlin, et al. Radon induced background processes in the KATRIN pre-spectrometer. *Astroparticle Physics*, 35(3):128–134, 2011. doi:10.1016/j.astropartphys.2011.06.009.
- [Fer34] E. Fermi. Versuch einer theorie der β -Strahlen. *Zeitschrift für Physik*, 88(3–4):161–177, 1934. doi:10.1007/BF01351864.
- [FGV⁺14] F.M. Fränkle, F. Glück, K. Valerius, et al. Penning discharge in the KATRIN pre-spectrometer. *Journal of Instrumentation*, 9(7):P07028, 2014. doi:10.1088/1748-0221/9/07/P07028.
- [FHI⁺98] Y. Fukuda, T. Hayakawa, E. Ichihara, et al. Evidence for oscillation of atmospheric neutrinos. *Phys. Rev. Lett.*, 81:1562–1567, Aug 1998. doi:10.1103/PhysRevLett.81.1562.
- [Fis14] Sebastian Fischer. *Commissioning of the KATRIN Raman system and durability studies of optical coatings in glove box and tritium atmospheres*. PhD thesis, Karlsruher Institut für Technologie (KIT), 2014. doi:10.5445/IR/1000043697.
- [FMO82] G. Falcone, D. Matragnano, and A. Oliva. Energy distribution of sputtered excited atoms. *Lettere al Nuovo Cimento (1971-1985)*, 35(16):465–468, Dec 1982. doi:10.1007/BF02817286.
- [Frä10] Florian M. Fränkle. *Background Investigations of the KATRIN Pre-Spectrometer*. PhD thesis, Karlsruher Institut für Technologie (KIT), 2010. doi:10.5445/IR/1000019392.
- [Fra17] F. M. Fraenkle. Background processes in the KATRIN main spectrometer. *Journal of Physics: Conference Series*, 888(1):012070, 2017. doi:10.1088/1742-6596/888/1/012070.
- [Fri17] Fabian Friedel. Studien zur Inbetriebnahme der kryogenen Pumpstrecke des KATRIN-Experiments. Master thesis, Karlsruher Institut für Technologie (KIT), 2017.
- [FRS⁺19] F. Friedel, C. Röttele, L. Schimpf, et al. Time-dependent simulation of the flow reduction of d_2 and t_2 in the KATRIN experiment. *Vacuum*, 159:161 – 172, 2019. doi:10.1016/j.vacuum.2018.10.002.
- [FSS⁺11] S. Fischer, M. Sturm, M. Schlösser, et al. Monitoring of tritium purity during long-term circulation in the KATRIN test experiment LOOPINO using laser Raman spectroscopy. *Fusion Science and Technology*, 60(3):925–930, 2011. URL http://www.ans.org/pubs/journals/fst/a_12567.
- [Fur39] W. H. Furry. On transition probabilities in double beta-disintegration. *Phys. Rev.*, 56:1184–1193, Dec 1939. doi:10.1103/PhysRev.56.1184.
- [GBC⁺17] L. Gastaldo, K. Blaum, K. Chrysalidis, et al. The electron capture in 163ho experiment – echo. *The European Physical Journal Special Topics*, 226(8):1623–1694, Jun 2017. doi:10.1140/epjst/e2017-70071-y.

- [GBH⁺13] S. Grohmann, T. Bode, M. Hötzel, et al. The thermal behaviour of the tritium source in KATRIN. *Cryogenics*, 55-56(0):5–11, 2013. doi:10.1016/j.cryogenics.2013.01.001.
- [GBSS11] S. Grohmann, T. Bode, H. Schön, and M. Süßer. Precise temperature measurement at 30 K in the KATRIN source cryostat. *Cryogenics*, 51(8):438–445, 2011. doi:10.1016/j.cryogenics.2011.05.001.
- [GGH⁺16] A. Gando, Y. Gando, T. Hachiya, et al. Search for majorana neutrinos near the inverted mass hierarchy region with kamland-zen. *Phys. Rev. Lett.*, 117:082503, Aug 2016. doi:10.1103/PhysRevLett.117.082503.
- [GGS58] M. Goldhaber, L. Grodzins, and A. W. Sunyar. Helicity of neutrinos. *Phys. Rev.*, 109:1015–1017, Feb 1958. doi:10.1103/PhysRev.109.1015.
- [GJBG⁺08] S. Grohmann, B. Bornschein J. Bonn, R. Gehring, et al. Cryogenic design of the KATRIN source cryostat. *AIP Conference Proceedings*, 985:1277–1284, 2008. doi:10.1063/1.2908483.
- [GLW57] R. L. Garwin, L. M. Lederman, and Marcel Weinrich. Observations of the Failure of Conservation of Parity and Charge Conjugation in Meson Decays: The Magnetic Moment of the Free Muon. *Physical Review*, 105:1415–1417, 1957. doi:10.1103/PhysRev.105.1415.
- [GM35] M. Goeppert-Mayer. Double beta-disintegration. *Phys. Rev.*, 48:512–516, Sep 1935. doi:10.1103/PhysRev.48.512.
- [GMRS79] Murray Gell-Mann, Pierre Ramond, and Richard Slansky. Complex Spinors and Unified Theories. *Conf. Proc.*, C790927:315–321, 1979, 1306.4669.
- [Gör14] Stefan Görhardt. *Background Reduction Methods and Vacuum Technology at the KATRIN Spectrometers*. PhD thesis, Karlsruher Institut für Technologie (KIT), 2014. doi:10.5445/IR/1000038050.
- [Gre02] John Greenwood. The correct and incorrect generation of a cosine distribution of scattered particles for Monte-Carlo modelling of vacuum systems. *Vacuum*, 67(2):217–222, Sep 2002. doi:10.1016/s0042-207x(02)00173-2.
- [Gro09] S. Grohmann. Stability analyses of the beam tube cooling system in the KATRIN source cryostat. *Cryogenics*, 49(8):413–420, 2009. doi:10.1016/j.cryogenics.2009.06.001.
- [Gro15] Stefan Groh. *Modeling of the response function and measurement of transmission properties of the KATRIN experiment*. PhD thesis, Karlsruher Institut für Technologie (KIT), 2015. doi:10.5445/IR/1000046546.
- [Hac17] Moritz Thomas Hackenjös. *KATRIN "First Light" - Commissioning and Modelling of the Beamline*. PhD thesis, Karlsruher Institut für Technologie (KIT), 2017. doi:10.5445/IR/1000078933.

- [Hae81] R.A. Haefer. *Kryo-Vakuumtechnik*. Oxford Master Series in Physics. Springer, 1981. doi:10.1007/978-3-642-49985-2.
- [Har15] Fabian Harms. *Characterization and Minimization of Background Processes in the KATRIN Main Spectrometer*. PhD thesis, Karlsruher Institut für Technologie (KIT), 2015. doi:10.5445/IR/1000050027.
- [Hei15] Florian Heizmann. Optimization of a KATRIN source analysis tool and investigations of the potential to constrain the relic neutrino background. Master thesis, Karlsruher Institut für Technologie (KIT), 2015. URL http://www.katrin.kit.edu/publikationen/mth_heizmann.pdf.
- [Hei18] Johannes Heizmann. Application of machine learning algorithms for improved background characterization at the KATRIN experiment. Master thesis, Karlsruher Institut für Technologie (KIT), 2018. URL <http://www.katrin.kit.edu/publikationen/mth-heizmannj.pdf>.
- [Hei19] Florian Heizmann. *Analysis tools and methods for tritium data taking with the KATRIN experiment*. PhD thesis, Karlsruher Institut für Technologie (KIT), 2019. doi:10.5445/IR/1000093536.
- [HHW⁺17] V. Hannen, I. Heese, C. Weinheimer, A. Sejersen Riis, and K. Valerius. Deconvolution of the energy loss function of the KATRIN experiment. *Astroparticle Physics*, 89:30 – 38, 2017. doi:10.1016/j.astropartphys.2017.01.010.
- [Hig64] Peter W. Higgs. Broken symmetries and the masses of gauge bosons. *Phys. Rev. Lett.*, 13:508–509, Oct 1964. doi:10.1103/PhysRevLett.13.508.
- [Hil16] Daniel F. R. Hilke. *Electric field simulations and electric dipole investigations at the KATRIN main spectrometer*. PhD thesis, Karlsruher Institut für Technologie (KIT), 2016. doi:10.5445/IR/1000065869.
- [Hin18] Dominic Hinz. Ionisation mechanisms of ^{206}Pb induced Rydberg atoms. Master thesis, Karlsruher Institut für Technologie (KIT), 2018. URL <http://www.katrin.kit.edu/publikationen/mth-hinz.pdf>.
- [HKK⁺88] K.S. Hirata, T. Kajita, M. Koshiba, et al. Experimental study of the atmospheric neutrino flux. *Physics Letters B*, 205(2):416 – 420, 1988. doi:[https://doi.org/10.1016/0370-2693\(88\)91690-5](https://doi.org/10.1016/0370-2693(88)91690-5).
- [Jac99] John David Jackson. *Classical electrodynamics*. Wiley, New York, 3. ed. edition, 1999.
- [Jan15] Alexander Jansen. *The Cryogenic Pumping Section of the KATRIN Experiment - Design Studies and Experiments for the Commissioning*. PhD thesis, Karlsruher Institut für Technologie (KIT), 2015. doi:10.5445/IR/1000047146.

- [JBD67] K.C. Jordan, B.C. Blanke, and W.A. Dudley. Half-life of tritium. *Journal of Inorganic and Nuclear Chemistry*, 29(9):2129 – 2131, 1967. doi:[https://doi.org/10.1016/0022-1902\(67\)80265-3](https://doi.org/10.1016/0022-1902(67)80265-3).
- [JOHW55] C. F. Curtiss J. O. Hirschfelder and R. B. Bird. Wiley. Molecular theory of gases and liquids. *Journal of Polymer Science*, 17(83):116–116, 1955, <https://onlinelibrary.wiley.com/doi/pdf/10.1002/pol.1955.120178311>. doi:10.1002/pol.1955.120178311.
- [Jou08] K. Jousten. *Handbook of Vacuum Technology*. John Wiley & Sons, 2008.
- [KA14] R. Kersevan and M. Ady. Molflow+ user guide, 2014. URL <http://molflow.web.cern.ch/>.
- [KAT05] KATRIN collaboration. KATRIN design report. FZKA scientific report 7090, 2005. URL <http://bibliothek.fzk.de/zb/berichte/FZKA7090.pdf>.
- [KBB⁺05] C. Kraus, B. Bornschein, L. Bornschein, et al. Final results from phase II of the mainz neutrino mass search in tritium β decay. *The European Physical Journal C*, 40(4):447–468, 2005. doi:10.1140/epjc/s2005-02139-7.
- [KBD⁺18] M. Kleesiek, J. Behrens, G. Drexlin, et al. β -decay spectrum, response function and statistical model for neutrino mass measurements with the KATRIN experiment. *Submitted to Eur. Phys. J. C.*, 2018, 1806.00369. URL <https://arxiv.org/abs/1806.00369>. In review.
- [KBK⁺08] O. Kazachenko, B. Bornschein, N. Kernert, et al. Tritium processing loop for KATRIN experiment. *Fusion Science and Technology*, 54(1):67–70, 2008. URL http://www.ans.org/pubs/journals/fst/a_1766.
- [Kel82] Roger Kelly. On the origin of sputtered excited atoms. *Nuclear Instruments and Methods in Physics Research*, 194(1):583 – 588, 1982. doi:[https://doi.org/10.1016/0029-554X\(82\)90585-7](https://doi.org/10.1016/0029-554X(82)90585-7).
- [KHD⁺18] L. Kuckert, F. Heizmann, G. Drexlin, et al. Modelling of gas dynamical properties of the KATRIN tritium source and implications for the neutrino mass measurement. *Vacuum*, 158:195–205, 2018. doi:10.1016/j.vacuum.2018.09.036.
- [KKL⁺17] Bartosz Kolodziej, A Kowal, L Lipinski, H Manuszkiewicz, and A Szymrka-Grzebyk. Comparison of the argon triple-point temperature in small cells of different construction. *International Journal of Thermophysics*, 38:94, 03 2017. doi:10.1007/s10765-017-2225-7.
- [Kle19] Manuel Klein. *Tritium ions in KATRIN: blocking, removal and detection*. PhD thesis, Karlsruher Institut für Technologie (KIT), 2019. doi:10.5445/IR/1000093526. 51.03.01; LK 01.

- [KM69] T. Kirsten and H.W. Müller. Observation of ^{82}Se double-beta decay in selenium ores. *Earth and Planetary Science Letters*, 6(4):271 – 274, 1969. doi:[https://doi.org/10.1016/0012-821X\(69\)90167-8](https://doi.org/10.1016/0012-821X(69)90167-8).
- [KM73] Makoto Kobayashi and Toshihide Maskawa. CP-Violation in the Renormalizable Theory of Weak Interaction. *Progress of Theoretical Physics*, 49(2):652–657, 02 1973, <http://oup.prod.sis.lan/ptp/article-pdf/49/2/652/5257692/49-2-652.pdf>. doi:10.1143/PTP.49.652.
- [Kna62] W. Knauer. Mechanism of the penning discharge at low pressures. *Journal of Applied Physics*, 33(6):2093–2099, 1962, <https://doi.org/10.1063/1.1728902>. doi:10.1063/1.1728902.
- [Kos12] Andreas Kosmider. *Tritium Retention Techniques in the KATRIN Transport Section and Commissioning of its DPS2-F Cryostat*. PhD thesis, Karlsruher Institut für Technologie (KIT), 2012. doi:10.5445/IR/1000028959.
- [Kra16] Marcel Kraus. *Energy-scale systematics at the KATRIN main spectrometer*. PhD thesis, Karlsruher Institut für Technologie (KIT), 2016. doi:10.5445/IR/1000054447.
- [KS52] O. Knacke and I. N. Stranski. Die theorie des kristallwachstums. In *Ergebnisse der Exakten Naturwissenschaften*, pages 383–427, Berlin, Heidelberg, 1952. Springer Berlin Heidelberg.
- [KUA⁺01] K. Kodama, N. Ushida, C. Andreopoulos, et al. Observation of tau neutrino interactions. *Physics Letters B*, 504(3):218 – 224, 2001. doi:[https://doi.org/10.1016/S0370-2693\(01\)00307-0](https://doi.org/10.1016/S0370-2693(01)00307-0).
- [Kuc16] Laura Kuckert. *The Windowless Gaseous Tritium Source of the KATRIN Experiment – Characterisation of Gas Dynamical and Plasma Properties*. PhD thesis, Karlsruher Institut für Technologie (KIT), 2016. doi:10.5445/IR/1000065077.
- [LD08] X. Luo and C. Day. Test particle monte carlo study of the cryogenic pumping system of the karlsruhe tritium neutrino experiment. *Journal of Vacuum Science & Technology A*, 26(5):1319–1325, 2008. doi:10.1116/1.2956628.
- [Lei14] Benjamin Leiber. *Investigations of background due to secondary electron emission in the KATRIN-experiment*. PhD thesis, Karlsruher Institut für Technologie (KIT), 2014. doi:10.5445/IR/1000042415.
- [Ley18] Leybold. Vacuum Measuring, Controlling. Brochure, 2018. https://www.leyboldproducts.de/media/pdf/1f/aa/cb/CP_060_Vacuum_Measuring_Controlling_EN.pdf.
- [LL02] Thomas J. Loredo and Donald Q. Lamb. Bayesian analysis of neutrinos observed from supernova sn 1987a. *Phys. Rev. D*, 65:063002, Feb 2002. doi:10.1103/PhysRevD.65.063002.

- [LP12] Julien Lesgourgues and Sergio Pastor. Neutrino mass from Cosmology. *Adv. High Energy Phys.*, 2012:608515, 2012, 1212.6154. doi:10.1155/2012/608515.
- [LS85a] V. M. Lobashev and P. E. Spivak. A method for measuring the electron antineutrino rest mass. *Nuclear Instruments and Methods in Physics Research Section A: Accelerators, Spectrometers, Detectors and Associated Equipment*, 240(2):305–310, 1985. doi:10.1016/0168-9002(85)90640-0.
- [LS85b] V.M. Lobashev and P.E. Spivak. A method for measuring the electron antineutrino rest mass. *Nuclear Instruments and Methods in Physics Research Section A: Accelerators, Spectrometers, Detectors and Associated Equipment*, 240:305–310, 10 1985. doi:10.1016/0168-9002(85)90640-0.
- [LV11] Maurizio Lusignoli and Marco Vignati. Relic Antineutrino Capture on 163-Ho decaying Nuclei. *Phys. Lett.*, B697:11–14, 2011, 1012.0760. doi:10.1016/j.physletb.2011.01.047, 10.1016/j.physletb.2011.06.008. [Erratum: *Phys. Lett.*B701,673(2011)].
- [Mal07] Oleg B. Malyshev. Characterisation of turbo-molecular pumps by a minimum of parameters. *Vacuum*, 81(6):752–758, feb 2007. doi:10.1016/j.vacuum.2005.11.055.
- [Mal08] Oleg B. Malyshev. Tritium migration along the cryopumping section. *Journal of Vacuum Science & Technology A: Vacuum, Surfaces, and Films*, 26(1):68, 2008. doi:10.1116/1.2816945.
- [Mar17] Alexander Marsteller. Measurement of Temperature Stability and Homogeneity of the KATRIN WGTS Cryostat. Master thesis, Karlsruher Institut für Technologie (KIT), 2017. URL https://www.katrin.kit.edu/publikationen/mth_marsteller.pdf.
- [MBB⁺12] S. Mertens, A. Beglarian, L. Bornschein, et al. Stochastic heating by ECR as a novel means of background reduction in the KATRIN spectrometers. *Journal of Instrumentation*, 7:P08025, 2012. doi:doi:10.1088/1748-0221/7/08/P08025.
- [MDF⁺13] S. Mertens, G. Drexlin, F.M. Fränkle, et al. Background due to stored electrons following nuclear decays in the KATRIN spectrometers and its impact on the neutrino mass sensitivity. *Astroparticle Physics*, 41:52–62, 2013. doi:10.1016/j.astropartphys.2012.10.005.
- [MIa] Inc. MKS Instruments. *HPS Products Series 423 I-MAG Cold Cathode Ionization Vacuum Sensor*.
- [MIb] Inc. MKS Instruments. *MKS Baratron Type 627D Absolute Pressure Transducer*.
- [MI18] Inc. MKS Instruments. Baratron[®] High Accuracy Systems Product Selection Guide. Brochure, 2018. <https://www.mksinst.com/docs/UR/HighAccuracyBaratronSelectionGuide-DS.pdf>.

- [MNS62] Ziro Maki, Masami Nakagawa, and Shoichi Sakata. Remarks on the unified model of elementary particles. *Prog. Theor. Phys.*, 28:870–880, 1962. doi:10.1143/PTP.28.870. [,34(1962)].
- [MS59] D. B. Mann and R. B. Stewart. Thermodynamic properties of helium at low temperatures and high pressures. *J. Heat Transfer*, 81:323–326, Nov 1959. doi:10.1115/1.4008218.
- [MS86] S. P. Mikheyev and A. Yu. Smirnov. Resonant amplification of ν oscillations in matter and solar-neutrino spectroscopy. *Il Nuovo Cimento C*, 9(1):17–26, Jan 1986. doi:10.1007/BF02508049.
- [MSac80] Rabindra N. Mohapatra and Goran Senjanović. Neutrino mass and spontaneous parity nonconservation. *Phys. Rev. Lett.*, 44:912–915, Apr 1980. doi:10.1103/PhysRevLett.44.912.
- [MWKW15] E. G. Myers, A. Wagner, H. Kracke, and B. A. Wesson. Atomic masses of tritium and helium-3. *Physical Review Letters*, 114:013003, 2015. doi:10.1103/PhysRevLett.114.013003.
- [NAB⁺18] A. Nucciotti, B. Alpert, M. Balata, et al. Status of the holmes experiment to directly measure the neutrino mass. *Journal of Low Temperature Physics*, 193(5):1137–1145, Dec 2018. doi:10.1007/s10909-018-2025-x.
- [NRS05] Sergej A. Nepijko, Irene Rabin, and Wilfried Schulze. Morphology of frozen rare-gas layers. *ChemPhysChem*, 6(2):235–238, 2005. doi:10.1002/cphc.200400420.
- [Nuc12] A. Nucciotti. Neutrino mass calorimetric searches in the mare experiment. *Nuclear Physics B - Proceedings Supplements*, 229-232:155 – 159, 2012. doi:https://doi.org/10.1016/j.nuclphysbps.2012.09.025. Neutrino 2010.
- [OSL⁺12] A. Osipowicz, W. Seller, J. Letnev, et al. A mobile magnetic sensor unit for the KATRIN main spectrometer. *Journal of Instrumentation*, 7(06):T06002, 2012. doi:10.1088/1748-0221/7/06/T06002.
- [Ott94] E Otten. The mainz neutrino mass experiment. *Progress in Particle and Nuclear Physics*, 32:153–171, 12 1994. doi:10.1016/0146-6410(94)90016-7.
- [OW08] E. W. Otten and C. Weinheimer. Neutrino mass limit from tritium β decay. *Reports on Progress in Physics*, 71(8):086201, 2008. doi:10.1088/0034-4885/71/8/086201.
- [Par06] Stephen J. Parke. Determining the neutrino mass hierarchy. In *Third NO-VE International Workshop on Neutrino Oscillations in Venice : Fifty years after the neutrino experimental discovery : Venezia, February 7-10, 2006, Istituto Veneto di Scienze, Lettere ed Arti, Campo Santo Stefano*, pages 115–125, 2006. URL http://lss.fnal.gov/cgi-bin/find_paper.pl?conf-06-248.

- [Per08] D.H. Perkins. *Particle Astrophysics, Second Edition*. Oxford Master Series in Physics. OUP Oxford, 2008. URL <https://books.google.de/books?id=fBNzZF7kLz4C>.
- [PKW64] W. E. F. Pauli, R. Kronig, and V. F. Weisskopf. *Collected scientific papers*. Interscience, New York, NY, 1964. Offener Brief an die Gruppe der Radioaktiven bei der Gauvereinstagung zu Tübingen (datiert 4. Dez. 1930).
- [Pon57] B. Pontecorvo. Mesonium and anti-mesonium. *Sov. Phys. JETP*, 6:429, 1957. [Zh. Eksp. Teor. Fiz.33,549(1957)].
- [Pon58] B. Pontecorvo. Inverse beta processes and nonconservation of lepton charge. *Sov. Phys. JETP*, 7:172–173, 1958. [Zh. Eksp. Teor. Fiz.34,247(1957)].
- [Pon68] B. Pontecorvo. Neutrino Experiments and the Problem of Conservation of Leptonic Charge. *Sov. Phys. JETP*, 26:984–988, 1968. [Zh. Eksp. Teor. Fiz.53,1717(1967)].
- [Pra11] Mathias Prall. *Background Reduction of the KATRIN Spectrometers: Transmission Function of the Pre-Spectrometer and Systematic Test of the Main-Spectrometer Wire Electrode*. PhD thesis, Westfälische Wilhelms-Universität Münster, 2011. URL http://www.researchgate.net/publication/238418212_Transmission_Function_of_the_Pre-Spectrometer_and_Systematic_Tests_of_the_Main-Spectrometer_Wire_Electrode_%28PHD_thesis%29.
- [PRG⁺12] M. Prall, P. Renschler, F. Glück, et al. The KATRIN pre-spectrometer at reduced filter energy. *New Journal of Physics*, 14(7):073054, 2012. doi:10.1088/1367-2630/14/7/073054.
- [PS95] M. E. Peskin and D. V. Schroeder. *An Introduction to Quantum Field Theory*. Westview Press, 1995.
- [PSB15] F. Priester, M. Sturm, and B. Bornschein. Commissioning and detailed results of KATRIN inner loop tritium processing system at tritium laboratory karlsruhe. *Vacuum*, 116:42–47, 2015. doi:10.1016/j.vacuum.2015.02.030.
- [QV15] X. Qian and P. Vogel. Neutrino mass hierarchy. *Progress in Particle and Nuclear Physics*, 83:1 – 30, 2015. doi:<https://doi.org/10.1016/j.pnpnp.2015.05.002>.
- [RC53] F. Reines and C. L. Cowan. Detection of the free neutrino. *Phys. Rev.*, 92:830–831, Nov 1953. doi:10.1103/PhysRev.92.830.
- [Rei13] Jan Reich. *Magnetic Field Inhomogeneities and Their Influence on Transmission and Background at the KATRIN Main Spectrometer*. PhD thesis, Karlsruher Institut für Technologie (KIT), 2013. doi:10.5445/IR/1000033076.
- [RK88] R. G. H. Robertson and D. A. Knapp. Direct measurements of neutrino mass. *Annual Review of Nuclear and Particle Science*, 38(1):185–215, 1988. doi:10.1146/annurev.ns.38.120188.001153.

- [Röll15] Marco Röllig. *Tritium analytics by beta induced X-ray spectrometry*. PhD thesis, Karlsruher Institut für Technologie (KIT), 2015. doi:10.5445/IR/1000054050.
- [Röt16] Carsten Röttele. Simulationen zu den inbetriebnahmemessungen mit der kryogenen pumpstrecke cps des katrin experiments. Master thesis, Karlsruher Institut für Technologie (KIT), 2016.
- [SAB⁺04] M Sisti, C Arnaboldi, C Brofferio, et al. New limits from the milano neutrino mass experiment with thermal microcalorimeters. *Nuclear Instruments and Methods in Physics Research Section A: Accelerators, Spectrometers, Detectors and Associated Equipment*, 520:125–131, 03 2004. doi:10.1016/j.nima.2003.11.273.
- [SBD⁺13] M. Slezák, S. Bauer, O. Dragoun, et al. Electron line shape of the KATRIN monitor spectrometer. *Journal of Instrumentation*, 8(12):T12002, 2013. doi:10.1088/1748-0221/8/12/T12002.
- [Sch06] Peter Schneider. Extragalactic astronomy and cosmology. *Extragalactic Astronomy and Cosmology, by Peter Schneider*. Berlin: Springer, 2006., 01 2006. doi:10.1007/978-3-642-54083-7.
- [Sch14] Johannes S. Schwarz. *The Detector System of the KATRIN Experiment - Implementation and First Measurements with the Spectrometer*. PhD thesis, Karlsruher Institut für Technologie (KIT), 2014. doi:10.5445/IR/1000042772.
- [Sch17] Lutz Schimpf. Untersuchung thermischer und radioaktiver Einflüsse auf den Tritium-Rückhaltefaktor der kryogenen Pumpstrecke von KATRIN. Master thesis, Karlsruher Institut für Technologie (KIT), 2017.
- [SJF⁺13] M. Schlösser, T. M. James, S. Fischer, et al. Evaluation method for raman depolarization measurements including geometrical effects and polarization aberrations. *Journal of Raman Spectroscopy*, 44(3):453–462, 2013. doi:10.1002/jrs.4201.
- [Sle15] Martin Slezák. *Monitoring of the energy scale in the KATRIN neutrino experiment*. PhD thesis, Charles University in Prague, 2015. URL <https://is.cuni.cz/webapps/zzp/detail/110567/?lang=en>.
- [SM19] Hendrik Seitz-Moskaliuk. *Characterisation of the KATRIN tritium source and evaluation of systematic effects*. PhD thesis, Karlsruher Institut für Technologie (KIT), 2019. doi:10.5445/IR/1000090748.
- [SRS⁺13] M. Schlösser, S. Rupp, H. Seitz, et al. Accurate calibration of the laser raman system for the Karlsruhe Tritium Neutrino experiment. *Journal of Molecular Structure*, 1044(0):61–66, 2013. doi:10.1016/j.molstruc.2012.11.022.
- [SSR⁺13] M. Schlösser, H. Seitz, S. Rupp, et al. In-line calibration of raman systems for analysis of gas mixtures of hydrogen isotopologues with sub-percent accuracy. *Analytical Chemistry*, 85(5):2739–2745, 2013. doi:10.1021/ac3032433.

- [Stu10] Michael Sturm. *Aufbau und Test des Inner-Loop-Systems der Tritiumquelle von KATRIN*. PhD thesis, Karlsruher Institut für Technologie (KIT), 2010. doi:10.5445/IR/1000019355.
- [SV80] J. Schechter and J. W. F. Valle. Neutrino masses in $su(2) \otimes u(1)$ theories. *Phys. Rev. D*, 22:2227–2235, Nov 1980. doi:10.1103/PhysRevD.22.2227.
- [TAA⁺16] The Double Chooz collaboration, Y. Abe, S. Appel, et al. Measurement of θ_{13} in double chooz using neutron captures on hydrogen with novel background rejection techniques. *Journal of High Energy Physics*, 2016(1):163, Jan 2016. doi:10.1007/JHEP01(2016)163.
- [THH⁺18] M. Tanabashi, K. Hagiwara, K. Hikasa, et al. Review of particle physics. *Phys. Rev. D*, 98:030001, Aug 2018. doi:10.1103/PhysRevD.98.030001.
- [Tro19] Nikolaus Rainer-Maria Trost. *Modeling and measurement of Rydberg-State mediated Background at the KATRIN Main Spectrometer*. PhD thesis, Karlsruher Institut für Technologie (KIT), 2019. doi:10.5445/IR/1000090450.
- [UDRL⁺09] M. Ubieto-Díaz, D. Rodríguez, S. Lukic, et al. A broadband FT-ICR penning trap system for KATRIN. *International Journal of Mass Spectrometry*, 288(1–3):1–5, 2009. doi:10.1016/j.ijms.2009.07.003.
- [Vaca] Leybold Vacuum. *MAG digital series*.
- [Vacb] Pfeiffer Vacuum. *HIPACE 300 Turbopumpe*.
- [Vacc] Pfeiffer Vacuum. *Prisma Quadrupole mass spectrometer QMS 200*.
- [v116] Nenion vacuum leakvalves. Manual UHV leakvalve ND 3. Brochure, 2016.
- [WAH⁺57] C. S. Wu, E. Ambler, R. W. Hayward, D. D. Hoppes, and R. P. Hudson. Experimental Test of Parity Conservation in Beta Decay. *Physical Review*, 105:1413–1414, 1957. doi:10.1103/PhysRev.105.1413.
- [WBOF94] A. Wucher, W. Berthold, H. Oechsner, and K. Franzreb. Detection of sputtered metastable atoms by autoionization. *Phys. Rev. A*, 49:2188–2190, Mar 1994. doi:10.1103/PhysRevA.49.2188.
- [WDF⁺13] N. Wandkowsky, G. Drexlin, F.M. Fränkle, et al. Validation of a model for radon-induced background processes in electrostatic spectrometers. *Journal of Physics G: Nuclear and Particle Physics*, 40(8):085102, 2013. doi:10.1088/0954-3899/40/8/085102.
- [Wei35] C. F. v. Weizsäcker. Zur theorie der kernmassen. *Zeitschrift für Physik*, 96(7):431–458, Jul 1935. doi:10.1007/BF01337700.
- [Wol78] L. Wolfenstein. Neutrino oscillations in matter. *Phys. Rev. D*, 17:2369–2374, May 1978. doi:10.1103/PhysRevD.17.2369.

- [WS12] L Winslow and R Simpson. Characterizing quantum-dot-doped liquid scintillator for applications to neutrino detectors. *Journal of Instrumentation*, 7(07):P07010–P07010, jul 2012. doi:10.1088/1748-0221/7/07/p07010.
- [WZB54] R. D. Worley, M. W. Zemansky, and H. A. Boorse. The vapor-pressure curve of helium between 4.2°k and 4.8°k. *Phys. Rev.*, 93:45–46, Jan 1954. doi:10.1103/PhysRev.93.45.
- [Yan80] Tsutomu Yanagida. Horizontal Symmetry and Masses of Neutrinos. *Progress of Theoretical Physics*, 64(3):1103–1105, 09 1980, <http://oup.prod.sis.lan/ptp/article-pdf/64/3/1103/5394376/64-3-1103.pdf>. doi:10.1143/PTP.64.1103.
- [YPDBdMdB17] Christophe Yèche, Nathalie Palanque-Delabrouille, Julien Baur, and Héliion du Mas des Bourboux. Constraints on neutrino masses from lyman-alpha forest power spectrum with BOSS and XQ-100. *Journal of Cosmology and Astroparticle Physics*, 2017(06):047–047, jun 2017. doi:10.1088/1475-7516/2017/06/047.
- [ZBB⁺13] M. Zbořil, S. Bauer, M. Beck, et al. Ultra-stable implanted $^{83}\text{rb}/^{83\text{m}}\text{kr}$ electron sources for the energy scale monitoring in the KATRIN experiment. *Journal of Instrumentation*, 8(03):P03009, 2013. doi:10.1088/1748-0221/8/03/P03009.
- [Zbo11] Miroslav Zbořil. *Solid electron sources for the energy scale monitoring in the KATRIN experiment*. PhD thesis, Westfälische Wilhelms-Universität Münster, 2011. URL <http://nbn-resolving.de/urn:nbn:de:hbz:6-91469497689>.
- [Zel17] Genrich Zeller. Development of a calibration procedure and calculation of the uncertainty budget for the KATRIN laser Raman system. Master thesis, Karlsruher Institut für Technologie (KIT), 2017. URL <https://www.katrin.kit.edu/publikationen/mth-Zeller.pdf>.
- [Zem65] J. Zemann. Crystal structures, 2nd edition. vol. 1 by r. w. g. wyckoff. *Acta Crystallographica*, 18(1):139–139, 1965, <https://onlinelibrary.wiley.com/doi/pdf/10.1107/S0365110X65000361>. doi:10.1107/S0365110X65000361.
- [Zub12] Kai Zuber. *Neutrino physics*. Series in high energy physics, cosmology, and gravitation. CRC Press / Taylor and Francis, Boca Raton, Fla., 2. ed. edition, 2012. URL <http://www.gbv.de/dms/goettingen/573268584.pdf>; <https://www.crcpress.com/Neutrino-Physics-Second-Edition/Zuber/9781420064711;..>

Danksagung

Zum Abschluss möchte ich mich bei allen bedanken, die mich während meiner Doktorarbeit unterstützt haben. Dabei geht mein besonderer Dank an:

- Prof. Dr. Guido Drexlin, der mir die Möglichkeit gegeben hat, meine Doktorarbeit im Rahmen des KATRIN Experimentes durchzuführen und seine sehr guten Vorlesungen, die meine Begeisterung an der Neutrinophysik geweckt haben.
- Prof. Dr. Ulrich Husemann für die Übernahme der Zweitkorrektur und die sehr hilfreichen Korrekturen.
- Dr. Markus Steidl für die wissenschaftliche Unterstützung vor allem bei den Aufbau und Durchführung der CPS Inbetriebnahme Messungen. Außerdem für das Korrekturlesen meiner Arbeit.
- Dr. Kathrin Valerius für die vielen Läufe und dem Motivieren zum Frankfurt Marathon. Zusätzlich für die Hilfe bei allen möglichen Dingen und vielen tollen Unterhaltungen.
- Dr. Florian Heizmann für die wöchentliche Fitnessgänge mit anschließendem Döner. Gleichzeitig für die Hilfe bei allen programmiertechnischen Problemen.
- Fabian Friedel, Johannes Heizmann und Lutz Schimpf für die sehr schöne Zeit miteinander im Büro. Dafür das es fast jeden Morgen wieder eine Freude war zur Arbeit zu gehen und die schönen und oftmals lustigen Unterhaltungen.
- Dr. Alexander Jansen und Michael Schrank für die Unterstützung bei allen Kryoproblemen und die gemeinsame Arbeit bei der Rufbereitschaft.
- Dem Loops Team für die sehr gute Zusammenarbeit und bei der Hilfe beim erfolgreichen Aufbau des CPS Loop-Systems.
- Dr. Joachim Wolf für das Korrekturlesen der meiner Arbeit und jeglicher Hilfe bei verschiedenen Vakuumfragen.
- Anton Huber, Dr. Moritz Hackenjos und Dr. Hendrik Seitz-Moskaliuk für das Miterleben vieler toller Momente, vor allem auch auf den zahlreichen Dienstreisen.

- Stephanie Hickford für die Hilfe beim Korrekturlesen.
- Lläuft bei KATRIN für die vielen Runden um den Campus Nord, die für frischen Sauerstoff sorgten. Außerdem für die zahlreichen gemeinsamen bestrittenen Wettkämpfe.
- Allen KATRIN Young Scientists für die gemeinsame mittwöchliche Pizza und die vielen ereignisreichen Stammtisch-Abende.
- Klaus Mehret für die schnelle und gute Erledigung aller handwerklichen Arbeiten. Und natürlich für das tägliche Abholen zum Essen mit anschließendem Kaffee.
- Katharina Fischer und Marion Behecti für die Hilfe in allen organisatorischen Dingen.
- Allen Freunden, die mich im Verlauf meiner Promotion begleitet haben.

Zuletzt möchte ich mich bei meiner Familie bedanken, die auch in den nicht immer einfachen Zeiten zu mir gestanden haben. Ohne euch wäre mein Studium mit anschließender Promotion nicht möglich gewesen.